

ANTI-ICING FUNCTIONAL BIPHILIC SURFACES AND FUNCTIONALIZED  
MULTISCALE METAL ORGANIC FRAMEWORK-BASED COATINGS

by

SHAGHAYEGH SAEIDIHARZAND

Submitted to the Graduate School of Engineering and Natural Sciences

in partial fulfillment of the requirements for the degree of

Doctor of Philosophy

Sabancı University

July 2023

© Shaghayegh Saeidiharzand

All rights reserved

## ABSTRACT

### ANTI-ICING FUNCTIONAL BIPHILIC SURFACES AND FUNCTIONALIZED MULTISCALE METAL ORGANIC FRAMEWORK-BASED COATINGS

SHAGHAYEGH SAEIDIHARZAND

Materials Science and Nano Engineering, Ph.D. Dissertation, July 2023

Thesis Supervisor: Prof. Dr. Ali Koşar

Keywords: Anti-icing surfaces, Superhydrophobic surfaces, Droplet impact, ZIF-8, Metal-organic framework, Micro-nano-subnano coating, Heterogenous wettability, dynamic de-icing, passive cleaning

Ice formation is a major challenge for engineering systems. In this dissertation, it is aimed to provide understanding about fundamentals of ice formation, ice accumulation and de-icing, to identify the governing mechanisms and to develop surfaces and coatings for anti-icing applications.

In this thesis, a functionalized metal-organic framework (ZIF-8) based micro-nano-subnano scale coating (SHMC) with  $CA > 172^\circ$ , rolling angle  $< 5^\circ$ , and  $CAH < 3^\circ$  was developed. The coating was applied to metallic substrates by the practical spray coating method. Superimposed nanoparticles and porous structure of ZIF-8 created a surface morphology containing a significant number of airpockets.

This thesis proves the superiority of SHMC over current approaches. Static and dynamic anti-icing behavior of SHMC was vigorously investigated. A fractal theory-based model of water contact angle was adapted to reveal its non-wetting mechanism. SHMC extended the icing time by at least 300% and maintained its superhydrophobicity for more than 30 icing/deicing cycles. The generated capillary pressure ranges within the multiscale coating were studied. The three-phase contact line characteristics were assessed. A significant reduction in heat transfer during the droplet contact time was obtained with SHMC.

Furthermore, this thesis provides valuable information about de-icing behavior of biphilic surfaces. The results indicated that the biphilic surface consisting of superhydrophobic islands with the diameter of  $D = 500 \mu\text{m}$  on a hydrophilic substrate having the superhydrophobicity ratio of 19.62% was capable of complete passive cleaning due to the Laplace pressure gradient generated by this specific surface design. Furthermore, as the superhydrophobicity ratio increased, more delay in ice formation and accumulation occurred. The results show that the choice of the surface design is a compromise between its icing and de-icing behavior.

## ÖZET

# BUZLANMA ÖNLEYİCİ FONKSİYONEL BİFİLİK YÜZEYLER VE FONKSİYONEL ÇOK ÖLÇEKLİ METAL ORGANİK ÇERÇEVELİ KAPLAMALAR

SHAGHAYEGH SAEIDIHARZAND

Malzeme Bilimi ve Nano Mühendislik, Doktora Tezi, Haziran 2019

Tez Danışmanı; Professor Dr. Ali Koşar

Anahtar kelimeler: Buzlanma önleyici yüzeyler, süperhidrofobik yüzeyler, ZIF-8, mikro-nano-nanoatlı kaplama, heterojen ıslanabilirliği, dinamik buz çözme, pasif temizleme, damla etkisi.

Buz oluşumu, mühendislik sistemleri için büyük bir sorundur. Bu tezde buz oluşumunun temelleri, buz birikimi ve buzlanmama temelleri hakkında bilgi verilmesi, ilgili mekanizmaların belirlenmesi ve buzlanma önleyici uygulamalar için yüzey ve kaplamalar geliştirilmesi amaçlanmaktadır.

Bu tez çalışmasında temas açısı ( $CA > 172^\circ$ ), yuvarlanma açısı  $< 5^\circ$  ve temas açısı histerisi ( $CA_H < 3^\circ$ ) olan işlevselleştirilmiş bir metal-organik kafesli (ZIF-8) tabanlı mikro-nano-nanoaltı ölçekli kaplama (SHMC) geliştirilmiştir. Araştırmada geliştirilen kaplama pratik sprey kaplama yöntemiyle metalik alt tabakalara uygulanmıştır. Kaplamada kullanılan ZIF-8 nanoparçacıkları, üst üste birleştirilmiş ve gözenekli yapısı sayesinde önemli sayıda hava cebi içeren bir yüzey morfolojisi yaratmıştır.

Bu tez SHMC'nin mevcut yöntemlere karşı üstünlüğünü kanıtlayan bir araştırmadır. SHMC'nin statik ve dinamik buzlanma önleme davranışı derinlemesine araştırılmıştır. Islanmama mekanizmasını ortaya çıkarmak için fraktal teoriye dayalı bir su temas açısı modeli geliştirilmiştir. SHMC yöntemi buzlanma süresini en az %300 uzatarak süperhidrofobikliğini 30'dan fazla buzlanma/buz çözme döngüsü boyunca koruyabilmiştir. Gerçekleştirilen çok ölçekli kaplama içerisinde üretilen kılcal basınç aralıkları incelenmiş ve üç fazlı temas hattı özellikleri değerlendirilerek SHMC ile damlacık temas süresi boyunca ısı transferinde önemli bir azalma elde edilmiştir.

Bunun yanında bu tez çalışması bifilik yüzeylerin buz çözme davranışı hakkında önemli bilgiler sunmaktadır. Tez çalışmasının sonuçları süperhidrofobiklik oranı %19.62 olan hidrofilik bir substrat üzerinde  $D=500 \mu\text{m}$  çapındaki süperhidrofobik adalardan oluşan bifilik yüzeyin, bu özel yüzey tasarımı tarafından üretilen Laplace basınç gradyanı nedeniyle tam pasif temizleme yeteneğine sahip olduğunu göstermiştir. Üstelik süperhidrofobiklik oranı arttıkça buz oluşumunda ve birikmesinde daha fazla gecikme meydana gelmiştir. Bu tez çalışmasının sonuçları yüzey tasarımı seçiminin, buzlanma ve buz çözme davranışı arasında bir denge olduğunu göstermektedir.

## Acknowledgements

I would like to express my gratitude and deepest appreciation to my thesis advisor Prof. Dr. Ali Koşar for his invaluable guidance, support, and patience during this research journey. It has been an honor and a privilege to have him as both my doctoral advisor and mentor. His unwavering mentorship was beyond the role of advisor and he created a supportive, friendly and motivational work environment for all of us. He always encouraged me and he provided multiple opportunities for me to improve my skills and experiences as an independent researcher.

I would like to express my sincere appreciation to Dr. Alp Yürüm for his support, help, insightful comments and accessibility during my Ph.D. studies as my thesis progress committee member. His extensive expertise has been substantial in broadening my understanding of materials characterization and helped me to explore new avenues and approach my research from a different aspect.

I would like to extend my gratitude to my honorable thesis progress committee member Dr. Hüseyin Üvet and dissertation jury members Dr. Emre Erdem and Dr. Yegan Erdem for their time, valuable feedbacks and comments.

I am would like to thank my dear friends Gülayşe Şahin Dündar, Dilara Çelik, Mariam Omer, Amin Ahmadi, Farzin Asghari who supported me during this journey and made these years memorable. Additionally, I am very grateful for the friendship and support of all of the members of the Micronano Scale Heat Transfer & Microfluidics Research Group. It was such a blast to work as a member of this hardworking and active group.

Furthermore, I would like to thank Sabanci University Faculty of Engineering and Natural Science (FENS) for graduate student support. The related studies were supported by TÜBİTAK (The Scientific and Technological Research Council of Turkey) Support Program for Scientific and Technological Research Project Grant No. 120M659 and UK Research and Innovation ODA Impact and Development Grant.

This thesis has been dedicated to my beloved parents Roghayeh and Hasan Saeidiharzand who taught me that everything is possible with hard work and dedication

and my brother, Sahand Saeidiharzand, who encouraged me every day to peruse my dreams and was present in every moment of this journey.

## TABLE OF CONTENT

Contents	
Acknowledgements.....	viii
Table of content .....	x
List of Figures .....	xiii
LIST OF SYMBOLS AND ABBREVIATIONS .....	xvi
Chapter I: Introduction.....	1
1.1 Motivations .....	2
1.2 Objectives .....	2
1.2.1 Design and development of superhydrophobic multiscale metal organic framework-based coating as a passive method .....	3
1.2.2 A fundamental study on ice formation and accumulation through different methods and evaluation of the anti-icing performance and durability of the developed coating .....	3
1.2.3 Active de-icing.....	4
1.2.4 Propose a surface design suitable for both passive and active de-icing methods .....	4
1.3 Thesis outline .....	4
Chapter II: Literature Survey .....	6
2.1. Freezing.....	6
2.2. De-icing techniques.....	11
2.1.1 Active ice protection techniques.....	12
2.1.2 Passive ice protection techniques .....	17
Chapter III: Development of a multiscale superhydrophobic zeolitic imidazole framework- based coating.....	26
3.1. Introduction .....	26

3.2. Experimental methods and procedure.....	27
3.2.1. Materials.....	27
3.2.2. Synthesis of ZIF-8 nanoparticles.....	27
3.2.3. Preparation of superhydrophobic ZIF-8 based coating .....	28
3.2.4 Materials characterization .....	28
3.3 Results and discussion.....	29
3.3.1. ZIF-8 nanoparticles .....	29
3.3.2. Superhydrophobic multiscale ZIF-8 based coating .....	38
3.4 Conclusions .....	40
Chapter IV: Static and dynamic icing behavior on a multiscale superhydrophobic zeolitic imidazole framework-based coating.....	42
4.1. Introduction.....	42
4.2. Experimental procedure .....	43
4.3. Results and discussions.....	45
4.3.1. Non-wetting mechanisms .....	45
4.3.2 Thermodynamic of the phase change and static icing.....	49
4.3.3 Dynamic water/ice repellency and contact line behavior .....	57
4.4. Conclusion.....	61
Chapter V: Biphilic surfaces for icing/de-icing applications and passive cleaning of surfaces .....	63
5.1. Introduction.....	63
5.2. Experimental procedure .....	64
5.2.1. Surface fabrication.....	64
5.2.2. Icing/de-icing experiments .....	68
5.3. Results and discussion.....	69
5.3.1. Effect of wettability on icing/de-icing.....	70

5.3.2. Condensation icing.....	75
5.3.2. De-frosting.....	81
5.4. Conclusion.....	96
Chapter VI: Conclusions and future works.....	97
6.1. Conclusions.....	97
6.2. Future prospective.....	98
6.3. Contribution to the scientific community.....	99
References.....	101

## LIST OF FIGURES

Figure 1. Phase diagram of water (Q. Li & Guo, 2018).....	7
Figure 2. Schematic of a heterogenous nucleation.....	9
Figure 3. Energy difference for homogenous and heterogenous nucleation (Fan & Men, 2022).....	10
Figure 4. Condensation frosting involving four consecutive stages of a) droplet condensation, b) droplet coalescence, c) ice nucleation and bridging, and d) dendrites growth (C. Huang et al., 2022). .....	11
Figure 5. Major passive anti-icing mechanisms with examples.....	17
Figure 6. Superhydrophobic coating based on porous ZIF-8 nanoparticles.....	22
Figure 7. XRD pattern of the as-synthesized ZIF-8 nanoparticles under different conditions. ....	29
Figure 8. SEM images of sample Z-1. ....	30
Figure 9. FTIR spectrum for ZIF-8 nanoparticles.....	31
Figure 10. SEM images of the as-synthesized Z-2 in different magnifications. ....	32
Figure 11. SEM images of the as-synthesized Z-2 in different magnifications. ....	33
Figure 12. a) Isotherm linear plot and b) Horvath-Kawazoe differential pore volume plot of sample Z-2. ....	34
Figure 13. SEM images of the as-synthesized Z-3 in different magnifications. ....	36
Figure 14. TEM images of the as-synthesized Z-3 in different magnifications. ....	36
Figure 15. a) Isotherm linear plot and b) Horvath-Kawazoe differential pore volume plot of sample Z-3. ....	37
Figure 16. (a-d) SEM images of ZIF-8 based coating in different magnifications. ....	38
Figure 17. Energy Dispersive X Ray (EDX) analysis results of ZIF-8 based coating. ....	39
Figure 18. Contact angle and contact angle hysteresis measurements of ZIF-8 based coating. ....	40
Figure 19. Schematic of the experimental setup for static and dynamic icing. The green region shows the equipment required for dynamic icing tests and orange region shows the surface cooling apparatus .....	44
Figure 20. a) Comparison between the predicted static WCAs by the classical Cassie-Baxter and fractal methods and experimental results on different samples, b) AFM results of the surface area of $1 \times 1 \mu\text{m}^2$ (top) and $20 \times 20 \mu\text{m}^2$ (bottom), c) surface profile of the SHMC on a copper substrate. ....	47
Figure 21. a) SEM image of the SHMC (inset: a reduced size generated from the fractal analysis), b) double-logarithmic plot of the $N(x)$ and $x$ , which displays the fractal dimension of 1.83 as the slope of the plot, c) the volume below $S_{\text{max}}$ in order to calculate $\phi_s$ .....	49

Figure 22. Plot of shape function for different hydrophilic and hydrophobic fractal surfaces (redrawn from [94]).	50
Figure 23. a) Surface freezing time on SHMC and bare samples on different surfaces and under ambient conditions, b) Icing activity on SHMC and plain area (the coating at the edges of the sample was cleaned to show the anti-icing effectiveness of the coated area)	51
Figure 24. Schematic and microscopic images of coalescence induced droplet jumping on SHMC.	52
Figure 25. a) icing and icing mode on the bare aluminum surface, b) icing and icing mode on the coated aluminum surface	53
Figure 26. Ice layer growth on a coated and coated sample	53
Figure 27. Schematic and SEM image of the passages formed by MOF nanoparticle superposition and the mechanisms responsible for coating stability against droplets	55
Figure 28. Net forces acting on droplets at different pore/passage and droplet sizes (Here, the green region indicates the area corresponding to the calculated maximum passage sizes on SHMC surfaces)	56
Figure 29. Water contact angle variation with icing/deicing cycles at different surface temperatures.	56
Figure 30. a) High-speed images taken from the early stages of droplet impact on bare (uncoated) and SHMC aluminum surfaces; b) Droplet edge upon spreading on the bare (uncoated) and SHMC aluminum surfaces, c) Fingering of the droplets is evident on coated surface.	58
Figure 31. High-speed images taken from the early later stages of droplet spreading on bare (uncoated) and SHMC aluminum surfaces.	59
Figure 32. High-speed images taken from the early later stages of droplet spreading on bare (uncoated) and SHMC aluminum surfaces.	60
Figure 33. IR thermography images of an impact on bare and coated aluminum surfaces.	61
Figure 34. Configuration of biphilic samples consisting of superhydrophobic areas (blue spots), a hydrophilic substrate, as P, D, and S represent the pitch size, diameter, and edge-to-edge spacing with $P = D + S$ .	66
Figure 35. Schematic of the microfabrication process of the sample.	67
Figure 36. SEM images of a biphilic sample consisting of superhydrophobic islands with $D=700 \mu\text{m}$ .	68
Figure 37. Photographs of the customized experimental icing setup.	69

Figure 38. The sequence of images taken from biphilic surface during condensation, icing at the temperature of $-15^{\circ}\text{C}$ and relative humidity (RH) of 75% and thermal de-icing at $6^{\circ}\text{C}$ on sample D5.....	73
Figure 39. a) Schematic of drop condensation and icing on hydrophilic (HPhi) and superhydrophobic (SHpho) surfaces, b) Sequence of images showing icing at the temperature of $-15^{\circ}\text{C}$ and relative humidity (RH) of 75% on sample D5. ....	74
Figure 40. Superhydrophobicity ratio versus ice accumulation time on samples at RH=55% and $T_s=-8^{\circ}\text{C}$ .....	76
Figure 41. Intermediate icing stage on a) fully hydrophilic reference sample, b) fully superhydrophobic reference sample, c) sample D1000, d) sample D150, e) sample D700 and f) sample D500 at $t=3.5$ mins after the substrates reach $T_s= -8^{\circ}\text{C}$ . ....	77
Figure 42. Intermediate icing stage on a) sample D1, b) sample D10, c) sample D5, and d) sample D7 at $t=3.5$ mins after the substrates reach $T_s= -8^{\circ}\text{C}$ .....	79
Figure 43. Ice propagation through bridging on a a) hydrophilic surface and b) superhydrophobic surface. ....	81
Figure 44. Normal-view time-lapse images of dynamic de-icing at $0^{\circ}\text{C}$ on sample D5.....	83
Figure 45. Normal-view time-lapse images of dynamic de-icing at $0^{\circ}\text{C}$ on sample D7. ....	86
Figure 46. Normal-view time-lapse images of dynamic de-icing at $0^{\circ}\text{C}$ on sample D10. ....	89
Figure 47. Normal-view time-lapse images of dynamic de-icing of a thin layer of ice at $0^{\circ}\text{C}$ on sample D10. ....	91
Figure 48. Normal-view time-lapse images of dynamic de-icing at $0^{\circ}\text{C}$ on sample D1. ....	92
Figure 49 Normal-view time-lapse images of dynamic de-icing at $0^{\circ}\text{C}$ on a) totally superhydrophobic and b) totally hydrophilic reference samples.....	93
Figure 50. Cleaning time at $0^{\circ}\text{C}$ - superhydrophobicity ratio.....	94

## LIST OF SYMBOLS AND ABBREVIATIONS

A: Surface area ( $\text{m}^2$ )

a: Characteristics length (m), acceleration ( $\text{m/s}^2$ )

Ca: Capillary number (-)

Cp: Specific heat (J/K)

D: Diameter (m)

F: Force (N)

g: Gravitational acceleration ( $\text{m/s}^2$ )

h: Heat transfer coefficient ( $\text{W/m}^2\cdot\text{K}$ )

k: Thermal conductivity ( $\text{W/m}\cdot\text{K}$ )

Ka: Langmuir adsorption constant (L/mg)

L: Distance (m)

M: Molar concentration

P: Pressure (bar)

p: Pitch size (m)

q: Heat flux ( $\text{W/cm}^2$ )

S: Average roughness (m)

D: Edge to edge spacing between islands (m)

T: Temperature (K)

U: Velocity (m/s)

V: Voltage (V)

X: Horizontal location (m)

X: Experimental parameter (variable unit)

Y: Vertical location (m)

BET: Brunauer Emmett Teller

FTIR: Fourier Transformed Infrared Spectroscopy

MOFs: Metal-organic frameworks

SEM: Scanning Electron Microscopy

TEM: Transmission Electron Microscopy

XRD: X-ray Diffraction

$\Delta G$ : Free energy change

$\Delta H$ : Ethalphy change (kJ/ mol)

$\Delta S$ : Entropy change (kJ/mol)

$\pi$ : Pi number (3.14159)

$\theta$ : Contact angle (degree), inclination angle (degree), diffraction angle (degree)

$\rho$ : Density (kg/m<sup>3</sup>)

$\sigma$ : Surface tension force (N/m)

$\gamma$ : Interfacial energy

## Chapter I: Introduction

Global climate change is a crucial concern that needs to be immediately dealt with. It is clear that the frequent occurrences of drought, flood, heat waves, and many other drastic events are the results of human-caused climate change. Climate change not only leads to the deterioration in natural resources but also puts most species in danger of extinction. Carbon emission is one of the major causes of global warming. High rates of fossil fuel consumption, nonefficient energy systems, and more importantly low investment in renewable and sustainable energy lead to excessive carbon emissions (Aboubakri et al., 2021).

Ice formation and accumulation have a fair share in carbon footprint increase. Ice accretion in energy-conversion systems cause improper energy transmission and efficiency setbacks. For instance, frosting on heat-exchangers reduce the heat transfer performance which leads to energy overconsumption, misuse of resources and environmental pollution (J. Yu, Zhang, & You, 2012). Green energy systems also suffer from this natural phenomenon. Ice formation on wind turbines and solar panels not only prevent the systems in reaching their highest efficiency but also leads to material degradation and the consequent need for maintenance or materials reproduction.

## 1.1 Motivations

Icing is a natural phenomenon that might occur in many engineering and industrial systems including solar panels, marine structures, power grids, heat exchangers, aircrafts and wind turbines. Ice formation and accumulation in infrastructure not only compromise the mechanical integrity of systems but also cause energy losses and performance setbacks. Ice formation-caused shortcomings not only have detrimental effects on environment and natural resources but also have been reported as a multi-billion-dollar problem (Gurumukhi et al., 2020). Therefore, de-icing methods have attracted much attention during past years to tackle with lead energy problems.

Ice accretion and frost formation on engineering surfaces is a multifaceted event and occurs in different ways. Proposing an effective solution requires a thorough understanding about this phenomenon, conditions and affects on the energy systems. The design and development of techniques as well as stablishing a balance in applicability, cost, environmental impact and efficiency are of a great importance.

Although different techniques have been proposed to prevent ice formation and accumulation both actively and passively they are mostly costly, environmentally unfriendly and low efficient (Benam et al., 2023). Therefore, this thesis aims to address these issues not only by providing a vigorous study on icing behavior from different perspectives but also by proposing effective new generation of functional anti-icing coatings/surfaces.

## 1.2 Objectives

The overall objective of this Ph.D. study is to design and test anti-icing coatings/surfaces with enhanced performance for prevention of ice frosting and for suppressing the common

icing induced problems. Furthermore, we present a detailed study on ice formation and accumulation as well as investigation of the interfacial phenomena and events throughout the course of this phase change.

The scope of this thesis covers the synthesis of a type of metal-organic framework suitable for the proposed application, optimization and characterization of the nanoparticles with different materials characterization methods in order to achieve the desirable properties, development of a superhydrophobic metal organic framework-based coating, characterization of the coating in terms of surface structure and surface chemistry, investigation and evaluation of the anti-icing performance of the coating under different conditions according to the industry applications.

The objectives of this study are listed as follows:

#### 1.2.1 Design and development of superhydrophobic multiscale metal organic framework-based coating as a passive method

The first objective of this thesis is to propose a novel superhydrophobic coating which can address the shortcoming of the current superhydrophobic coatings and surfaces in literature. For this, hierarchically porous hydrophilic metal-organic frameworks (MOF) were synthesized, characterized and optimized. A superhydrophobic multiscale MOF based coating was developed and evaluated in terms of surface structure, surface chemistry and wettability. It is aimed to propose and fabricate a uniform superhydrophobic coating for anti-icing applications.

#### 1.2.2 A fundamental study on ice formation and accumulation through different methods and evaluation of the anti-icing performance and durability of the developed coating

The second objective of this thesis is to provide a fundamental study on frosting. For this, the possible ice inducing events under real life conditions were identified. Icing experiments were designed to simulate the real-life experience. In this content, the anti-icing performance and durability of the developed superhydrophobic multiscale coating were investigated.

### 1.2.3 Active de-icing

The third objective of this thesis is to investigate the interfacial phenomena through the course of active de-icing on surfaces with different wettability. Since active defrosting is an inevitable approach in the industry it is of a great important to develop an understanding about the governing mechanisms.

### 1.2.4 Propose a surface design suitable for both passive and active de-icing methods

The fourth objective of this thesis is to investigate icing/de-icing behavior of surfaces with mixed wettability. It is aimed to propose a hybrid surface design which is not only capable of exhibiting a passive anti-icing behavior but can also contribute a better de-frosting performance.

## 1.3 Thesis outline

- Chapter I presents the motivation, challenges and research needs, objectives, and outline of the thesis.
- Chapter II describes fundamentals of icing and frost formation, identifies the icing induced problems, and delivers a literature survey on current de-icing techniques

(passive and active methods), high efficiency anti-icing surfaces and coatings and the shortcomings.

- Chapter III explores the design and development of a superhydrophobic multiscale coating (SHMC) as a potential candidate for anti-icing application.
- Chapter IV display fundamental studies on both static and dynamic icing behavior by evaluating SHMC performance.
- Chapter V covers interfacial phenomena during de-frosting on surfaces with mixed wettability. This chapter proposes surface designs that can generate a dynamic slush/water flow which contributes to surface cleaning with either no need or minimal need for external energy.
- Chapter VI summarizes the conclusions of the study, discusses the possible future work and the novel aspects of this thesis.

## Chapter II: Literature Survey

In order to be able to prevent icing and to decrease the risk of negative impacts induced by icing in energy and industrial systems, a thorough understanding about ice formation and accumulation is required. This chapter is dedicated to a comprehensive literature survey.

### 2.1. Freezing

Freezing is a phase transition from liquid to solid. The equilibrium freezing temperature of a material is defined as the saturation temperature between its solid and liquid phase, at a constant pressure. For instance, the equilibrium freezing temperature of pure water at the atmospheric pressure is zero degrees Celsius (dew point). However, pure water can be supercooled to approximately  $-40^{\circ}\text{C}$  before ice nucleates homogenously (Lamb & Verlinde, 2011). According to the thermodynamics of the phase change, the ice phase is stable at zero degrees Celsius, while a supercooled sessile water droplet has a metastable state and can stay in the liquid phase if there is no significant change in the system. Therefore,

the ice nucleation temperature in pure water is always less than 0 °C under the ambient pressure. Icing (frosting) is a complicated multiphase phenomenon which consists of different mechanisms occurring simultaneously since ice nucleation and growth are closely associated with the different phase transitions (Eberle, Tiwari, Maitra, & Poulikakos, 2014). According to the phase diagram of water (shown in Figure 1), water goes through various phase transitions under different environmental conditions (temperature and pressure). Ice formation can occur in three different ways (i) vapor–solid (sedimentation or desublimation), (ii) vapor–liquid–solid (condensation frosting), and (iii) liquid–solid (freezing) (Libbrecht, 2017; Schutzius et al., 2015).

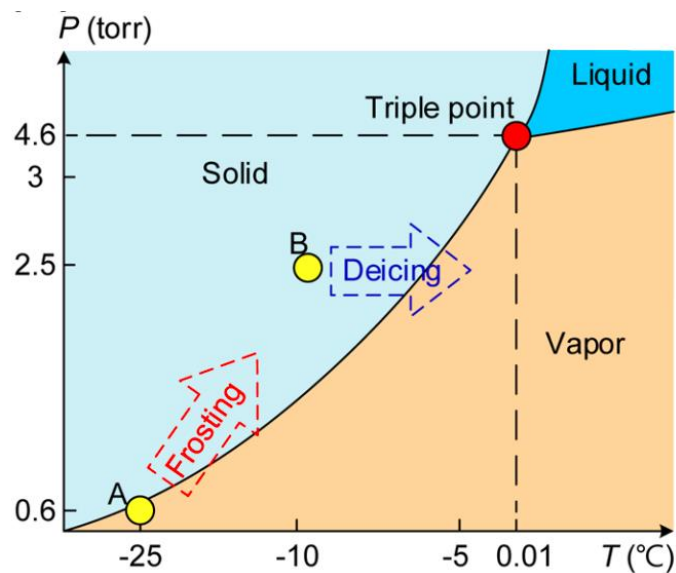


Figure 1. Phase diagram of water (Q. Li & Guo, 2018).

Desublimation frosting is defined as direct formation of solid from vapor on a wall or substrate. Condensation frosting involves a course of phase change phenomena where ice is formed as a result of three consecutive stages of 1) vapor condensation on a wall or substrate, 2) freezing of the condensate liquid, and 3) desublimation of vapor atop the frozen condensate.

A typical course of icing starts with water (vapor) supercooling and ice nucleation and then continues with ice front propagation within the liquid phase (freezing), or into the surrounding gas phase (desublimation). Ice nucleation can occur homogeneously (in the bulk of water) or heterogeneously (only at preferable locations). Fundamental concepts and mechanisms of both homogeneous and heterogeneous nucleation plays an important role in understanding icing from thermodynamics aspect.

Ice nucleation (crystallization) can be discussed with the use of the classical nucleation theory (CNT) based on thermodynamic perspectives (Y. Zhao, Guo, Lin, & Cheng, 2020). The homogeneous nucleation in form of a spherical ice crystal (phase  $\alpha$ ) with a radius  $r$  from vapor or liquid water (phase  $\beta$ ) occurs as the result of 1)  $\alpha$  to  $\beta$  phase change in a spherical volume  $V$ , and 2) generation of  $\alpha/\beta$  interface in an area  $A$ . The energy difference through the nucleation is the summation of volumetric bulk Gibbs free energy and interfacial energy:

$$\Delta G = V\Delta G_v + A_{\alpha\beta}\gamma_{\alpha\beta} \quad (1)$$

where  $\gamma_{\alpha\beta}$  is defined as the surface tension between phases  $\alpha$  and  $\beta$ . The volumetric Gibbs free energy difference ( $\Delta G_v$ ) for either water to ice or vapor to ice is directly related to supercooling cooling ( $T - T_m$ ).

The maximal value of  $\Delta G$  is achieved at a critical radius:

$$r^* \left| \frac{dG}{dr} = 0 = - \frac{2\gamma_{\alpha\beta}}{\Delta G_v} \right. \quad (2)$$

which is technically the smallest radius for the embryos to become stable. By substituting  $r^*$  into Equation 1, the maximum required energy for the formation of the smallest possible stable nuclei can be calculated as:

$$\Delta G^* = \Delta G(r^*) = \frac{16}{3} \pi \frac{\gamma_{\alpha\beta}^3}{\Delta G_v^2} \quad (3)$$

In heterogeneous nucleation on a solid substrate ( $\delta$ ), the ice embryo is considered as a spherical cap shape having a contact angle of  $\theta$  (shown in Figure 2). The energy difference for a heterogeneous nucleation consists of three terms of volumetric Gibbs free energy, interfacial energy as a result of generation of  $\alpha/\beta$  and  $\alpha/\delta$  interfaces and elimination of  $\beta/\delta$

interface. The critical radius for heterogenous nucleation is the same as the homogenous critical radius in homogenous and is independent of contact angle  $\theta$ :

$$\Delta G_{\text{het}} = V\Delta G_v + A_{\alpha\beta}\gamma_{\alpha\beta} + A_{\alpha\delta}\gamma_{\alpha\delta} - A_{\beta\delta}\gamma_{\beta\delta} \quad (4)$$

$\Delta G_{\text{het}}^*$  is be defined as:

$$\Delta G_{\text{het}}^* = \frac{1}{4} (2 - 3\cos\theta + \cos^3\theta)\Delta G_{\text{hom}}^* \quad (5)$$

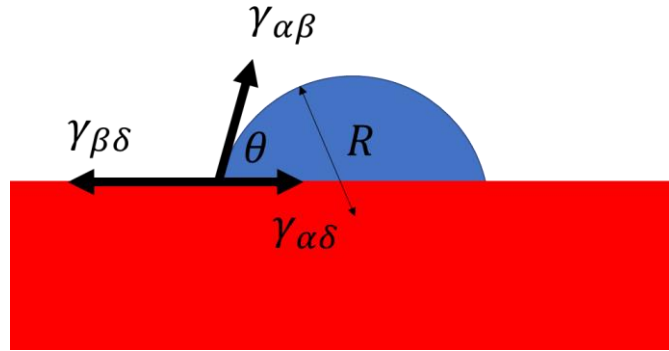


Figure 2. Schematic of a heterogenous nucleation.

Although the presence of active locations for nucleation does not affect the critical nucleation radius, heterogenous nucleation requires a lower activation energy compared to homogenous nucleation. Therefore, for heterogenous nucleation, a smaller supercooling is required. As the activation energy for nucleation is overcome, the stabilized embryos grow larger into ice crystals and lead to the further increase in the total energy.

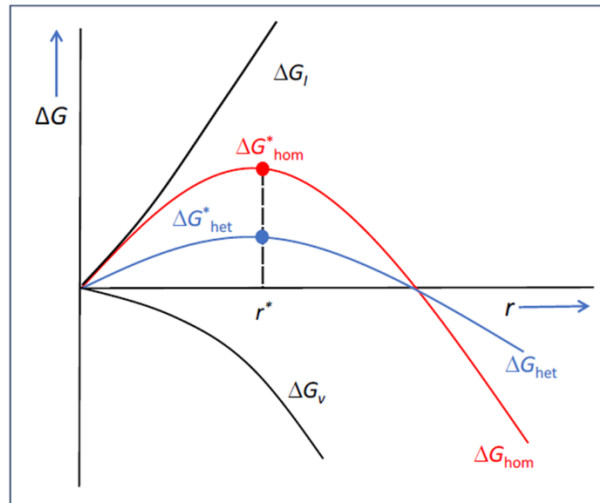


Figure 3. Energy difference for homogenous and heterogenous nucleation (Fan & Men, 2022).

According to the Fletcher's classical nucleation theory (CNT), condensation frosting is more preferable under most of supercooling conditions. Following droplet condensation and freezing of the condensate droplets, ice propagates as 1) frost spreading through bridging between the frozen droplets, 2) growth of ice dendrites atop frozen drops, and 3) dendrites merging and densification (Figure 41). Recent progress in probing technologies has led to a great development to provide fundamental understanding about condensation frosting. Microscopic characterizations of condensation and icing nucleation kinetics, dynamics of ice bridging, and growth mode of ice dendrites are among the related topics (Chengzhi Huang, Zhao, & Gu, 2022).

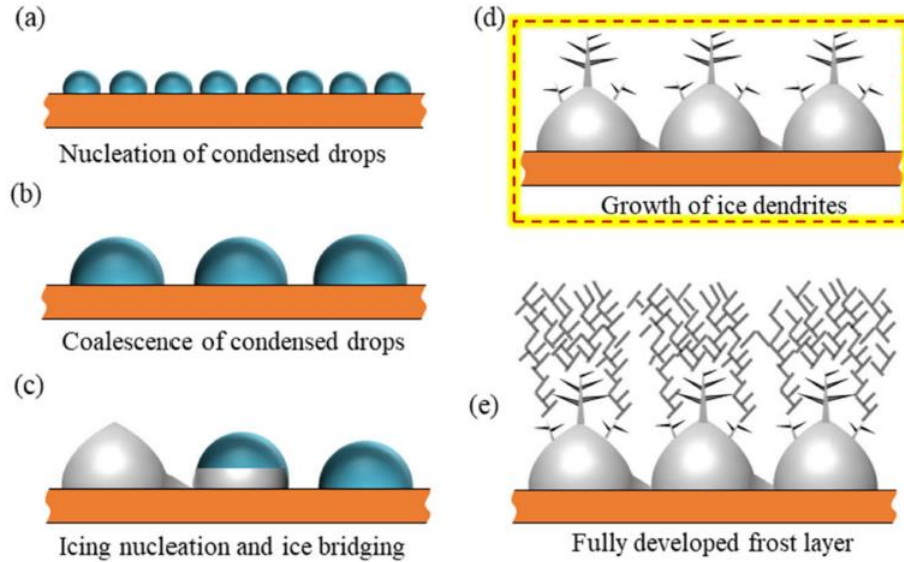


Figure 4. Condensation frosting involving four consecutive stages of a) droplet condensation, b) droplet coalescence, c) ice nucleation and bridging, and d) dendrites growth (C. Huang et al., 2022).

It can be realized that ice dendrite formation is only observed on frozen condensates while the inter droplets gaps remain dry and require ice bridging. As this stage plays a substantial role in the properties of the fully developed frost layer, investigating the governing parameters in ice bridging and the behavior of dendrites growing on top of the frozen condensates becomes very important. Therefore, these two phenomena have been the focus of several studies along with the thermodynamics of icing (C. Huang et al., 2022).

## 2.2. De-icing techniques

Ice crystallization and ice formation are major drawbacks that considerably hinder the productivity of industrial machinery and equipment in cooling systems. The ice nucleation activity and freezing particles significantly reduce the system efficiency in a wide

range of industrial equipment such as refrigerators, heat exchangers, power transmitters, and aerodynamics such as wind turbines, helicopters, and aircraft (Radermacher & Kim, 1996). It is therefore essential to integrate ice preventing mechanisms with the least energy requirement and remarkable efficiency to prevent ice formation at interfaces or elsewhere. The formation of ice introduces excess thermal resistance as a result of the outer ice layer resulting in deterioration in machine functioning (Moser, George, Zangl, & Brasseur, 2009). On the other hand, accumulated ice layers reduce safety in engineering applications. Slippery pavements, changing the hydrodynamics of the surface of aircraft including wings, airfoils, and rotors, and separating ice layers from wind turbines are examples of human safety issues and catastrophic events. Therefore, rigorous efforts have been made to understand the icing and de-icing mechanisms (Heydarian, Jafari, & Momen, 2021; W. Li, Zhan, & Yu, 2021; Lv, Song, Jiang, & Wang, 2014). Although several anti-icing and de-icing methods and materials have been developed, the conventional approaches are often costly, ineffective, and most importantly, are not environmentally friendly (Muthumani et al., 2014). Anti-icing and de-icing processes can be categorized into passive and active modes. The passive method takes the advantage of physical properties of the surface, while the active method relies on external systems, which require an energy supply.

### 2.1.1 Active ice protection techniques

Active methods can be generally sorted into three main categories of thermal, mechanical, and chemical methods.

#### 2.1.1.1 Thermal de-icing methods

Thermal active methods are aimed to increase the surface temperature above the freezing point in order to melt the accumulated ice. **Hot airflow layer** is one of the well-known thermal active methods (Ilinca, 2011). This method which has been extensively used

for turbine blades creates a circulation of hot air inside and on surface through the small holes(Sørensen, 2011). The substantial temperature limitation due to low thermal resistance of materials (polymers and carbon fibers) is one of the shortcomings of this approach (Khadka, Subeshan, & Asmatulu, 2021). Scientists have proposed an approach to protect polymeric materials during active heating by using thermal pad and foils, however, significant change in aerodynamics of the blades and the overall performance was the major drawback of this method (Dalili, Edrisy, & Carriveau, 2009; Hung, Dillehay, & Stahl, 1987).

Performing de-icing on aircrafts has been a challenge for years. **The hot air injection** method has been commonly recruited for aircrafts and wind turbines as well (Cao, Tan, & Wu, 2018). The hot air injection is made of a heating blower and a monitoring system. However, various parameters including the thermal conductivity of the material, wall thickness, geometry and size of the blades, and temperature of the hot air can affect the efficiency of the hot air technique (Gantasala, Luneno, & Aidanpaa, 2016; B. Li, He, Liu, Luo, & Zhang, 2019).Although studies have shown promising results for the hot air injection method, this technique is highly affected by meteorological conditions and surface size and a reduction in the efficiency could be observed in case of severe icing in large scales (Bu, Lin, Yu, Yang, & Song, 2013). Furthermore, low thermal conductivity and thermal aging of polymer composites makes the hot air injection a quite ineffective de-icing method (Bu et al., 2013).

**Electrical heating elements** are another active heating technique. The type of the heating elements, position and possible configuration of the resistors are the parameters that should be taken into account while implementing this method (Mayer, Ilinca, Fortin, & Perron, 2007). Generally, electrical heating systems are made of a control system, an energy supply device, and a heating element. The heaters can be positioned internally or externally with respect to the surface. In wind turbines, the heating elements can be made of a mesh of electrical wires or carbon fibers which can be laminated or glued to the blade's outer surface and covered by a layer of polymer or polymer composite in order to increase the mechanical durability (T. Gao, Luo, Zhou, & Yang, 2021). However, the entire turbine blade does not have the same icing behavior and therefore the required power for de-icing varies locally. This necessitates the implementation of different monitoring strategies for the surface which

requires complicated wiring networks (Pourbagian & Habashi, 2013). Electrical heating systems have been widely used in Finland, Japan, and Switzerland for years (W. Huang, Huang, Guo, & Liu, 2022). However, significant dependence on the thermal resistance and low mechanical integrity (detachment of the elements through heating) and induced surface roughness are the major drawbacks of this method. Therefore, the use of this method has been significantly reduced during recent years (Madi, Pope, Huang, & Iqbal, 2019; Shen, Wang, Lin, Bu, & Wen, 2020). **Microwave heating** and **infrared heating** are other active heating methods that have been used for aircrafts and wind turbine blades (Borigo, 2014; Hansman Jr, 1982).

#### 2.1.1.2 Mechanical de-icing methods

**Expulsive methods** recruit electromagnetic or piezoelectric pulses to break ice and lead to the ice removal. **Electromagnetic de-icing systems** consist of spiral coil placed on the inner side of a metallic surface in order to glue a composite of conductors and dielectric materials to the surface. As a specific amount of ice is accumulated on the surface, the monitoring system sends a signal, and the discharge circuit is turned on. A constantly changing magnetic field is generated by the capacitor, which leads to the creation of eddy currents in the metallic part. The impulse force makes the surface vibrate, which results in the separation of the ice from the surface. This de-icing technique has been applied to aircrafts as well as wind turbine blades, and the results indicate the ice removal up to 84% (Landry, Beauchemin, & Venne, 2000). Electromagnetic de-icing systems are mostly environmentally friendly, efficient and easily to operate, have low energy consumption, and capable of removing large masses of ice (Yousuf, Khawaja, & Virk).

**Pneumatic methods** are used to remove the ice from the leading edges of the aircraft wings. In this technique, ice break off occurs as compressed air pulses inflate and deflate the air chambers consecutively (Mayer et al., 2007). Pneumatic methods are implemented to wind turbine blades as well. In this case, the system is placed on the blade's surface, and as

the expansion tube and airbag on the surface are expanded or ejected, the accumulated ice is removed (Wei, Yang, Zuo, & Zhong, 2020). Normally in case of no ice, tubes are flat and attached to the deicers while covering the icing areas (Aboubakri et al., 2021; Parent & Ilinca, 2011). As the ice mass reaches as a certain amount, the compressed air inflates the deicers and cracks the ice layer which results in ice removal from the surface [66]. This technique is simple and energy-efficient; however, it is not practical for wind turbine blades. Since the deicers are attached to the surface, they induce roughness to the surface which can directly affect the aerodynamic drag of the blades. This method can be problematic for aircrafts in the same way. As the deicers deform over a period of time and they can influence the aerodynamics of the aircraft as well. Additionally, noise generation and intensive system maintenance are reported for this approach (Wei et al., 2020).

**High-velocity fluids methods** such as water and steam jets are used for removing frost from marine structures, open frozen pipes, and surfaces such as concretes which have high durability (Zichen Zhang, Lusi, Hu, Bai, & Hu, 2021). However, in case of more delicate materials such as composites and plastics, and brittle materials such as glass, low-pressure air systems remove the ice (Wyderski, Lozada-Ruiz, Ryerson, Davila, & Tarazano, 2003). For instance, for ice removal in aircraft and wind turbine blades, small volumes of de-icing fluid are injected into the air stream along with the heating and leads to the ice removal (Ryerson & Koenig, 2003). However, this method has some shortcomings such as incapability of removing large masses of ice from rigid and complicated components.

**Ultrasonic technology** has been used in non-destructive testing for years, many research efforts focused on active ultrasonic de-icing (Z. Wang, 2017). Ultrasonic de-icing has been vigorously investigated under laboratory conditions for de-icing on wind turbine and aircraft (X. Zhao & Rose, 2016). Although laboratory experimental results are promising, many technical issues are required to be resolved in order to investigate this method under actual conditions. It is aimed to break the adhesion bond between ice and protected surface in this technique. The contact area of the ice and protected surface, temperature and surface roughness can affect the ice adhesion to the surface.

Shear horizontal wave (SHW) and ultrasonic guided wave (UGW) are commonly used in ultrasonic de-icing methods (Yibing Wang, Xu, & Huang, 2017). Shear horizontal

wave (SHW) and lamb wave are used to generate interfacial transverse shear stresses between the substrate and ice layer. When the applied shear stresses are larger than the ice adhesion strength, the ice layer breaks and is detached from the surface. Furthermore, ultrasonic guided wave (UGW) can result in the local melting of ice and in the formation of small water droplets at the interface, where the ultrasonic cavitation bubbles can intensify the ice separation effect (Yibing Wang et al., 2017).

### 2.1.1.3 Chemical de-icing methods

Although chemical de-icing methods have been extensively used in different applications addressing environmental issues and materials corrosion has still remained as a challenge (Zichen Zhang et al., 2021). The chemicals can be applied either before icing or after a certain amount of ice forms. De-icing chemical agents include several chlorides, formates and acetates, namely sodium and calcium chlor-rides, magnesium chloride, calcium magnesium acetate, potassium acetate, potassium formate, sodium acetate and sodium formate (Rashid, Khawaja, & Edvardsen, 2016). The selection of chemicals for de-icing depends on the application condition and the protected surface properties. For instance, sodium chloride is ineffective at lower temperature and has corrosive properties. Some of these chemicals tend to absorb the moisture and lead to slippery residuals on the surfaces, which can cause hazard. Spraying is one of the common ways of applying de-icing chemicals onto the surfaces. This method has been practical for marine structures and walkways. However, de-icing chemical methods are not very common for aircrafts and wind turbine blades.

Active de-icing methods have been an inseparable part of the de-icing procedures in industry (Gurumukhi et al., 2020). However, high energy consumption, low efficiency, complicated monitoring systems, maintenance costs, mechanical integrity, heaviness have been major setbacks of these methods. Furthermore, initialization of active-icing networks in critical applications may cause serious interference with the systems performance (Hai

Wang et al., 2023a). Therefore, prevention methods or manipulative approaches which can affect icing in terms of delay in the phase change or easier ice removal are more effective.

### 2.1.2 Passive ice protection techniques

Passive technologies mainly use the physical and chemical properties of the surface to lower the risk of icing by causing delay in the ice formation and accumulation or any phenomena which can induce icing (Figure 5). The interfacial properties of ice and surfaces are of great importance and have been the focus of many scientific studies. The main idea of these techniques is the protection of surfaces from icing and the associated problems in a more efficient way with no further need for external energy.

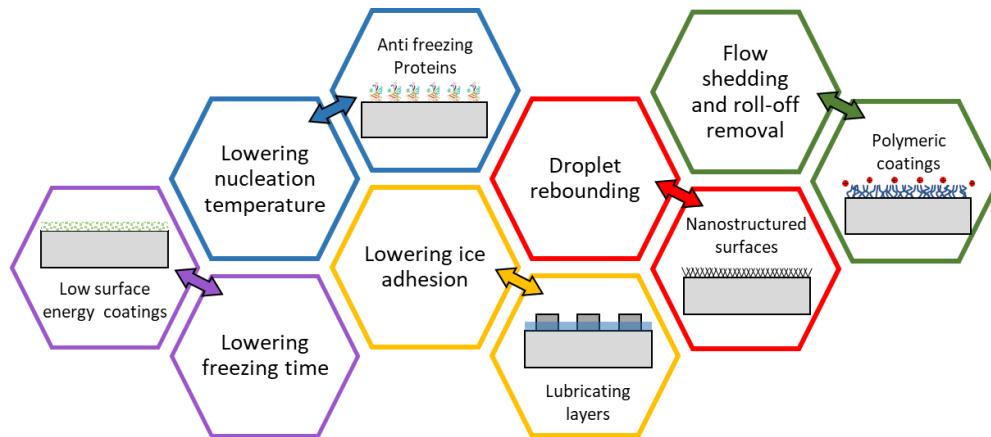


Figure 5. Major passive anti-icing mechanisms with examples.

Many studies have been focused on developing anti-icing passive techniques (Gharib, Saeidiharzand, Sadaghiani, & Koşar, 2021). The development of **superhydrophobic surfaces** is one of the extensively used approaches in different applications (Kreder, Alvarenga, Kim, & Aizenberg, 2016). Superhydrophobic surfaces, inspired by lotus leaves, are referred to the surfaces having contact angles higher than  $150^\circ$  (Onda, Shibuichi, Satoh, & Tsujii, 1996). These bionic surfaces have contact angle

hysteresis smaller than  $10^\circ$  or less than  $5^\circ$  according to some references (Barthlott & Neinhuis, 1997; Kreder et al., 2016; Q. Li & Guo, 2018; Onda et al., 1996). Properties such as self-cleaning (Fürstner, Barthlott, Neinhuis, & Walzel, 2005; Y. Gao, Sun, & Guo, 2014; J. Li, Wan, Ye, Zhou, & Chen, 2012), drag reduction (Shirtcliffe, McHale, Newton, & Zhang, 2009; Y.-Y. Song, Schmidt-Stein, Bauer, & Schmuki, 2009), good resistance to corrosion (Xu & Wang, 2009; Yin, Liu, Chen, Liu, & Cheng, 2008), along with the anti-icing behavior, have made superhydrophobic surfaces one of the most practical surfaces in different industries (Farhadi, Farzaneh, & Kulinich, 2011; Tourkine, Le Merrer, & Quéré, 2009). Superhydrophobic surfaces can be fabricated by the combination of a hierarchy of micro- and nano-scale surface structures and modification of low surface energy chemistry (X. Deng et al., 2011; Kwak, Seol, Tak, & Yong, 2009; J.-P. Lee, Choi, & Park, 2011). Techniques such as anodic oxidation, chemical and electrochemical methods, laser etching (Lu et al., 2012; Qian & Shen, 2005; J. Song, Xu, & Lu, 2012), and deposition (A. P. Deng & Wu, 2012) have been used by scientists to develop superhydrophobic surfaces. For instance, Gao et al. (Y. Gao et al., 2014) fabricated Ti-6Al-4V superhydrophobic surfaces with high durability and good resistance to abrasion through an economic process of anodizing. They developed micro-structured Ti-6Al-4V surfaces with a contact angle of  $158.5^\circ$  and a contact angle hysteresis of  $5.3^\circ$ . Despite of commonly developed surfaces, the resulting surfaces in this study have a low roughness of  $R_a = 0.669$ .

**Slippery liquid infused porous surfaces (SLIPS)** are another bionic strategy in anti-icing applications (Chaowei Huang & Guo, 2019). SLIPs, inspired by *Nepenthes* pitcher plants, are developed by infusing a slippery lubricant into a textured solid surface. The slippery nature of the SLIP not only results in easier water droplets shedding from the surface in the presence of a slight force (such as gravity force due to a slight tilt or blow of wind in harsh environment) but also results in a weaker ice adhesion (C. Wang & Guo, 2020).

In order to evaluate the performance of these two conventional strategies in anti-icing applications, providing insight about anti-icing mechanism is of great importance. As mentioned previously, the vapor–liquid–solid transition is dominant in relatively wide ranges of temperature and pressure in many anti-icing applications (Libbrecht, 2017; Schutzius et al., 2015). Water repellency of a surface is one of the critical features that can prevent ice

formation through this transition. Condensation and accumulation of water droplets on a surface are influenced by this important feature (Q. Li & Guo, 2018). Due to the higher contact angle of superhydrophobic surfaces (more than  $150^\circ$ ) compared to SLIPs, this stage and following ice formation are delayed on these surfaces. Superhydrophobic surfaces are developed based on the Classical Cassie–Baxter (CB) model on water wettability (Cassie & Baxter, 1944; Wenzel, 1936). In contrast to Wenzel model, where the contact areas are relatively large, in CB model water droplets do not wet the droplet-substrate interface fully and continuously (Erbil & Cansoy, 2009). The interface is a composite of the peaks of the solid substrate pattern and air pockets which are trapped due to the specific topography of the hydrophobic surface. The smaller contact area in the CB state leads to low friction between the droplet and substrate with increased droplet mobility on the surface. Therefore, the bouncing of droplets can be observed upon their impact on superhydrophobic surfaces (X. Yu, Zhang, Hu, & Luo, 2021). Furthermore, the droplets can be removed due to external forces (Kreder et al., 2016; Wen & Ma, 2020a). The droplet removal in various directions can be observed on the superhydrophobic surface, while the droplets only roll of the surface for SLIPs (C. Wang & Guo, 2020). However, it should be mentioned that water penetration inside superhydrophobic surfaces cavities can occur after progressive nucleation and coalescence when exposed to near-saturated vapor (F. Wang, Ding, He, & Zhang, 2019; Zhuo, Wang, Xiao, He, & Zhang, 2018).

In terms of icing, ice formation still occurs and propagates over the surface through icing waves. Due to the low surface energy of superhydrophobic surfaces, the growth of the icing front is an order of magnitude slower on superhydrophobic surfaces than on SLIPs. Moreover, the detachment of the droplets or the ice from the SLIPs results in considerable loss of lubricant and functionality deterioration (Long et al., 2020).

The development of SLIPs requires more complicated processes which usually contain hazardous and costly lubricants materials such as perfluoropolyethers or perfluorinated. Also, researchers have been successful to develop superhydrophobic surfaces with good anti-fouling and anti-corrosion properties (He, Yang, Mu, Wang, & Lan, 2022; Xue, Guo, Ma, & Jia, 2015). Taking all of this into account, SHSs have been extensively

used under different conditions despite the limited application of SLIPs (Tenjimbayashi et al., 2018; Yao et al., 2015; J. Zhang, Wang, & Seeger, 2014).

Janjua et. al. (Janjua et al., 2017) studied the development of micro-nano-structured superhydrophobic coatings for aerospace applications. The maximum contact angle reported by the authors was  $154^\circ$  on a 20% functionalized carbon nanotube coated sample. Accordingly, a very low initial ice adhesion was observed in this study. Another attempt to develop superhydrophobic coating with high durability was done by Tong et. al. (Tong, Xiong, Wang, Wu, & Zhou, 2019) who recruited self-assembled deposited nanoparticles for the development of anti-icing coating of aerospace composite materials. The relatively high contact angle of both water and acid or alkaline along with good stability was reported for this hierarchical structured coating having low surface energy. Most importantly, promising anti-icing in terms of i) delay in ice accretion by 120 min and ii) relatively low ice adhesion strength as 53.6 kPa was observed by the authors. Jiang et al. (Jiang, Chen, Zhang, & Huang, 2018) developed a micro-nano-structured superhydrophobic SiC/CNTs coating. The water contact angle of  $161^\circ$  and a significantly low roll angle of  $2^\circ$  were reported for the developed coating. SiC/CNTs coating not only exhibited a reduction in ice adhesion strength but also assists in anti-icing due to the photothermal properties of CNT.

Although many studies have been performed on superhydrophobic surfaces, development of a superhydrophobic coating for real life industrial applications has still remained as a challenge. The developed method is complex and multistep. In addition to high cost and multiple-step procedures, these methods usually require special devices and specific conditions (Barthlott & Neinhuis, 1997; C. Wu et al., 2017; Yeom & Kim, 2016). Easy applicability of the coating on large scale for aircrafts or wind turbine is another major issue in the development of such coatings. Furthermore, although mechanical durability of the coatings has been discussed, maintaining the superhydrophobic behavior of the coatings in relatively high humidity is another important issue which requires to be taken into account. Limited by complex fabrication procedures, a facile, low-cost, and scalable coating method is of great importance (Hooda, Goyat, Pandey, Kumar, & Gupta, 2020; Kobina Sam et al., 2019; W. Li et al., 2021; Parvate, Dixit, & Chattopadhyay, 2020). In this regard, the

development of superhydrophobic coatings containing nanoparticles can be a good substitution for existing conventional time-consuming, and complex processes.

Titanium oxide (TiO<sub>2</sub>) and silicon oxide (SiO<sub>2</sub>) nanoparticles have been used to provide superhydrophobic coatings by producing a hierarchical surface structure as an addition to a low surface energy material (Lu et al., 2015; Qing et al., 2016; L. Zhao et al., 2014; Zheng, Bellido-Aguilar, Huang, et al., 2019; Zheng, Bellido-Aguilar, Wu, et al., 2019). Due to the inherent hydrophilicity of SiO<sub>2</sub>/TiO<sub>2</sub> nanoparticles, polymeric materials such as PDMS and resins are generally required to be used as a matrix to create low surface energy in such coatings (Kamegawa, Shimizu, & Yamashita, 2012; Saharudin et al., 2018; Sharifi, Pugh, Moreau, & Dolatabadi, 2016; X. Zhang, Geng, Guo, Zhang, & Zhang, 2013; Zhaozhu Zhang, Ge, Men, & Li, 2016). Uneven dispersion or aggregation of particles is one of the common problems with these composite coatings and needs to be dealt with sensitivity (Sreekantan, Yong, Basiron, Ahmad, & De'nan, 2022). Moreover, contact angles reported for superhydrophobic SiO<sub>2</sub>/TiO<sub>2</sub> nanoparticle based coatings are around 150°, and complex processes are required to enhance their performance (Hengzhen Chen, Zhang, Zhang, & Zhang, 2012; Latthe & Rao, 2012; Yan et al., 2020).

Recently, metal organic frameworks (MOFs) have attracted much due to their significant properties, such as ordered porosity, high internal surface area, low density, and adjustable structure. Zeolitic imidazolate frameworks (ZIFs), a subclass of MOFs, are highly porous and crystalline materials having zeolite-like structures, which are formed by divalent metal ions nodes and imidazolate ligands. Among this family, ZIF-8 consists of tetrahedrally coordinated Zn<sup>+2</sup> bridged by 2-methylimidazolate linkers and exhibits sodalite (SOD) topology. ZIF-8 is comprised of micropores located in the center, which comprises micropores located in the center accessible through six-membered windows (Feng, Zhang, Shi, & Wang, 2021; Y.-R. Lee et al., 2015). On a ZIF-8 based coating, the distinctive porous and cage-like structure of the nanoparticles has not only an important role in the superhydrophobic behavior of the coating in terms of creating more air packets and superhydrophobicity but also causes higher durability against moisture penetration compared to conventional coatings based on SiO<sub>2</sub> and TiO<sub>2</sub> nanoparticles. Figure 6 indicate the porous structure a coating based on ZIF-8 nanoparticles.

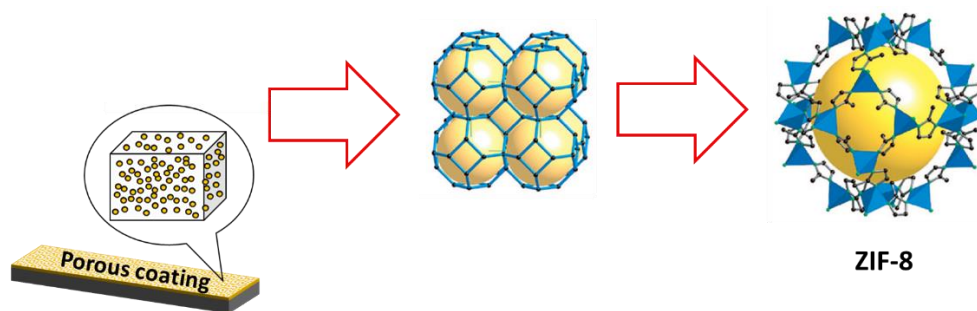


Figure 6. Superhydrophobic coating based on porous ZIF-8 nanoparticles.

Furthermore, ZIF-8 is an intrinsically highly hydrophobic material, mainly due to the presence of the imidazolite rings in its structure (S. Chen et al., 2019; Sann, Pan, Gao, Zhan, & Xia, 2018). This significantly contributes to the water repellency of ZIF-8 based coatings in terms of creating low surface energy. Therefore, ZIF-8 nanoparticles can solely create significant superhydrophobic effects due to their extraordinary structure and nature.

Moreover, excellent chemical and thermal stability, good flexibility for structure and surface modification, adjustable particle size, modifiable pore size, and environmentally friendly synthesis process offer the opportunity to develop coatings with additional functionalities for critical applications, especially for anti-icing applications (N. Nordin et al., 2014; Y. Pan, Liu, Zeng, Zhao, & Lai, 2011).

On the other hand, evaluation of anti-icing performance under various conditions and detecting the interfacial phenomena on superhydrophobic coatings are substantial to develop effective anti-icing surfaces for different applications. Numerous studies have been conducted on static icing of superhydrophobic coatings (C. Chen et al., 2022; Haipeng Wang, He, Liu, & Guan, 2019; Yushun Zhao, Yan, Hou, Dou, & Shen, 2022). These studies mainly focus on static icing conditions such as (sub)millimetric droplet (Nine, Tung, Alotaibi, Tran, & Losic, 2017) and film (N. Wang, Xiong, Deng, Shi, & Wang, 2015) icing and utilized simple hydrothermal analysis on the anti-icing nature of the superhydrophobic coating (Y. Li, Li, Zhao, Tian, & Zhang, 2018). A detailed analysis of the effect of surface chemistry and texture on mechanisms behind the superhydrophobicity of the coating such as Laplace pressure within the structure, non-wetting mechanism, condensation-induced icing mitigation approaches, and ice growth direction is necessary (Kim, Lee, Kim, & Kim, 2015;

R. Pan, Zhang, & Zhong, 2021; Watson et al., 2017). Most importantly, ice formation is dictated by impacting droplets on supercooled surfaces in many industrial applications (P. Jin et al., 2022; Schremb, Roisman, & Tropea, 2018; D. Song, Jiang, Chou, Asawa, & Choi, 2020). At high surface supercooling temperatures, the droplet contact time is longer than the freezing timescale. The freezing-governed hydrothermal interaction between the droplet and supercooled surface and the dynamics of the three-phase contact line (droplet/surface/air) are still poorly understood at supercooled surface temperatures (Q. Li & Guo, 2018; Yuanyi Wang, Xue, Wang, Chen, & Ding, 2013; T. Wu, Xu, Guo, Xie, & Qu, 2021; Y. Zhao et al., 2020). For instance, although advancing and receding contact angles do not vary with the contact line speed on non-wetting surfaces followed by complete rebound under isothermal conditions (Bayer & Megaridis, 2006), three-phase contact line dynamics and contact angle hysteresis on supercooled conditions require more analysis. The effective design of anti-icing surfaces requires an understanding about transient thermal transport through the droplet/surface interface, which is governed by hydrothermal characteristics of the contact line during the impact process.

**Biphilic surfaces** are another category of engineered surfaces that can be used for certain anti-icing applications. Although superhydrophobic surfaces have shown an outstanding performance in hampering icing, they cannot prevent ice formation completely and by sufficient time, ice crystals nucleate and cover the entire the surface (Nath, Ahmadi, & Boreyko, 2017). Another limitation of superhydrophobic surfaces for their implementation into industrial applications is related to the systems such as ventilation, air-conditioning, and refrigeration. In more practical systems such as heat pumps and refrigerators, surfaces are prone to condensation frosting as condensation is a critical part of the process (Hou et al., 2018). In order to maintain the energy efficiency, it is necessary to prohibit ice formation and accumulation without degrading the condensation capacity of the surfaces. Therefore, using fully superhydrophobic surfaces for such application may not be a practical solution in terms of the whole system's performance (Pérez-Lombard, Ortiz, Coronel, & Maestre, 2011; Vocale, Morini, & Spiga, 2014).

Furthermore, in order to provide a completely ice-free surface in industrial systems the need for active methods is inevitable. Three active de-icing techniques are currently used in industry: oscillation ultrasonic vibration, electro-hydrodynamics (EHD), and system

defrosting (Kazunari Adachi, Saiki, & Sato, 1998; Kazunari Adachi, Saiki, Sato, & Ito, 2003; Schaefer & Langmuir, 1953). Due to the high costs of EHD and vibration, system defrosting is commonly used. In system defrosting, the fluid is heated through reversal of the cycle direction (Ding, Ma, Chai, & Jiang, 2004). However, up to 27% of the total heat input is used for heating the evaporator, and up to 75% of the defrosting energy is spent on heating the refrigeration system and not the frost (STOECKER, Lux Jr, & Kooy, 1983). After defrosting, water retention is usually observed on surfaces which can reduce the overall heat-transfer coefficient by up to 20% and act as a stimulating layer for next icing cycle (Xia, Hrnjak, & Jacobi, 2005). Furthermore, water retention in long term leads to material degradation, corrosion and loss of performance of the materials which causes additional cost, energy, and waste for maintenance and even reproduction of materials.

Taking all of these into account, 1) the compromise between condensation and icing, 2) inevitable need for auxiliary active methods, and 3) water retention after de-icing highlight a crucial need for proposing alternative anti-icing surfaces.

The use of hybrid biphilic surfaces for anti-icing applications was proposed first by allocating sacrificial hydrophilic domains across the surface to keep superhydrophobic regions dry (Ahmadi et al., 2018). As an example, Gurumukhi et. al. (Gurumukhi et al., 2020) proposed hydrophilic stripes through the surface to create the complete cleaning of the superhydrophobic areas. They performed de-frosting by setting the chiller at higher temperature (about 20°C) or heating the samples via strip heaters. Biphilic surfaces having hydrophilic stripes with the thickness of 1mm ( $L_{HL} = 1 \text{ mm}$ ) and superhydrophobic with thickness of equal or less than 4 mm ( $L_{SHP} \leq 4 \text{ mm}$ ) showed enhanced de-icing behavior while water retention was observed on the biphilic surfaces with  $L_{SHP} > 4 \text{ mm}$ . Wang et. al (Hai Wang et al., 2023b) performed a similar study which proposes a different biphilic design for the same purpose. Square shaped superhydrophobic regions on a hydrophilic substrate with the spacing of 2 mm resulted in the best evaporation mediated surface cleaning. However, in both studies, hydrophilic regions were proposed to only clean the superhydrophobic regions while the domain dimension is considerably large. Furthermore, the complete cleaning of the entire surface was assisted by evaporation (additional heating).

Meanwhile, Boreyko et. al (Boreyko et al., 2013) provided a more thorough study on interfacial phenomena during de-frosting on a superhydrophobic surface.

This thesis proposes a functionalized multiscale superhydrophobic coating based on Zeolitic imidazolate frameworks which have superior anti-icing performance due to the outstanding nonwetting mechanisms generated by its unique physical and chemical properties. Furthermore, this thesis describes fundamental studies on both static and dynamic icing behavior of the coating by simulating the real industrial conditions in order to provide a thorough insight into the interfacial phenomena occurring on a multiscale (micro-nano-sub nano) superhydrophobic surface structure. The proposed functional ZIF-8-based superhydrophobic multiscale shows a relatively high contact angle ( $CA < 172^\circ$ ) compared to the literature. Additionally, the reported contact angle hysteresis for this coating is significantly low ( $CAH < 3^\circ$ ). The coating enables droplet induced jumping and an outstanding reduction in interfacial heat transfer which results in excellent anti-icing behavior. Furthermore, due to the dense surface morphology and the presence of hydrophobic micropores on ZIF-8 nanoparticles, significant superhydrophobicity durability is observed on this coating which is a crucial superiority along with chemical and thermal stability and can reduce the costs related to maintenance and reapplications. More importantly, the coating is developed through the practical spray coating method which can be effectively applied in industrial systems such as wind turbine blades.

Furthermore, this thesis proposes an optimum biphilic surface design consisting of superhydrophobic islands surrounded by hydrophilic regions for de-icing. The proposed biphilic design with certain geometrical properties enables passive cleaning due to the Laplace pressure gradient generated by the surface pattern. The biphilic design is aimed to create an ice/water-free surface after de-icing with no need for further heating which can contribute to a reduction in energy consumption during de-icing and the risk of water retention after de-icing. The optimum design is also investigated based on its influence on ice formation and propagation. The presence of superhydrophobic regions not only causes a delay in ice formation and growth but also affects the ice structure. Ice forms a porous structure on superhydrophobic islands due to the larger distance between the ice nuclei and more challenging bridging between the frozen droplets while a more dense and

interconnected ice structure is observed on hydrophilic regions. This leads to the formation of a nonuniform layer of ice on biphilic surfaces which makes it more prone to melting and easier removal.

### Chapter III: Development of a multiscale superhydrophobic zeolitic imidazole framework-based coating

#### 3.1. Introduction

This chapter proposes and discusses the development of a multiscale superhydrophobic zeolitic imidazolate framework (ZIF-8) based coating (SHMC). SHMC led to contact angle larger than  $172^\circ$ , rolling angle less than  $5^\circ$ , and contact angle hysteresis smaller than  $3^\circ$ . The coating was successfully applied to metallic and composite substrates using the practical spray coating method.

## 3.2. Experimental methods and procedure

### 3.2.1. Materials

2-methylimidazole (Hmim, 99%), 1H,1H,2H,2H-perfluorooctyltriethoxysilane (PFOTES, 97%) and zinc nitrate hexahydrate ( $\text{Zn}(\text{NO}_3)_2 \cdot 6\text{H}_2\text{O}$ , 99%) were purchased from Sigma Aldrich. The other chemicals such as absolute ethanol, n-hexadecane, and acetone were purchased from Sigma Aldrich and were used without any further purification. Deionized water (DI water) purified by water purification system was used for all the aqueous solution preparations. Copper (purity  $\geq 99.5\%$ ) and Aluminum were used for the metallic substrates.

### 3.2.2. Synthesis of ZIF-8 nanoparticles

ZIF-8 nanoparticles were synthesized in an aqueous system at room temperature. 1.17 gr  $\text{Zn}(\text{NO}_3)_2 \cdot 6\text{H}_2\text{O}$  was dissolved in 8 ml DI water while 22.70 gr 2-methylimidazole was dissolved in 80 ml DI water. The zinc nitrate solution was poured into the 2-methylimidazole solution and was mixed with a magnetic stirrer to prepare the synthesis solution with the molar ratio of  $\text{Zn}^{2+}$  2-methylimidazole:  $\text{H}_2\text{O}$ =1:70:1238. After two hours of stirring for 2 hours at room temperature, the product was collected by centrifuge. The nanoparticles were then washed with DI water and dried in a vacuum oven at  $85^\circ\text{C}$  for 24 hours. In order to optimize the synthesis process, stirring duration of 45 mins for sample Z-1, 2 hrs for sample Z-2, and 3 hrs for sample Z-3 were proposed and carried out.

In another technique, ZIF-8 nanoparticles (sample Z-3) were synthesized through a microwave assisted approach. The molar ratio of  $\text{Zn}^{2+}$  2-methylimidazole:  $\text{H}_2\text{O}$ =1:70:1238

were kept constant while the synthesis was proposed at 120 °C for 10 mins with the stirring rate of 1200 rpm using a microwave.

### 3.2.3. Preparation of superhydrophobic ZIF-8 based coating

In order to develop a uniform and durable superhydrophobic coating, ZIF8 nanoparticles were first modified by 1H,1H,2H,2H-perfluorooctyltriethoxysilane (PFOTES). 0.5 ml of 1H,1H,2H,2H-perfluorooctyltriethoxysilane (PFOTES) was mixed ultrasonically in 50 ml absolute ethanol for 1 hour. Consequently, 1.5 gr ZIF-8 nanoparticles were dissolved ultrasonically in the as-prepared solution for 30 mins to obtain the coating solution. Metallic Substrates were cut into 30 mm×30mm pieces and polished with sandpaper (up to 2000 grade). Consequently, the substrates were degreased by acetone and cleaned with DI water ultrasonically (for 10 mins each). The coating solution was spray-coated on the substrates using a spray gun. Air pressure of 0.1 MPa and spray distance of 20 cm were the spray coating parameters.

### 3.2.4 Materials characterization

Scanning electron microscopy (SEM) Zeiss Leo Supra 35VP equipped with energy dispersive X-ray spectroscopy (EDX) was employed to characterize the morphology of the nanoparticles, surface structure of the coating, and elemental composition of the materials. X-ray diffraction (XRD) analysis was done by recruiting a Bruker D2 Phaser (Bruker AXS GmbH) by CuK $\alpha$  radiation (wavelength of 1.54 Å) to characterize the crystal structure of ZIF-8 nanoparticles. Infrared spectra were recorded using a Nicolet iS50 FT-IR (Fourier Transform Infrared Spectroscopy) spectrophotometer to confirm the structure of ZIF-8 nanoparticles. The specific surface area and pore volume of crystals were measured using a Micromeritics gas adsorption analyzer instrument equipped with a commercial software for calculation and analysis. The BET surface area was calculated from the adsorption isotherms using the standard Brunauer–Emmett–Teller (BET) equation.

### 3.3 Results and discussion

#### 3.3.1. ZIF-8 nanoparticles

**Sample Z-1:** Figure 7 shows the X-ray diffraction pattern of ZIF-8 nanoparticles synthesized as at different conditions. Three sharp peaks around  $2\theta$  values of  $17.5^\circ$ ,  $25^\circ$  and  $36^\circ$  were observed on the XRD pattern of sample Z-1 which does not match with the characteristic peaks for ZIF-8. For further analysis, SEM observations were carried out on the as-synthesized sample (Figure 8 a-d). SEM images at different magnifications along with the XRD analysis are indicative of the incomplete synthesis of ZIF-8.

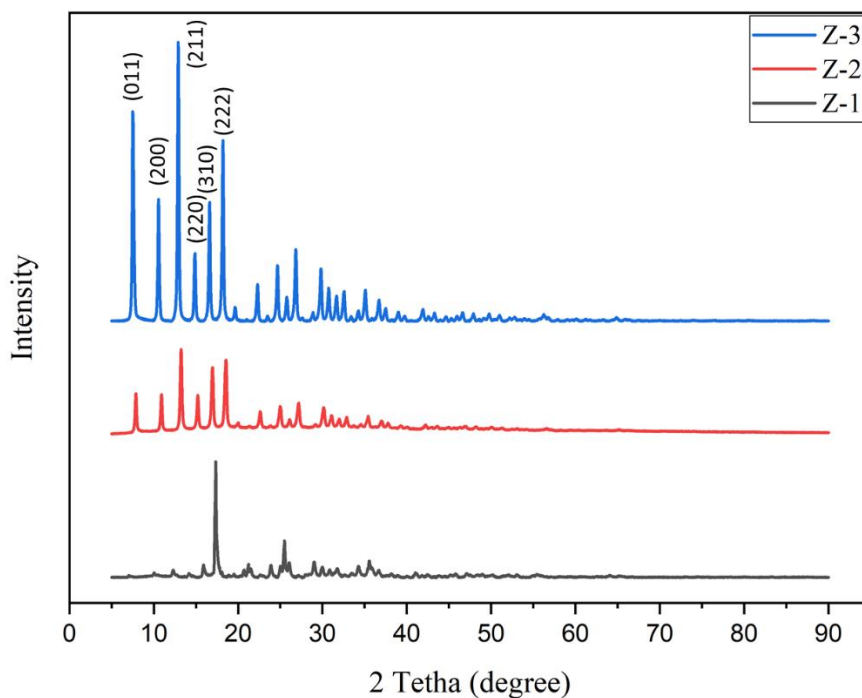


Figure 7. XRD pattern of the as-synthesized ZIF-8 nanoparticles under different conditions.

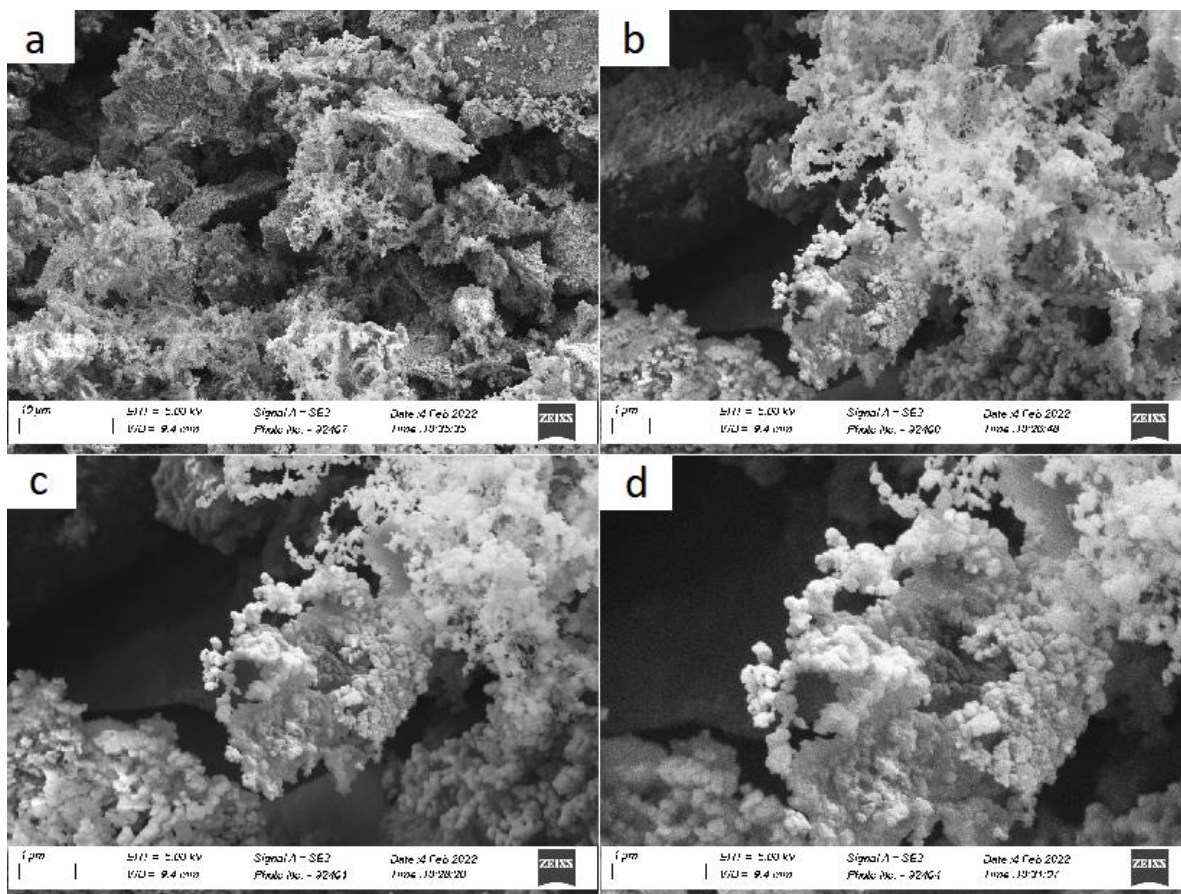


Figure 8. SEM images of sample Z-1.

**Sample Z-2:** As the obtained results from Z-1 synthesis method were not promising, the reaction duration was increased up to 2hr to achieve sample Z-2. XRD pattern of the as-synthesized ZIF-8 nanoparticles in sample Z-2 can be seen in Figure 7 which is in good agreement with the literature (Awadallah-F, Hillman, Al-Muhtaseb, & Jeong, 2019; N. A. H. M. Nordin, Ismail, Misdan, & Nazri, 2017). The presence of well-defined peaks with high intensity is indicative of good crystallinity of ZIF-8 nanoparticles. XRD pattern indicates characteristic diffractions at two thetas of  $6^\circ$ ,  $10.1^\circ$ ,  $13.2^\circ$ ,  $15.2^\circ$ ,  $17^\circ$ ,  $18.5^\circ$ ,  $19.9^\circ$ ,  $23^\circ$ ,  $24.9^\circ$ ,  $25^\circ$ ,  $26^\circ$ ,  $27^\circ$  and  $30^\circ$  degrees corresponding to (110), (200), (211), (220), (310), (222), (321), (411), (332), (431), (440) and (334) planes of the crystalline structure of ZIF-8, respectively. No peak associated with impurities was spotted.

FTIR spectrum of ZIF-8 nanoparticles in sample Z-2 and Z-3 are shown in Figure 10. The spectrum of sample Z-2 shows peaks at  $692\text{ cm}^{-1}$  and  $760\text{ cm}^{-1}$  which corresponds to C–H bending. Peaks at  $995\text{ cm}^{-1}$ ,  $1144\text{ cm}^{-1}$ ,  $1179\text{ cm}^{-1}$  due to =C–H in-plane bending and =C–H in-plane deformation vibration are observed. Furthermore, the peaks at  $1306\text{ cm}^{-1}$ ,  $1428\text{ cm}^{-1}$ ,  $1459\text{ cm}^{-1}$ ,  $1570\text{ cm}^{-1}$ ,  $1677\text{ cm}^{-1}$ ,  $2930\text{ cm}^{-1}$  and  $3132\text{ cm}^{-1}$  represent  $\text{CH}_2$  vibration,  $\text{CH}_3$  bending, asymmetric bending of  $\text{CH}_2$ , C=C stretching, C=N stretching, symmetric stretch of C–H and =C–H stretching in imidazole ring, respectively. The FTIR results are in agreement with the literature (Awadallah-F et al., 2019; Huaiyin Chen, Wang, Fan, Hong, & Li, 2021).

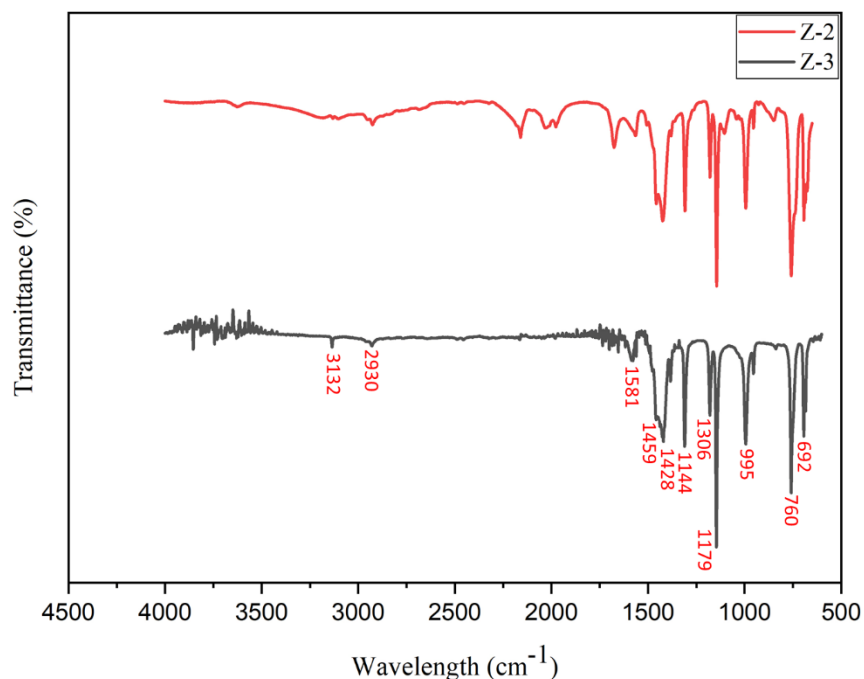


Figure 9. FTIR spectrum for ZIF-8 nanoparticles.

SEM images of sample Z-2 are shown in Figure 11. SEM analysis indicates the nano spherical particles within the range of 50-150 nm. In addition to SEM observations, transmission electron microscopy (TEM) was carried out in order to provide a better understanding about the particle morphology and the size distribution. TEM images (Figure 11) are indicative of nanoparticles having faceted shapes which shows the proper formation

of the crystalline structure of ZIF-8 nanoparticles. The average size of ZIF-8 nanoparticles were measured as 93.83 nm. Both SEM and TEM observations were in good agreement with the literature (Yuan et al., 2019).

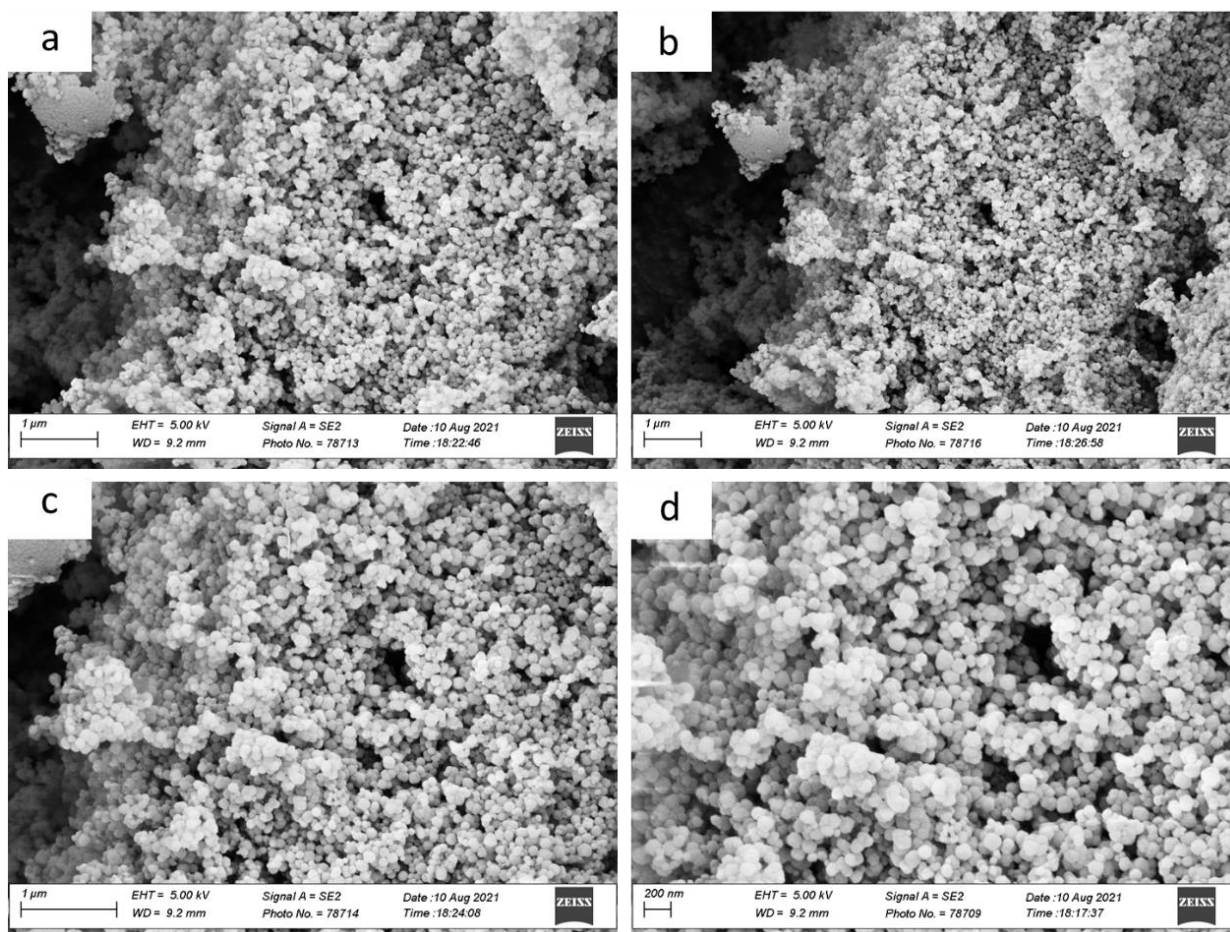


Figure 10. SEM images of the as-synthesized Z-2 in different magnifications.

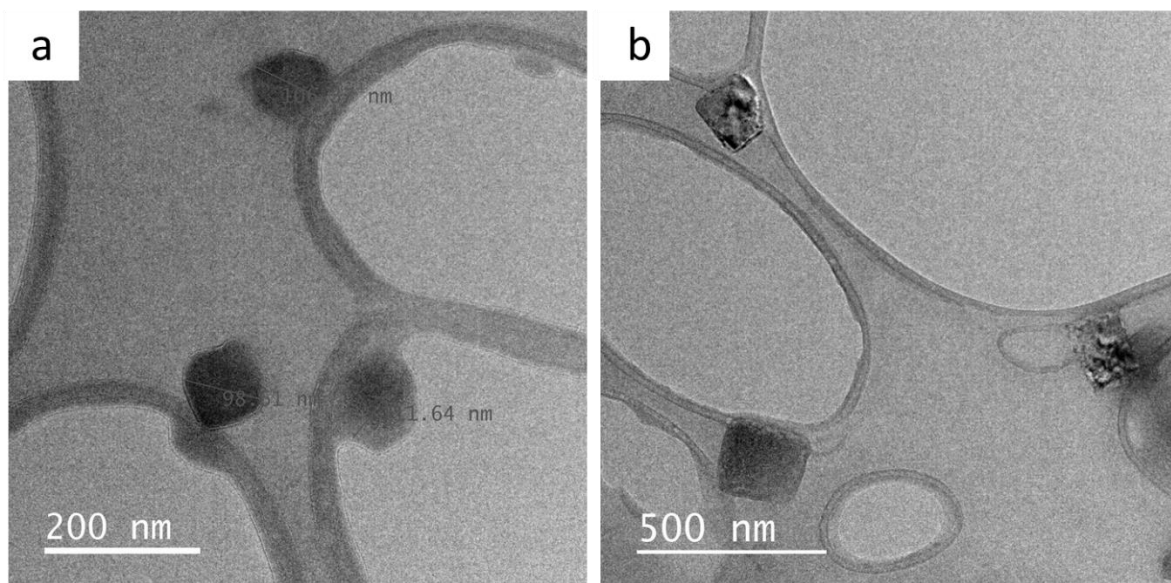


Figure 11. SEM images of the as-synthesized Z-2 in different magnifications.

The  $N_2$  adsorption measurement results are shown in Figures 13a and b. The  $N_2$  adsorption isotherm in Figure 13a indicates type 1 adsorption behavior. The increase in the adsorbed volume at low pressures is linked with the existence of micropores. The micropore volume and Brunauer-Emmett-Teller (BET) surface area are obtained as  $0.4641 \text{ cm}^3 \text{ g}^{-1}$  and  $1173 \text{ m}^2 \text{ g}^{-1}$ , respectively. The results are in good agreement with the reported values in the literature (Y. Pan et al., 2011; Yao et al., 2015). The distribution of micropore size of ZIF-8 nanoparticles was measured using the Horvath-Kawazoe (HK) method. As shown in Figure 13b, three narrow pore size distributions through the pore width range of 0.7- 1.8 nm centered around 0.75 nm, 1.125 nm, and 1.45 can be observed.

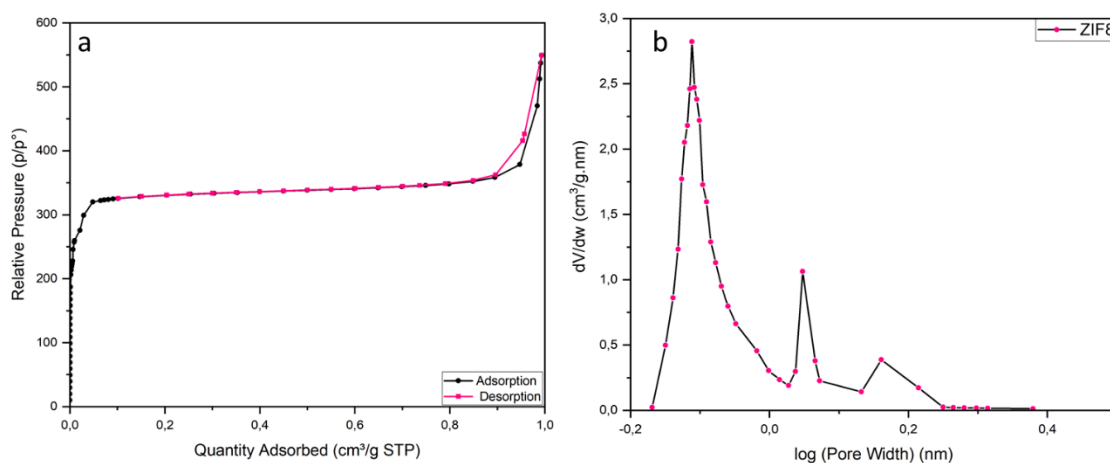
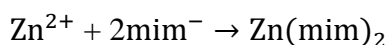


Figure 12. a) Isotherm linear plot and b) Horvath-Kawazoe differential pore volume plot of sample Z-2.

The yield percentage of the products another factor to evaluate the proper synthesis process and can be calculated based on the following equation:

$$\text{Yield} = \frac{m_r}{m_t} \times 100 \quad (1)$$

where  $m_r$  is the actual yield whereas  $m_t$  is the theoretical yield of ZIF-8 based on the below chemical formula:



Since 1.17 gr Zinc nitrate hexahydrate was used as the limiting reactants:

$$1.17 \text{ gr Zn(NO}_3)_2 \cdot 6\text{H}_2\text{O} \times \frac{1 \text{ mol Zn(NO}_3)_2 \cdot 6\text{H}_2\text{O}}{297.5 \text{ gr Zn(NO}_3)_2 \cdot 6\text{H}_2\text{O}} \times \frac{1 \text{ mol Zn}}{1 \text{ mol Zn(NO}_3)_2 \cdot 6\text{H}_2\text{O}} \times \frac{1 \text{ mol Zn(mim)}_2}{1 \text{ mol Zn}} \times \frac{229.60 \text{ gr Zn(mim)}_2}{1 \text{ mol Zn(mim)}_2} = 0.9 \text{ gr ZIF-8}$$

$m_t$  is the theoretical yield of ZIF-8 is equal to 0.9 gr while the product of the synthesis process in a fully aqueous system at room temperature for 2 hours was measured as 0.816 which results in the yield percentage of 90.6%. The yield percentage of the proposed synthesis method is relatively high and in good agreement with the literature (Kida, Okita, Fujita, Tanaka, & Miyake, 2013).

**Sample Z-3:** In order to investigate the effect of the assistance of microwave on the ZIF-8 synthesis, sample Z-3 was produced with the same reactant ratios by using microwave at 120 °C for 10mins with the stirring rpm of 1200. XRD pattern of the as-synthesized sample Z-3 can be seen in Figure 7. The results are similar to the XRD pattern obtained for sample Z-2 and in good agreement with the literature (Awadallah-F et al., 2019; N. A. H. M. Nordin et al., 2017). The well-defined peaks with high intensity indicate good crystallinity of ZIF-8 nanoparticles. XRD pattern indicates characteristic diffractions at two thetas of 7.5°, 11°, 13.5°, 15°, 16.5°, 18.5°, 19.9°, 23°, 24.9°, 25°, 26°, 27° and 30° degrees corresponding to (110), (200), (211), (220), (310), (222), (321), (411), (332), (431), (440) and (334) planes of the crystalline structure of ZIF-8, respectively. No significant impurities were observed.

FTIR spectrum of sample Z-3 is indicated in Figure 10. The spectrum shows peaks at 692 cm<sup>-1</sup> and 760 cm<sup>-1</sup> which corresponds to C–H bending. Peaks at 995 cm<sup>-1</sup>, 1144 cm<sup>-1</sup>, 1179 cm<sup>-1</sup> due to =C–H in-plane bending and =C–H in-plane deformation vibration are observed. Furthermore, the peaks at 1306 cm<sup>-1</sup>, 1428 cm<sup>-1</sup>, 1459 cm<sup>-1</sup>, 1581 cm<sup>-1</sup>, 2930 cm<sup>-1</sup> and 3132 cm<sup>-1</sup> represent CH<sub>2</sub> vibration, CH<sub>3</sub> bending, asymmetric bending of CH<sub>2</sub>, C=C stretching, C=N stretching, symmetric stretch of C–H and =C–H stretching in imidazole ring, respectively. The FTIR results are in agreement with the literature (Awadallah-F et al., 2019; Huaiyin Chen et al., 2021).

SEM images of Z-3 are shown in Figure 14. The images are indicative of nanosized crystals of ZIF-8 with the uniform size distribution within the range of 50-200 nm. SEM analysis did not show any significant difference in ZIF-8 nanoparticles caused by microwave assisted method. Further analysis was carried out through TEM observations in order to investigate the effect of synthesis method on the particles size, morphology in a more accurate way. TEM images of sample Z-3 are shown in Figure 15. TEM images exhibit polygon ZIF-8 nanoparticles with a wider size distribution.

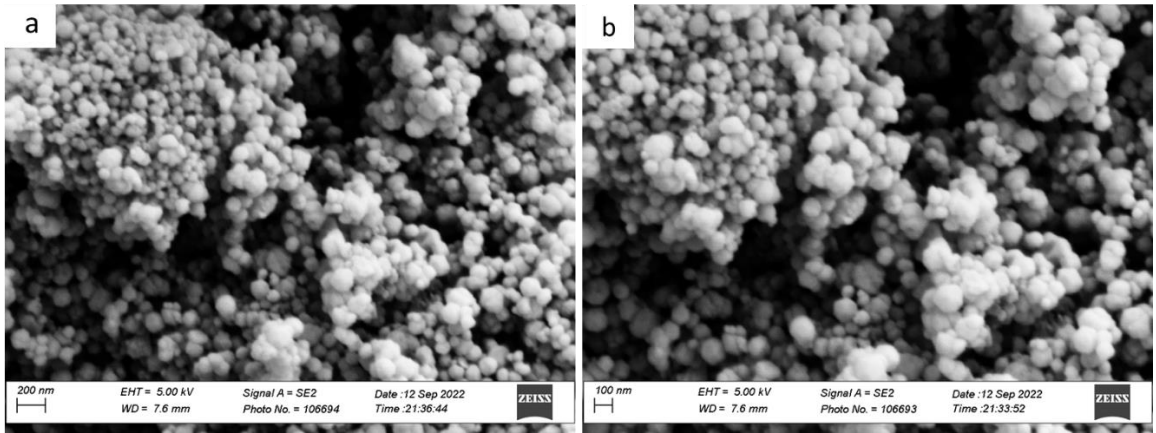


Figure 13. SEM images of the as-synthesized Z-3 in different magnifications.

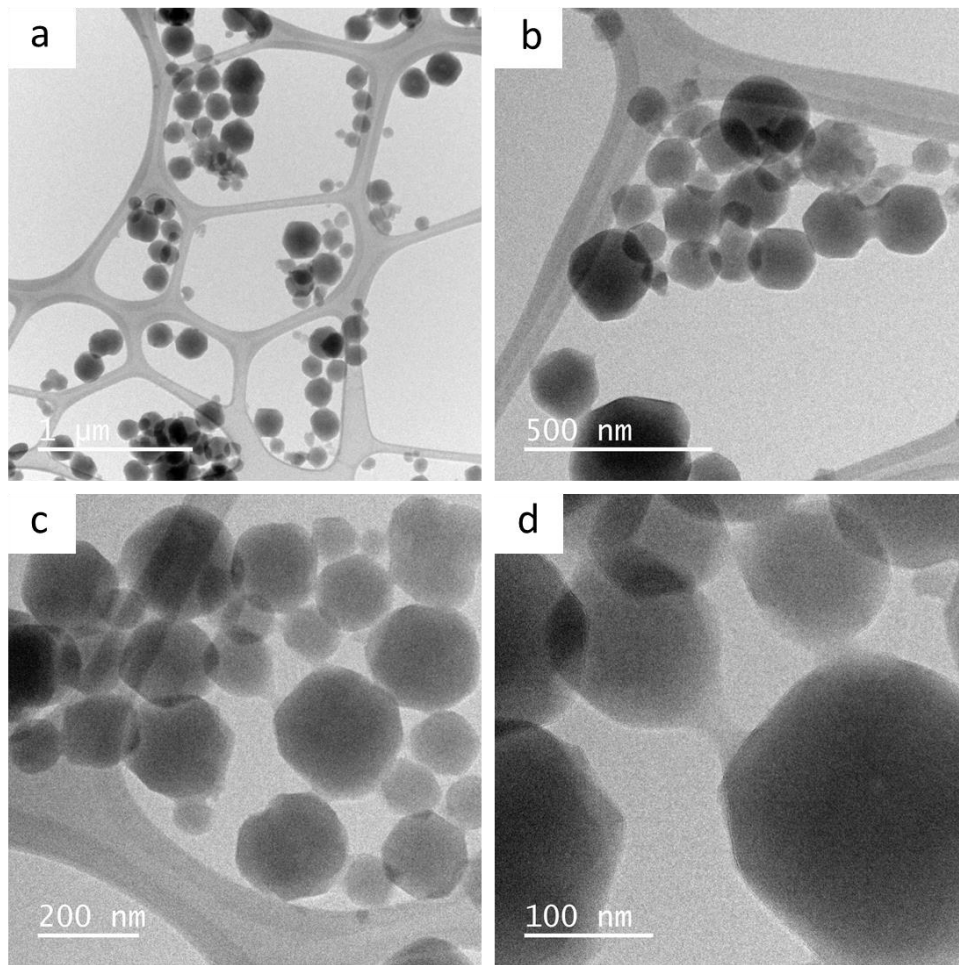


Figure 14. TEM images of the as-synthesized Z-3 in different magnifications.

The N<sub>2</sub> adsorption measurements of sample Z-3 are shown in Figures 16a and b. The N<sub>2</sub> adsorption isotherm in Figure 16a indicates type 1 adsorption behavior. The increase in the adsorbed volume at low pressures is associated with the existence of micropores. The micropore volume and Brunauer-Emmett-Teller (BET) surface area are obtained as 0.5301 cm<sup>3</sup> g<sup>-1</sup> and 1177 m<sup>2</sup> g<sup>-1</sup>, respectively. The results are in good agreement with the reported values in the literature (Y. Pan et al., 2011; Yao et al., 2015). The distribution of micropore size of ZIF-8 nanoparticles was measured using the Horvath-Kawazoe (HK) method. As shown in Figure 16b, three narrow pore size distributions through the pore width range of 0.675- 1.8 nm centered around 0.75 nm, 1.1 nm can be observed.

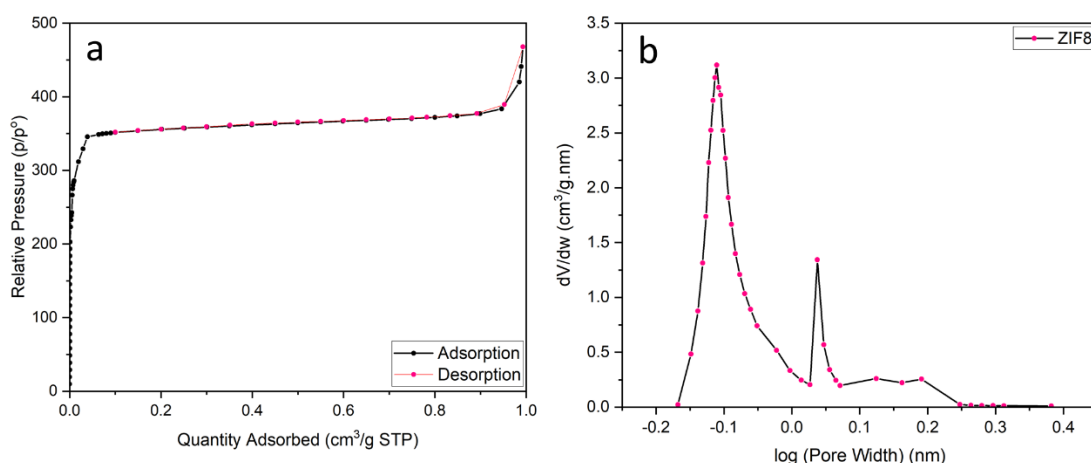


Figure 15. a) Isotherm linear plot and b) Horvath-Kawazoe differential pore volume plot of sample Z-3.

Although the electron microscopy analysis did not show any significant difference between the morphology, ZIF-8 nanoparticles synthesized by microwave assisted method showed a wider size distribution. The N<sub>2</sub> adsorption measurements indicate slight enhancement in porosity of the ZIF-8 nanoparticles. The microwave assisted synthesized nanoparticles show larger pore volume and a more uniform pore size distribution.

On the other hand, the yield percentage of the product in sample Z-3 is obtained as 87.5% which is still a high value and in good agreement with literature (Kida et al., 2013).

ZIF-8 nanoparticles from sample Z-2 were used to develop the ZIF-8 based coating due to faster and easier process in terms of the product mass per each synthesis course. Prior

to spray coating, the samples were functionalized as instructed in the experimental procedure.

### 3.3.2. Superhydrophobic multiscale ZIF-8 based coating

The morphology and surface texture of the superhydrophobic ZIF-8 based coating were characterized by the SEM technique (Figure 16). Observations in low magnifications (Figure 16a) are indicative of the uniform distribution of ZIF-8 nanoparticles. Images at higher magnifications (Figure 16c- d) and in-Lens detector images (Figure 16b) exhibit nanoscale cavities through coatings, which result from the packing of nanoparticles. SEM observations along the surface profile of the coatings confirm a micro/nano surface structure for the coating.

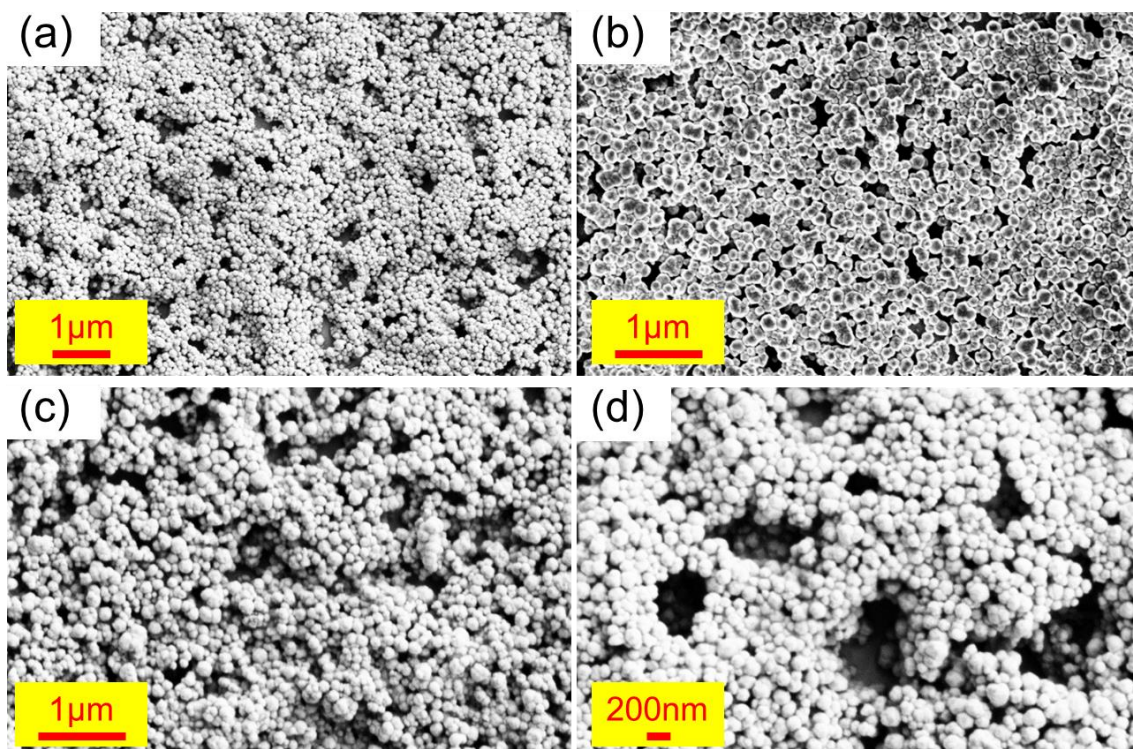


Figure 16. (a-d) SEM images of ZIF-8 based coating in different magnifications.

On the other hand, ZIF-8 comprises micropores located at the center accessible through six-membered apertures (Feng et al., 2021; Y.-R. Lee et al., 2015) due to its sodalite (SOD) topography. Characterization results of the ZIF-8 nanoparticles indicate the porous structure of the nanoparticles. X-ray diffraction pattern confirms the sodalite (SOD) topology of ZIF-8 consisting of micropores. Furthermore, the linear isotherm plot obtained from gas adsorption analysis proves the presence of micropores in ZIF-8 nanoparticles. It should be mentioned that micropore is referred to pores with widths smaller than 2 nm (Sing, 1985). Taking all of these into account, the developed coating based on ZIF-8 nanoparticles has an extraordinary multi scale (subnano-nano-micro) surface topography which is not observed on the other nanoparticle-based coatings such Si<sub>2</sub>O/TiO<sub>2</sub> based coatings. The multiscale surface structure of the coating is created due to 1) superimposed nanoparticles and 2) porous structure of nanoparticles.

Energy Dispersive X Ray (EDX) Analysis results (Figure 17) of the coated samples show a uniform distribution of Fluorine elements on the coatings, which is indicative complete modification of nanoparticles with the silane. ZIF-8 is a porous material with a significantly high surface area. On the other hand, ZIF-8 is an intrinsically hydrophobic material (S. Chen et al., 2019; Sann et al., 2018). Therefore, with a slight chance of the presence of any unmodified pore, hydrophobic behavior will be still observed which enables us to provide a superhydrophobic coating without to an additional material with low surface energy.

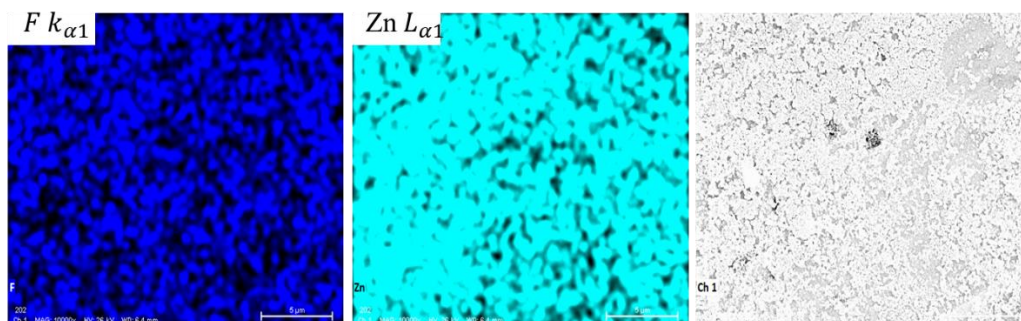


Figure 17. Energy Dispersive X Ray (EDX) analysis results of ZIF-8 based coating.

Contact angle measurements prove significant water-repellent behavior of the developed coating. The water contact angle (WCA) and rolling angle were measured as  $172^\circ$  and  $5^\circ$  respectively. The outstanding superhydrophobic behavior stems from the combination of multiscale surface topography and substantially low surface energy of the surface. Figure 18 displays the water contact angle measurement on a superhydrophobic multiscale ZIF-8 based coating on an aluminum substrate.



Figure 18. Contact angle and contact angle hysteresis measurements of ZIF-8 based coating.

### 3.4 Conclusions

ZIF-8 nanoparticles were synthesized through two different methods. The reactant ratio was kept constant in both methods in order to investigate the process parameters on the final properties of the nanoparticles. Both of the synthesis processes were successful. The  $N_2$  adsorption experiment results of the ZIF-8 nanoparticles synthesis at room temperature indicate the presence of micropores with three narrow pore size distributions through the pore width range of 0.7- 1.8 nm. The micropore volume and Brunauer-Emmett-Teller (BET) surface area were obtained as  $0.4641 \text{ cm}^3 \text{ g}^{-1}$  and  $1173 \text{ m}^2 \text{ g}^{-1}$ , respectively. The results prove a slight enhancement in porosity of the ZIF-8 nanoparticles through the microwave assisted synthesis method as they show a more uniform pores size distribution.

ZIF-8 nanoparticles were functionalized successfully by 1H,1H,2H,2H-perfluorooctyltriethoxysilane (PFOTES). A superhydrophobic multiscale coating was

developed based on ZIF-8 nanoparticles by the spray coating method. Superimposed nanoparticles and porous structure of ZIF-8 along with the water repellency properties of PFOTES led to the significantly high contact angle values of the coating.

## Chapter IV: Static and dynamic icing behavior on a multiscale superhydrophobic zeolitic imidazole framework-based coating

### 4.1. Introduction

This chapter provides a comprehensive study on the responsible mechanisms for reducing the risk of icing in stationary and dynamic conditions. For this, we investigated the anti-icing performance of the superhydrophobic multiscale ZIF-8-based coating (SHMC) developed in the previous chapter which can be a strong candidate for anti-icing applications in energy systems. This chapter investigates the ice formation and growth under static conditions from different aspects. The non-wetting mechanism of the coating is explained with a fractal theory-based model of water contact angle. For static icing tests, the effect of SHMC on ice nucleation, ice growth mode, total surface icing time, and possible condensation induced freezing are investigated. In dynamic icing experiments, the three-phase contact line characteristics including contact times, contact diameters, and interfacial heat transfer during the spreading and retraction stages of the impacting droplet on SHMC are covered.

This study not only indicates the superiority of the SHMC (fabricated in chapter III) compared to the current superhydrophobic surfaces but also highlights the critical parameters for anti-icing surfaces by presenting a fundamental analysis on static and dynamic icing.

## 4.2. Experimental procedure

Icing experiments were performed in a lab-made temperature- and humidity-controlled environmental chamber at various relative humidity (RH) settings. Figure 19 shows a schematic of the experimental setup. Care was taken to preclude possible contamination such as that due to hydrocarbons. The sample was mounted using thermally conductive adhesive tape (McMaster Carr, 6838A11) on the cold plate of a Peltier cooler (Peltier Module TEG High Temperature). The subcooling of the sample surface was maintained by setting the Peltier cooler at different temperatures. A cooling loop was designed to reduce the temperature of the hot plate of the thermoelectric device for thermal stability in long icing experiments. The sample surfaces were monitored and measured simultaneously using an IR thermal camera (FLIR T1020). A standard DSLR camera (Canon EOS) was used to visualize the icing experiments from the top. The real-time experiments were recorded from top and side using IR, high speed, and Digital Single-Lens Reflex (DSLR) camera. Image processing was performed using the MATLAB software.

The droplet impact experiments were performed using deionized water as the working fluid with droplet volumes of  $\sim 0.5$ , 4.2, and 33.5  $\mu\text{l}$  (diameters of 1, 2, and 4mm). Different needles (different gauge sizes) were connected to a syringe pump (LEGATO® 200, KD Scientific, Holliston, MA, USA). Droplets detached due to gravity from needles mounted at heights between 5 and 32 cm, leading to impact velocities ranging from 1 to 2.5 m/s. The impact dynamics of droplets was captured using a speed camera (Phantom v9.1 vision research high-speed camera) operated at different frames per second with long-distance lenses and a workstation with visualization software (Phantom PCC 3.7 software). A cold light source was used to backlight the impacting droplet on the target surface. Depending on the required frame per second (fps), the resolution of the recorded videos ranged from 960 x

240 (7648 fps) to 1632 x 1200 (1000 fps). The experiments were performed on a single droplet impact, where each experiment was repeated for at least five times.

The measuring errors in this study mainly involve the surface temperature and impact conditions measurements. The surface temperatures were measured using a T-type thermocouple ( $\pm 1^\circ\text{C}$ ) and IR Thermal Camera FLIR T1020 ( $\pm 2^\circ\text{C}$ , with 1024x768 resolution). Uncertainty in the ImageJ image software analysis was 1 pixel ( $\pm 0.01\text{mm}$ ). The impact velocity was calculated by examining the last 20 consecutive frames with a maximum uncertainty of  $\pm 0.03\text{ m/s}$ . The maximum uncertainty in the impact Weber number was 7.58%, which was calculated using the following equation (Gultekin, Erkan, Ozdemir, Colak, & Suzuki, 2021):

$$\frac{\delta_{We}}{We} = \sqrt{\left(\frac{\delta_{D_0}}{D_0}\right)^2 + \left(2\frac{\delta_{u_0}}{u_0}\right)^2} \quad (1)$$

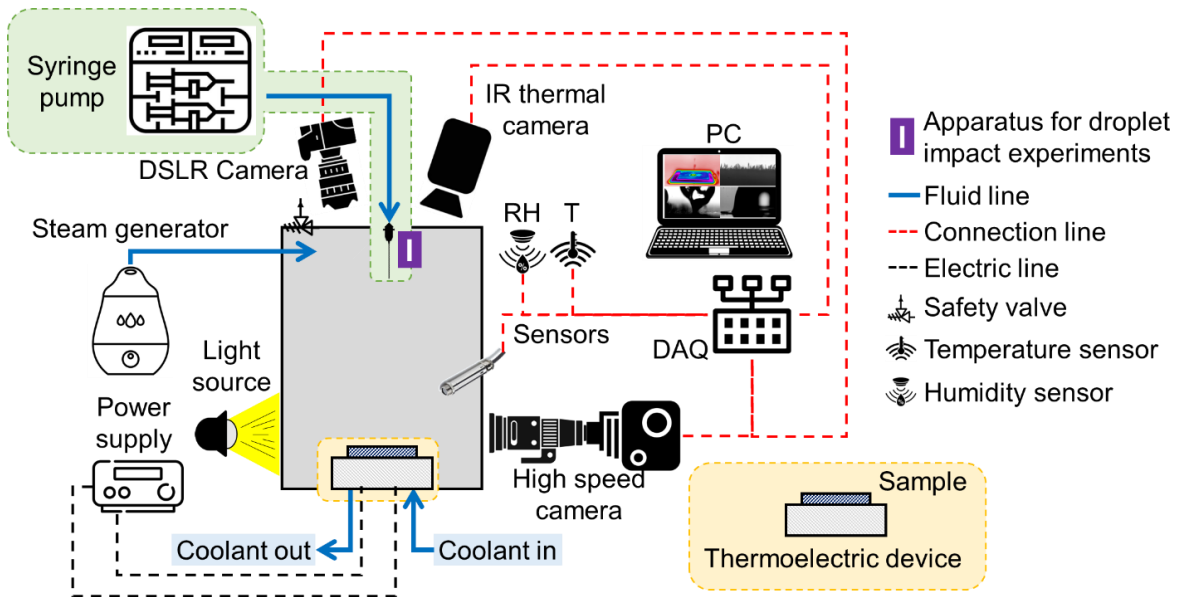


Figure 19. Schematic of the experimental setup for static and dynamic icing. The green region shows the equipment required for dynamic icing tests and orange region shows the surface cooling apparatus

## 4.3. Results and discussions

### 4.3.1. Non-wetting mechanisms

The superhydrophobic surfaces can be realized by using a combination of low surface energy material and surface texture. Due to the successful design and fabrication of SHMC, the proposed coating can satisfy both surface energy and surface structure factors as follows:

Surface chemistry: Generally, materials with nonpolar chemistries and closely packed stable atomic structures have low surface energy and exhibit water repellency. Polysiloxanes ( $-\text{Si}-\text{O}-\text{Si}-$  groups), fluorocarbons ( $\text{CF}_2/\text{CF}_3$ ), nonpolar materials (with bulky  $\text{CH}_2/\text{CH}_3$  groups), or polymers with combined chemistry are some examples of low surface energy materials. The methyl functionalized Im linkers as well as the coordinative saturation of the metal sites in ZIF-8 have a significant contribution to its hydrophobic nature. On the other hand, silane modification of nanoparticles with 1H,1H,2H,2H-perfluorooctyltriethoxysilane (PFOTES) results in superhydrophobic behavior of the coating. The partially perfluorinated silane having three hydrolyzable functional ethoxy groups bonds to ZIF-8 nanoparticles and leads to a structure morphology with strongly bonded perfluoroalkyl functionalities. Low energy perfluorinated alkyl chains on a surface with a hierarchical texture generate a very high water repellency. Water molecules cannot form a hydrogen bond with the superhydrophobic ZIF-8 based coating and form hydrogen bonds with themselves in order to decrease the energy of the system. Therefore, the water molecules have very low interaction with the coating and cannot wet the surfaces.

Surface structure: In terms of the surface structure, the classical Cassie-Baxter (CB) theory assumes that the coating structure consists of two different materials: MOF particles with WCA of  $\theta_s$  and a surface fraction area of  $\varphi_s$ , and air pockets with WCA of  $\theta_v$  and a surface fraction area of  $1-\varphi_s$  (Roach, Shirtcliffe, & Newton, 2008). The apparent CB WCA ( $\theta_{CB}$ ) on the composite interface is then expressed as:

$$\cos \theta_{CB} = \varphi_s \cos \theta_s + (1 - \varphi_s) \cos \theta_v = \varphi_s \cos \theta_s + (\varphi_s - 1) \quad (2)$$

As can be seen in Figure 20a, there is a difference between CB WCA values and those obtained experimentally. The difference is due to the CB model being proposed assuming the morphology of single-scale roughness over the surface. Considering the multiscale nature of the proposed coating, the water contact angle (WCA) of the coated surface can be modeled using the Fractal theory (Parvate et al., 2020; Roach et al., 2008). The Fractal theory was introduced to evaluate complex geometries, in which a fractal geometry can show excellent superhydrophobicity by mimicking nature (Onda et al., 1996). The fractal structure becomes more complex with the number of series and micro- and nanostructures over a lotus surface (Bharat Bhushan, Yong Chae Jung, & Kerstin Koch, 2009). Therefore, Equation (2) can be used after introducing a roughness factor  $(L/l)^{D-2}$ :

$$\cos \theta_{Fr} = \varphi_s \left( \frac{L}{l} \right)^{D-2} \cos \theta_s - \varphi_v \quad (3)$$

Here, D is the Hausdorff dimension, and L and l are the upper and lower limit scales of the fractal structure surface, respectively. Figure 20b shows the Atomic Force Microscopy (AFM) results taken from the sample surface area of  $1 \times 1 \mu\text{m}^2$  (top) and  $20 \times 20 \mu\text{m}^2$  (bottom).

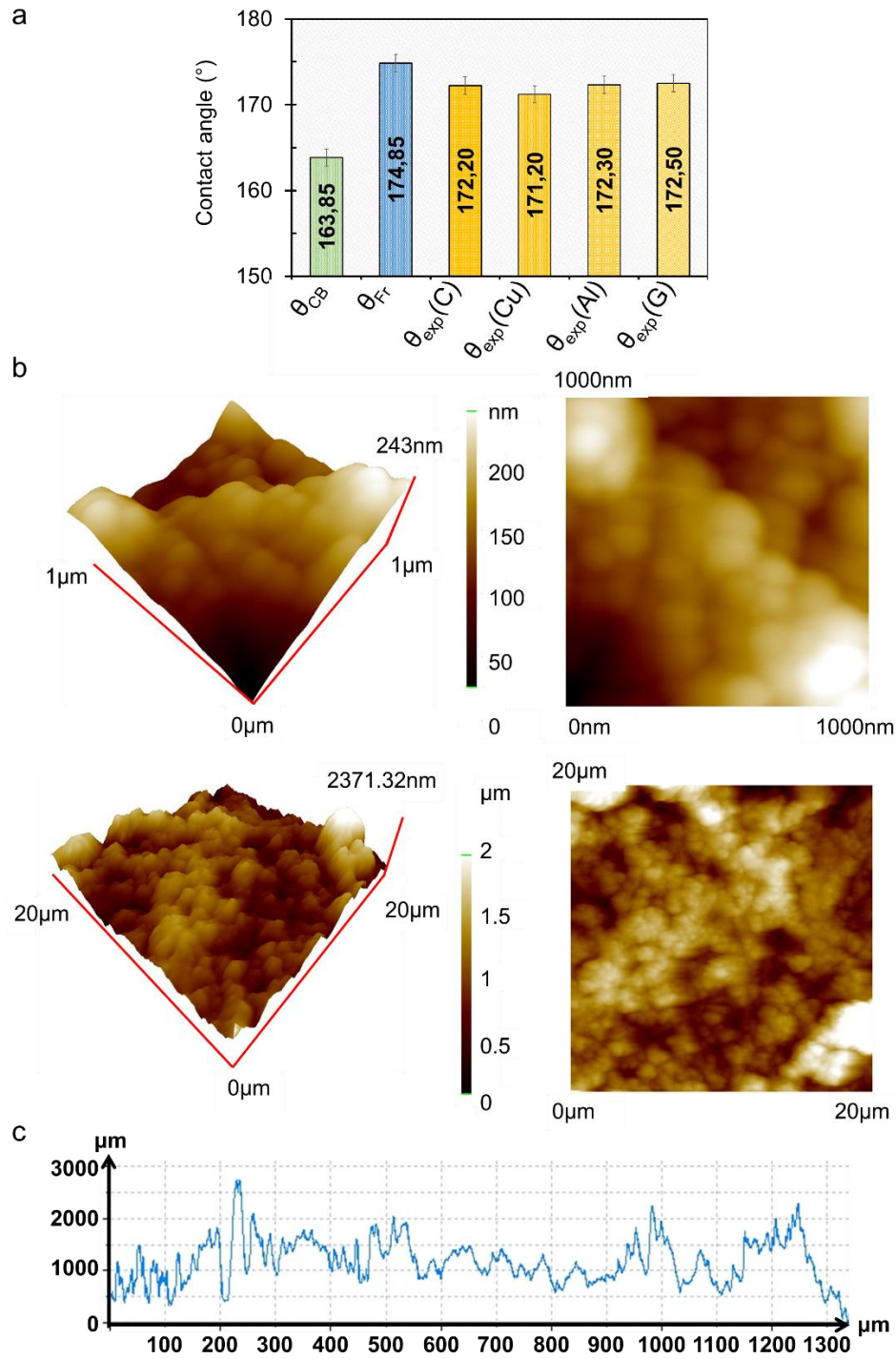


Figure 20. a) Comparison between the predicted static WCAs by the classical Cassie-Baxter and fractal methods and experimental results on different samples, b) AFM results of the surface area of  $1 \times 1 \mu\text{m}^2$  (top) and  $20 \times 20 \mu\text{m}^2$  (bottom), c) surface profile of the SHMC on a copper substrate.

Multiscale randomness and self-similarity features of the surface texture imply that the coating has fractal nature, and fractal theory can be utilized to analyze the wetting mechanism (Jiang, Hu, & Chen, 2020). Based on the fractal analysis,  $\theta_f$  of the nanostructure in the fractal wetting model can be directly calculated by extracting the morphology of the multiscale coating. The fractal dimension “D” can well reflect the roughness, irregularity, and self-affinity of the surface. In this analysis, FracLac (an open-source plugin run in ImageJ) was used, which uses a “box counting” method to find the fractal dimension (D) on the pixel distribution of an SEM image of samples. In this method, a square lattice with lattice constant  $x$  is superimposed on the surface SEM image. Initially,  $x$  is set at  $\alpha/2$  (where  $\alpha$  is the length of the edge of the surface image), resulting in a lattice of  $2^2=4$  boxes. Then,  $N(x)$  is the number of all squares that contain at least one pixel of the image. The lattice constant  $x$  is then reduced stepwise by a factor of 2, and the process is repeated until  $x$  is equal to the distance between two adjacent pixels. The slope of the  $\log N(x)$ - $\log x$  plot gives the fractal dimension  $D$  directly. Figure 21 shows the Fractal analysis obtained from the box counting method with (a) SEM image of the ZIF-8 coating (inset: a reduced size generated from the fractal analysis), (b) plot of the  $N(x)$  and  $x$ , which shows the fractal dimension of 1.83 as the slope of the plot.

The irregularity of the micro-nano-structure of the coating results in different drop/coating interfaces. Therefore, the solid and vapor surface fraction area ( $\phi_s$  and  $\phi_v$ ) of the entire surface cannot be directly calculated. In this study, we used the suggested method in the literature (Jiang et al., 2020). Accordingly, the coating surface is divided into several 2D cross sections. Figure 21a shows a 2D cross-section. The size of the sitting droplet on the coating is larger than the length of the section. Here, we can assume that the maximum air volume below the droplet is the whole volume below the  $S_{\max}$ . Considering the occupied volume by coating ( $S_1$ ), the  $\phi_s$  can be estimated as  $\phi_s = \frac{S_1}{S_{\max}}$  and  $\phi_v = \frac{S_{\max} - S_1}{S_{\max}} = 1 - \phi_s$ .

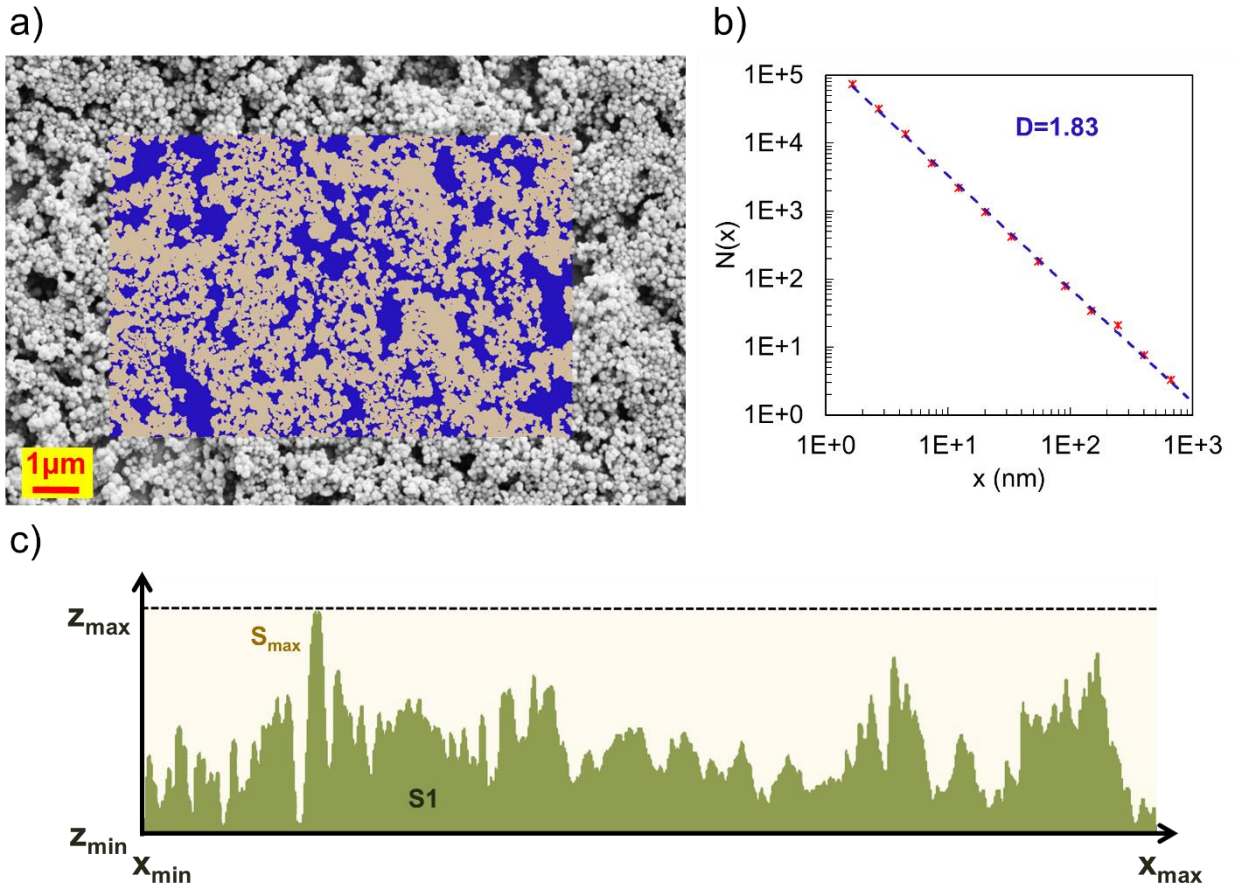


Figure 21. a) SEM image of the SHMC (inset: a reduced size generated from the fractal analysis), b) double-logarithmic plot of the  $N(x)$  and  $x$ , which displays the fractal dimension of 1.83 as the slope of the plot, c) the volume below  $S_{\max}$  in order to calculate  $\phi_s$

The calculated CB ( $\theta_{CB}$ ), fractal ( $\theta_{Fr}$ ), intrinsic ( $\theta_s$ ), and experimental ( $\theta_{exp}$ ) contact angles are shown in Figure 20a. As seen, a good agreement between the obtained results and experimental ones is achieved.

#### 4.3.2 Thermodynamic of the phase change and static icing

Freezing experiments were performed on SHMC and plain surfaces to investigate the effect of surface energy and surface texture. According to the icing behavior observations,

ice formation and accumulation on SHMC samples require a larger supercooling, and ice formation starts at a much lower supercooling temperature on plain surfaces. Equations 3 and 4 express the critical Gibbs Free Energy (nucleation barrier) for homogeneous and heterogeneous nucleation (Zhisen Zhang & Liu, 2018):

$$\Delta G_{Hom}^* = \frac{16\pi\sigma^3}{3\Delta G_v^2} \quad (3)$$

$$\Delta G_{Het}^* = f(\theta, R) \Delta G_{Hom}^* \quad (4)$$

Here,  $f(\theta, R)$  is the shape function that indicates the deviation of the heterogeneous nucleation process from the homogeneous nucleation process. Figure 22 shows the variation in shape function with apparent contact angle and fractal dimensions for hydrophilic and hydrophobic fractal surfaces (Zeng & Xu, 2015). As seen, the shape function increases with the wettability of the fractal surface. According to the Classical Nucleation Theory, ice nuclei need to overcome a larger energy barrier (Critical Gibbs Free Energy) to become stable, grow and continue to decrease the energy of the system on the coated surface compared to a plain sample. The plain samples have a higher surface energy and act as a preferable surface for ice nucleation and facilitate freezing.

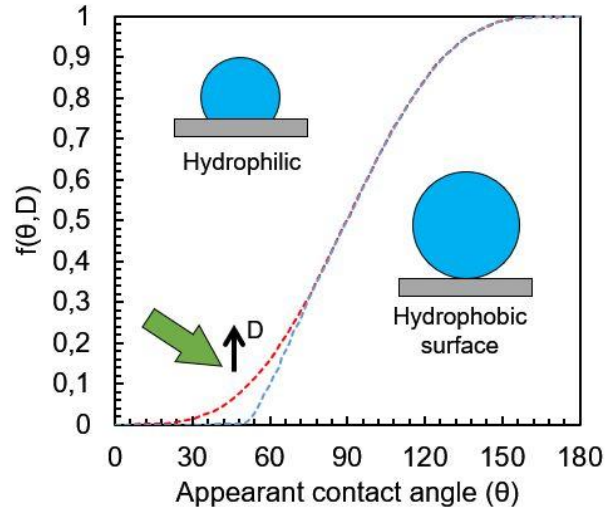


Figure 22. Plot of shape function for different hydrophilic and hydrophobic fractal surfaces (redrawn from [94]).

The total surface icing times on the SHMC and bare surfaces under different conditions are shown in Figure 23. The results show that SHMC considerably prolongs the icing time under different surface and ambient conditions. This implies that the critical radius of stable nuclei may be larger on the coating compared to plain surfaces in heterogeneous nucleation, which means that the embryos need to be larger to be stabilized (more molecules aggregate), which requires more time. On the other hand, the rate of ice nucleation can be calculated as:

$$J = KA_{\text{int}}(\theta, t) \exp\left(-\frac{\Delta G_c(\theta, R)}{kT}\right) \quad (5)$$

where  $K$ ,  $k$ ,  $A_{\text{int}}$  are the kinetic constant, Boltzmann's constant, and the geometric substrate-liquid "apparent" contact area, respectively. From Equation 5, it is apparent that SHMC increases the critical Gibbs Free Energy of heterogeneous nucleation and decreases the nucleation rate.

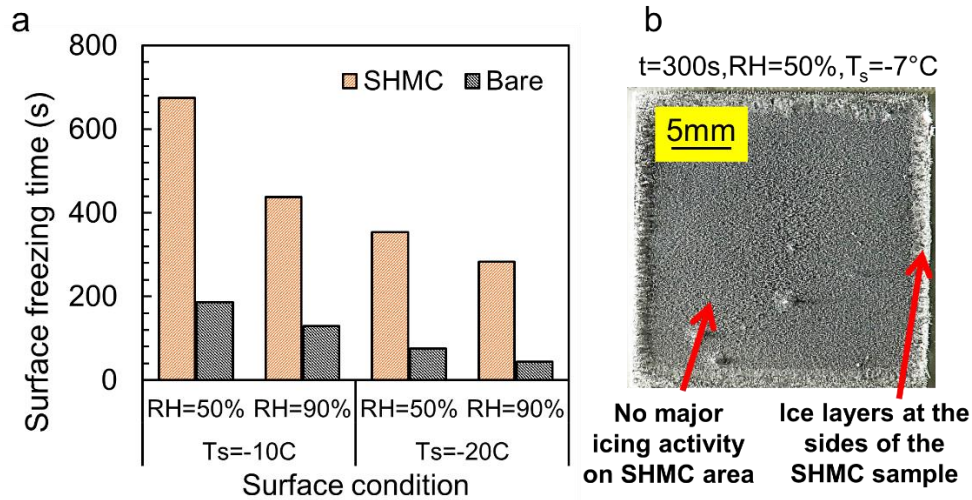


Figure 23. a) Surface freezing time on SHMC and bare samples on different surfaces and under ambient conditions, b) Icing activity on SHMC and plain area (the coating at the edges of the sample was cleaned to show the anti-icing effectiveness of the coated area)

The freezing delay is not only related to the higher ice nuclear barrier but high WCA, low CAH, and lower solid-liquid contact area of the condensate droplets also contribute to icing hindrance on the coated surfaces. Dropwise condensation due to high static WCA and

enhanced mobility because of low CAH on SHMC remarkably reduce the risk of condensation freezing. The low solid-liquid contact area limits the heat transfer from the coating to droplets and extends the icing time. Coalescence-induced droplet jumping is the other parameter contributing to the prevention of icing (Figure 24) (X. Chen, Patel, Weibel, & Garimella, 2016). The jumping of a droplet is a process where condensed water jumps from a surface as the excess surface energy is converted into upward kinetic energy when condensed water droplets merge.

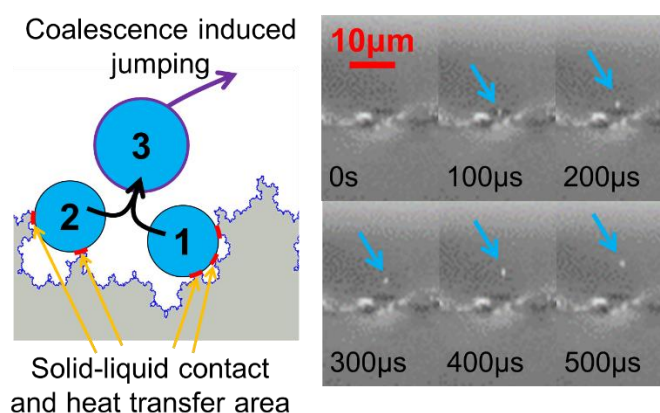


Figure 24. Schematic and microscopic images of coalescence induced droplet jumping on SHMC.

Ice growth is thermodynamically driven by the minimization of the Gibbs surface energy, which is  $\Delta G = \Delta H - T\Delta S$ . The ice growth mode on the SuperHydrophobic Multiscale Coating is majorly different from that of the plain surface. Figure 25a shows the ice growth mode on the bare surface. The ice growth is along the surface, and ice continues to grow in the same focal plane as the substrate. As time passes, ice layers grow and form a thick ice layer. The superhydrophobic nature of the coating imposes a large positive value of  $T\Delta S$ , which overcomes a small positive value of  $\Delta H$ . The entropic contribution to the Gibbs energy,  $T\Delta S$ , dominates over the enthalpic contribution,  $\Delta H$ , making it more energetically feasible for the ice crystal to grow off the surface rather than along the surface. As a result, ice growth on SHMC undergoes an off-surface growth mode, as demonstrated in Figure 25b (Liu et al., 2017). Since the contact area of the ice and SHMC is much lower than the bare surface, the ice layer thickness is also lighter compared to the plain samples.

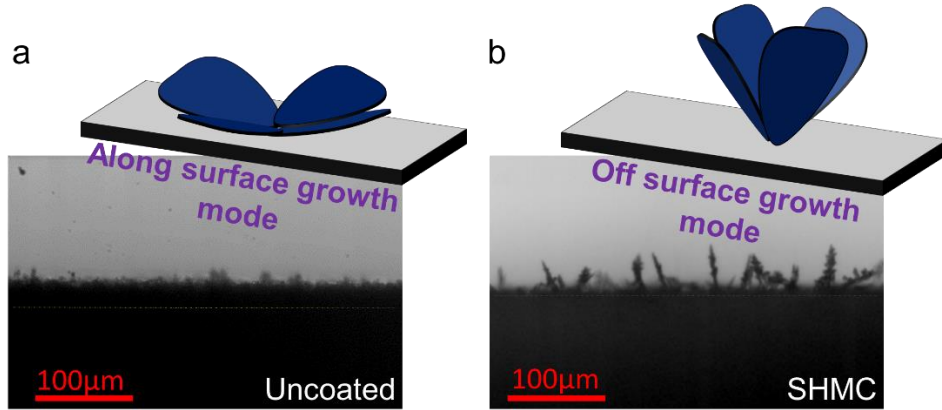


Figure 25. a) icing and icing mode on the bare aluminum surface, b) icing and icing mode on the coated aluminum surface.

With all these into account, it was expected to observe a slower ice growth front on a SHMC sample compared to a bare surface. Ice propagation on coated and uncoated samples at the RH of 90% and  $T_s = -20\text{ }^\circ\text{C}$  was observed (Figure 26). On the bare substrate, ice formation and propagation initiated from the edges and proceeded to the central region of the sample and cover the entire surface in less than 800ms. However, a significant delay in ice accretation was observed on SHMC. Ice formation was observed at different spots due to the surface defects. Ice propagated nonuniformly at different regions. Given 4000 ms, still the entire surface was not covered by ice.

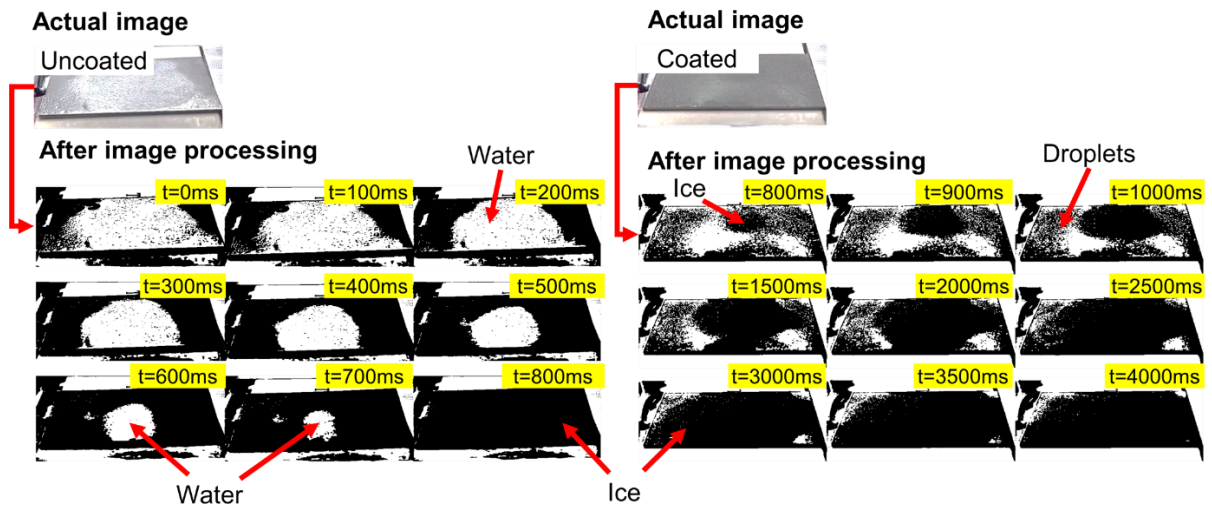


Figure 26. Ice layer growth on a coated and coated sample.

The trapped air within SHMC cavities induces a capillary force on the droplet. The stability of these air pockets is critical for the durability of the superhydrophobic coating and for preventing CB to Wenzel transition during condensation as well as repeating icing/deicing cycles. The droplet can penetrate into i) the passages formed due to superimposed MOF nanoparticles and ii) the nanoparticle pores. As shown in Figure 27, liquid penetration depends on the droplet size ( $R_d$ ), passage or pore size ( $d$ ), and droplet and meniscus angles ( $\theta_d$  and  $\theta_m$ ). The net force acting on a droplet on a hydrophobic pore or passage is given as (Choi & Liang, 2016):

$$F_{net} = \frac{\pi\sigma d^2}{2R_d} + \rho g R_d (1 - \cos\theta_d) \frac{\pi d^2}{4} + \pi\sigma d \cos(\theta_m) \quad (6)$$

Here,  $\sigma$  and  $\rho$  are the surface tension (0.075N/m) and density of water (998 kg/m<sup>3</sup>) at zero degrees, and  $g$  is the gravitational acceleration (9.81 m/s<sup>2</sup>). The first, second, and third terms on the right-hand side equation are the Laplace force acting on a drop, gravitational force, and capillary force by a meniscus in a passage, respectively. When a surface is hydrophobic ( $\theta_d, \theta_m > 90^\circ$ ), the meniscus exerts a force in the upward direction, preventing water penetration. However, when a drop is small enough to make Laplace pressure larger than the capillary pressure, drop penetration can take place due to the positive net force in the downward direction.

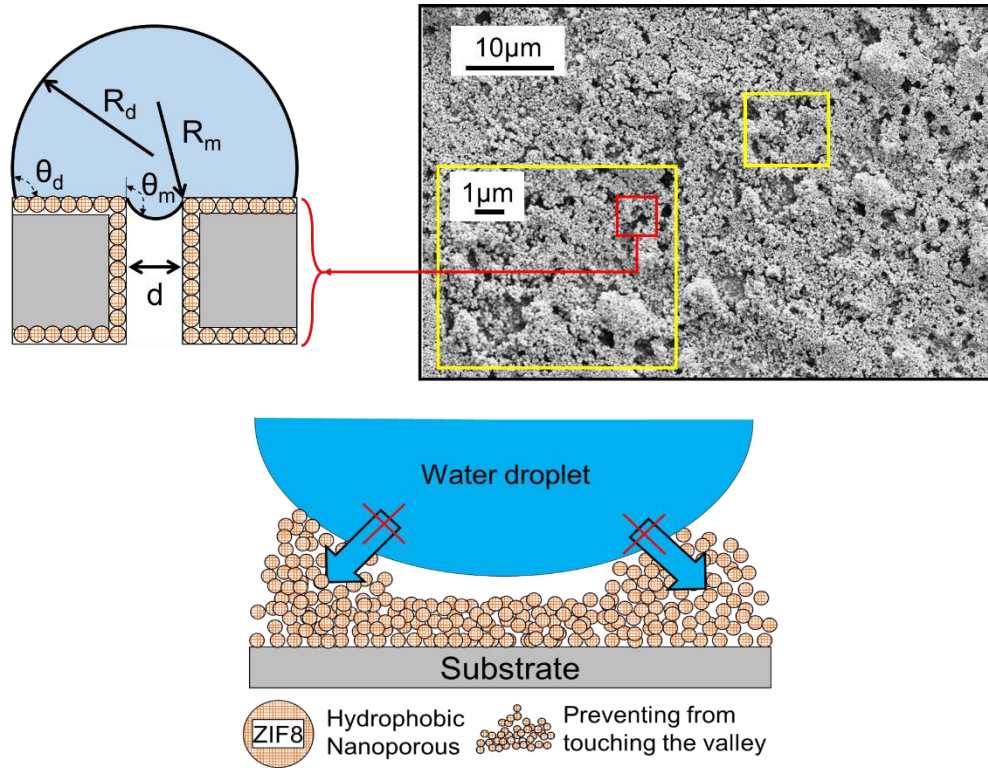


Figure 27. Schematic and SEM image of the passages formed by MOF nanoparticle superposition and the mechanisms responsible for coating stability against droplets

Figure 29 shows the calculated net forces for different droplet and passage/pore sizes. The green area shows the region corresponding to the calculated maximum passage size formed by MOF nanoparticle superimposition. Passages with sizes smaller than  $1\mu\text{m}$  provide a stable condition by preventing the penetration of droplets with radii larger than  $100\text{nm}$ . The liquid penetration within the MOF nanoparticle pores ( $d < 10\text{nm}$ ) also requires droplet radii smaller than  $10\text{nm}$ . The microstructures prevent the droplet from touching the valleys, while hydrophobic nanoparticles pin liquid droplets and thus prevent liquid from filling the valleys between asperities (Figure 27). The dense microscale structure, hydrophobic nature, high surface area, and nanoporous structure of ZIF-8 nanoparticles provide air pocket stability for a higher number of icing/deicing cycles.

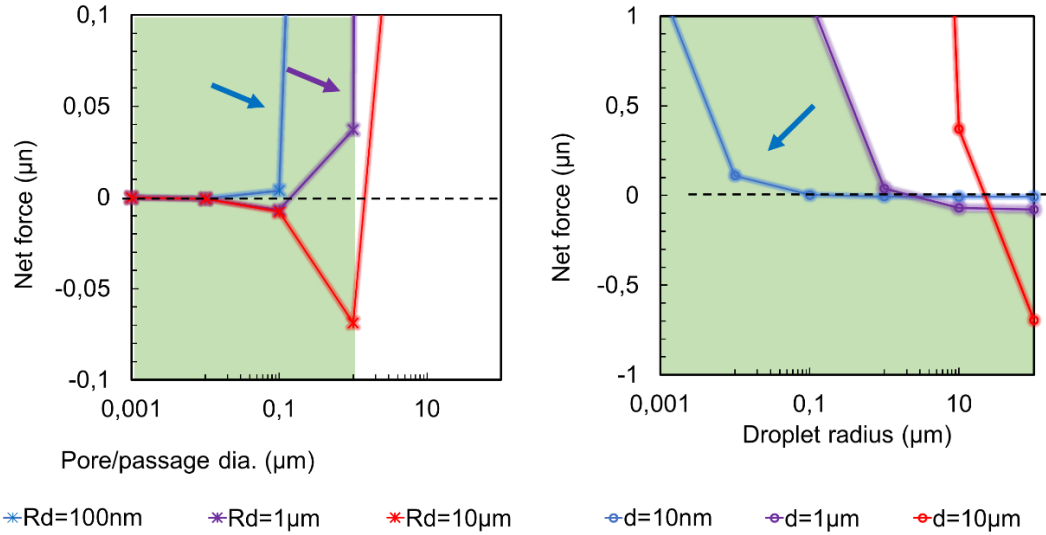


Figure 28. Net forces acting on droplets at different pore/passagage and droplet sizes (Here, the green region indicates the area corresponding to the calculated maximum passage sizes on SHMC surfaces).

As can be seen in Figure 29, the static WCA decreases with the number of cycles. Although a 3% decrease in WCA is observed on tested specimens at  $T_s = -5^\circ\text{C}$ , a further decrease in the surface temperature results in hindering the superhydrophobicity of the coating (6% decrease in WCA at  $T_s = -15^\circ\text{C}$ ).

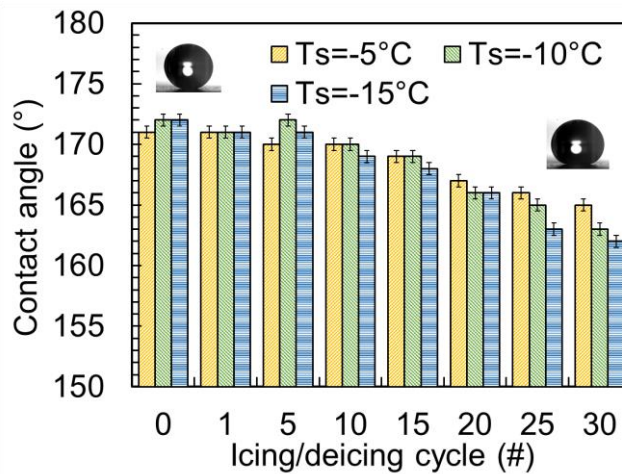


Figure 29. Water contact angle variation with icing/deicing cycles at different surface temperatures.

#### 4.3.3 Dynamic water/ice repellency and contact line behavior

An impacting droplet experiences three stages: spreading, retraction, and bouncing. The droplet dynamics during these stages strongly depend on the relative magnitude of inertia, surface tension and viscous forces as well as the surface wetting state. Weber ( $We = \rho V^2 D_0 / \sigma$ ), Reynolds ( $Re = \rho V D_0 / \mu$ ), Capillary ( $Ca = We / Re = \mu V / \sigma$ ), and Ohnesorge ( $Oh = \mu / (\rho \sigma D_0)^{0.5}$ ) numbers are the non-dimensional numbers used to characterize the impact process, where We, Re, Ca, and Oh numbers stand for the relative magnitude of inertia to surface tension forces, the inertia to viscous forces, viscous to interfacial forces, and viscous to inertia and surface tension forces, respectively. The impact experiments were performed at different surface supercooling temperatures from  $-5^\circ\text{C}$  to  $-20^\circ\text{C}$ , impact velocities from 1 to 2.5 m/s, and droplet diameters of 1, 2, and 3mm. The early stages of droplet impact and spreading for a droplet with  $We=80$  on plain and coated surfaces at room temperature are illustrated in Figure 30.

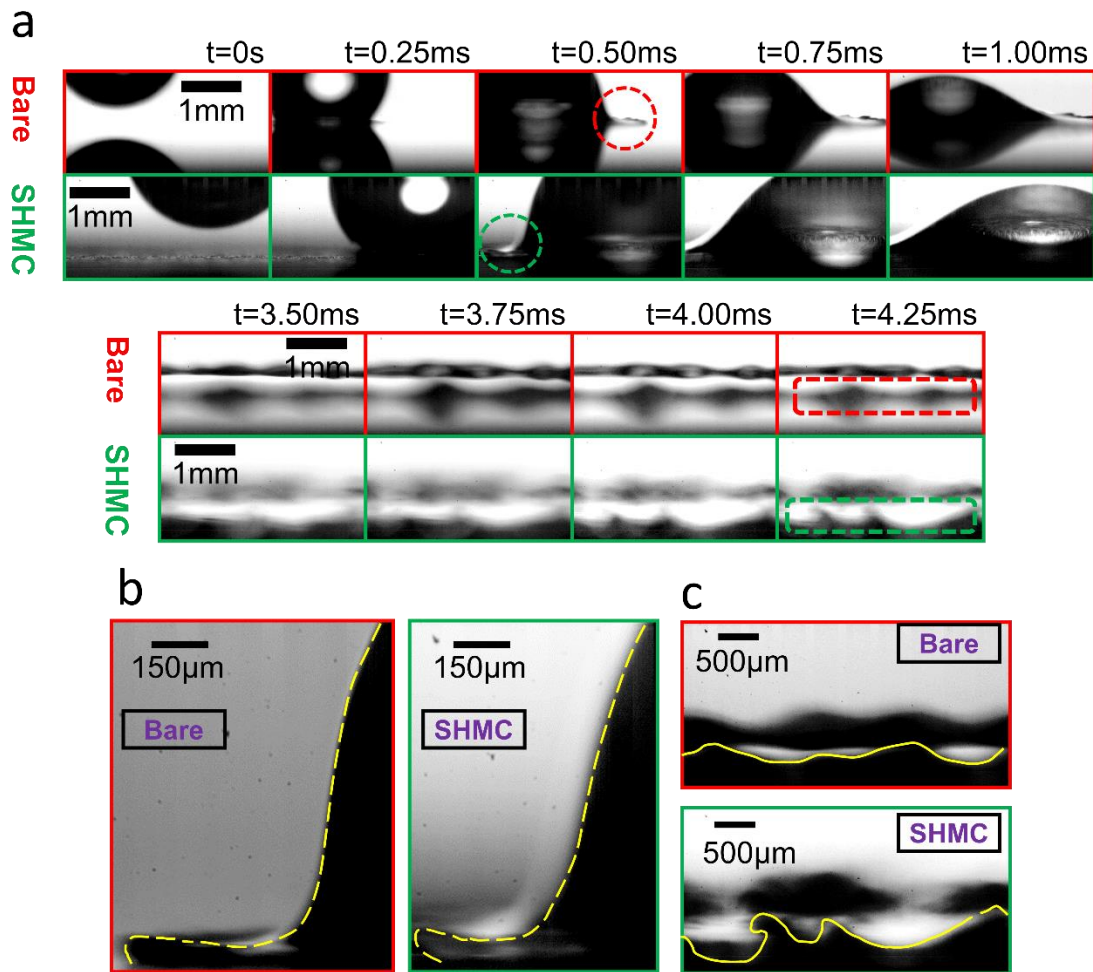


Figure 30. a) High-speed images taken from the early stages of droplet impact on bare (uncoated) and SHMC aluminum surfaces; b) Droplet edge upon spreading on the bare (uncoated) and SHMC aluminum surfaces, c) Fingering of the droplets is evident on coated surface.

The droplet edge upon spreading on the coated surfaces stays untouched by the substrate, resulting in a reduction in the contact area between the liquid and solid phases (Figure 30b). This reduces the viscous dissipation and contact line friction and assists the droplet to maintain its energy and to spread over much larger diameters with larger three-phase contact line velocities. During the later phases of the spreading stage, fingering of the droplets is evident on coated surfaces even at Weber numbers as low as 25. The Rayleigh-Taylor instability at the liquid/air interface is the main reason for the formation of fingers

and break up at the spreading front of the decelerating interface during the later phases of spreading (Figure 30c) (B. Bhushan, Y. C. Jung, & K. Koch, 2009; Sharp, 1984). Stronger interfacial surface tension force on the superhydrophobic (SHPho) surface results in a larger pressure difference across the elongated droplet/air interface. The unbalanced pressure distribution in the droplet also causes the droplet to contract toward its center with larger retraction velocities on the SHPho surface. The retraction velocity has a direct effect on the contact time of a bouncing droplet ( $\tau \sim (\rho D^3 / \sigma)^{1/2}$ ). During the later phases of the retraction stage, where the retraction velocity decreases to zero, the droplet bouncing is observed on coated surfaces (Figure 31).

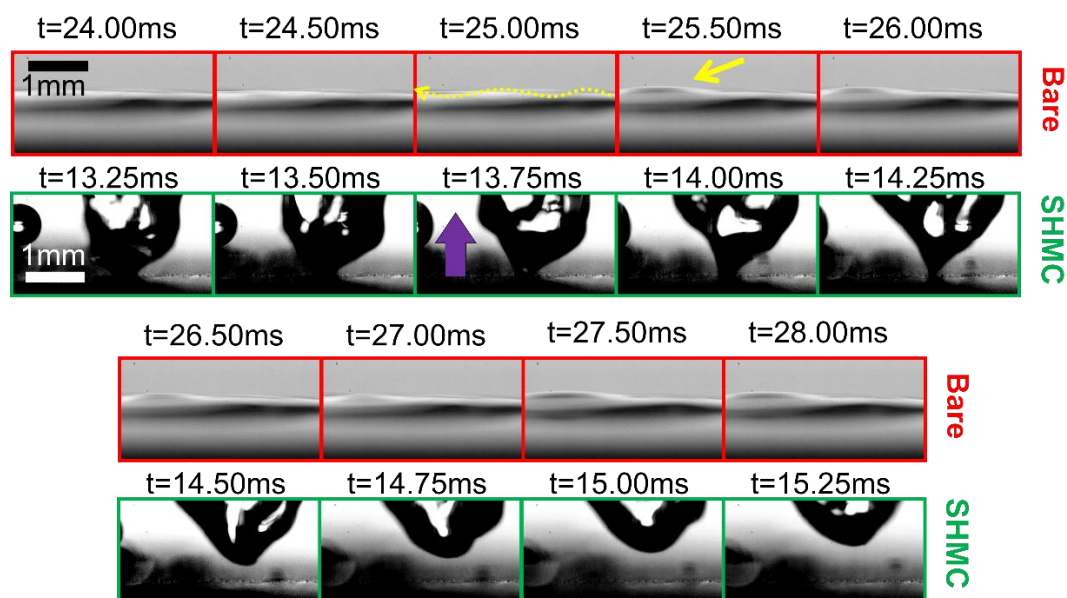


Figure 31. High-speed images taken from the early later stages of droplet spreading on bare (uncoated) and SHMC aluminum surfaces.

The performance of the SHMC surface for anti-icing applications was further examined by investigating the impacting dynamics of droplets with diameters of 1, 2, and 4 mm at substrate temperatures of  $-5^{\circ}\text{C}$ ,  $-10^{\circ}\text{C}$ , and  $-20^{\circ}\text{C}$ . The droplet dynamics upon bouncing from the coated surface is shown in Figure 32 at room temperature ( $20^{\circ}\text{C}$ ) and surface temperatures of  $10$  and  $-10^{\circ}\text{C}$  for  $We=80$ . The effect of a further decrease in surface supercooling on droplet dynamics and resultant heat transfer is negligible, while the surface

supercooling gradually begins to have an effect as the inertia force decreases. Compared to bare surfaces, the proposed coating provides an outstanding performance in terms of droplet mobility and reduction in the heat transfer rate.

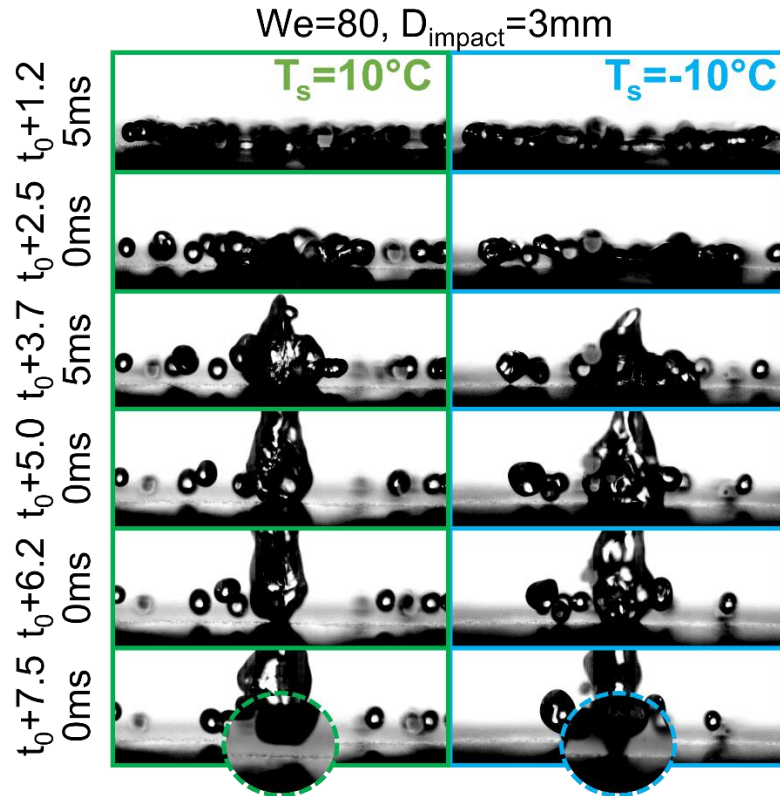


Figure 32. High-speed images taken from the early later stages of droplet spreading on bare (uncoated) and SHMC aluminum surfaces.

The IR thermography images of a droplet impact with We=80 on the bare and SHMC surfaces shown in Figure 33 confirm the heat transfer deterioration during and after impact on the coated sample. Instant droplet deposition and freezing on a supercooled aluminum surface are evident. The non-uniform temperature distribution on the coated surface is the result of droplet splashing, breakup, and bouncing, which decreases the droplet contact time and eliminates the risk of icing on the proposed coating. The gradual decrease in the surface temperature of the coated surface after impact ( $t > 60$ ms) also indicates the liquid stage of the secondary droplets remained on the coated surface.

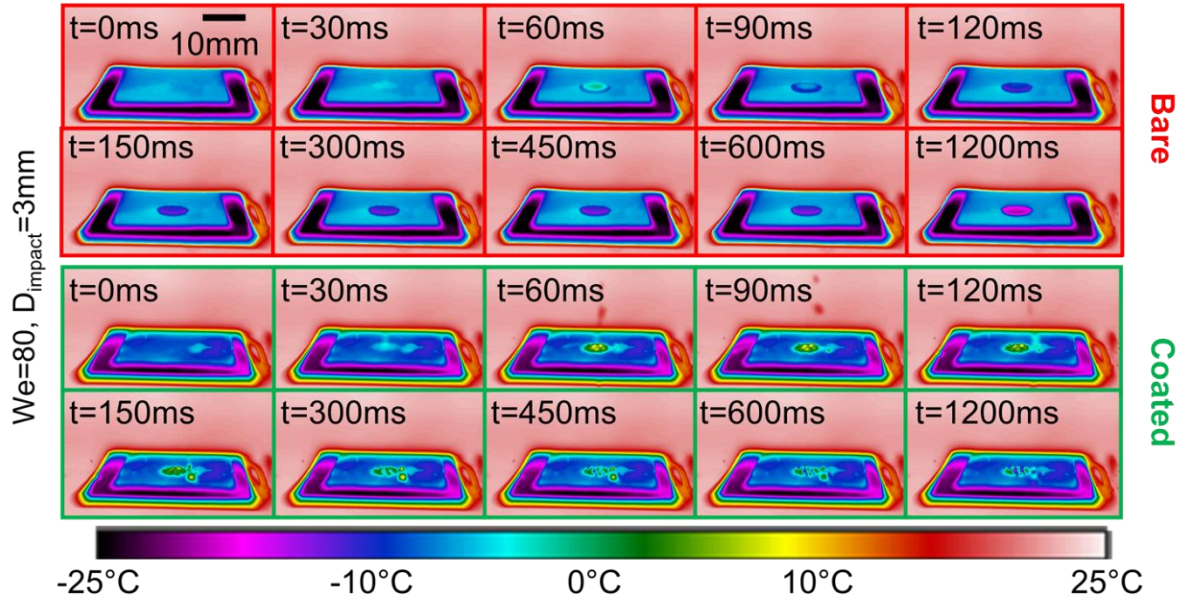


Figure 33. IR thermography images of an impact on bare and coated aluminum surfaces.

#### 4.4. Conclusion

A comprehensive examination of the static and dynamic icing performance of the superhydrophobic multiscale coating (SHMC) was made using microscopic and macroscopic analyses. The microscale peaks of the coating texture were achieved by nanoparticles superposition, MOF nanoparticles formed nanoscale structures, and nanoparticle pores and their effect on nanoparticle morphology led to subnano features of the structure. Multiscale, randomness, and self-similarity features of the SHMC texture suggested the fractal nature of the coating, and a fractal theory-based model of water contact angle was adapted to reveal the non-wetting mechanism on SHMC. Different modes of icing were observed on plain (on-surface) and coated surfaces (off-surface), resulting in different ice morphology due to the presence of the coating on the substrate. The multiscale texture of the SHMC extended the icing time by at least 300% and maintained its superhydrophobicity for more than 30 icing/deicing cycles. The capillary pressure generated within the multiscale coating prevented the droplet from penetrating into the structure and reduced the risk of

condensation-induced freezing under different variant supercooling and relative humidity conditions and within continuous icing/deicing cycles. Compared to the plain sample, which exhibited instant icing at 60ms after impact, no icing was observed on the SuperHydrophobic Multiscale Coating . The three-phase contact line characteristics including the contact times, contact diameters, and interfacial heat transfer during the spreading and retraction stages of the impacting droplet on SHMC were assessed for different surfaces and ambient conditions. The high speed and IR thermography results proved that reduction in heat transfer rate during the total droplet contact time could be obtained on SHMC.

## Chapter V: Biphilic surfaces for icing/de-icing applications and passive cleaning of surfaces

### 5.1. Introduction

Condensation frosting and de-frosting is a process with multi-scale energy transfer and interfacial phenomena, starting from the initial formation of droplets at scale of only a few nanometers, continuing with growth and coalescence, droplet departure/shedding and frost sheets of at a millimetric length scale. Furthermore, de-icing and the behavior of slush/water during and after melting are the events that are highly dependent on interfacial and surface forces. Each of processes and subprocess involves different phase states and has different preferred conditions due to their various governing mechanism. Therefore, a vigorous study on the entire process focused on the interfacial events at different scales is required.

Microscale biphilic surfaces have shown promising behavior in different phase change applications. The effect of superhydrophobicity ratio through microscale biphilic

surfaces have been investigated previously by our group (Chehrghani, Abbasiasl, Sadaghiani, & Koşar, 2021; Motezakker et al., 2019). Biphilic surfaces consisting superhydrophobic islands on a hydrophilic region with different superhydrophobicity ratios were studied for thermal fluid systems and superhydrophobicity up to 38.46% enhance both heat transfer coefficient and critical heat flux up to 103% and  $197 \frac{W}{cm^2}$  among the tested biphilic surfaces (Motezakker et al., 2019). Furthermore, although superhydrophobic surfaces are very practical in terms of condensation heat transfer, Chehraghi et. al (Abbasiasl, Chehrghani, Sadaghiani, & Koşar, 2021) indicated that the presence of hydrophobic regions on superhydrophobic substrates can enhance the heat transfer performance. For instance, biphilic surfaces having islands with the diameter of 500  $\mu m$  indicated condensation heat transfer was enhanced by 36% and the high heat transfer coefficient for steam mass flux (SMF) of 50  $kg/m^2 s$ .

Motivated by the promising behavior of biphilic surfaces and our previous results, in this study, we explored the performance of microscale biphilic surfaces for icing/de-icing conditions. This study investigates the effect of superhydrophobicity ratio and biphilic design on condensation icing from different aspects including the frost structure and frost hampering mechanism. Furthermore, this study reveals the behavior of slush water during de-frosting and the capability of the biphilic designs for passive cleaning with zero external energy.

## 5.2. Experimental procedure

### 5.2.1. Surface fabrication

Surfaces with mixed wettability were fabricated using microfabrication techniques. Samples consist of one hundred superhydrophobic circular islands (silicon nanoglass) surrounded by a hydrophilic area ( $SiO_2$ ). The superhydrophobic spots were distanced from each other with a pitch size of 1 mm in all the samples. Figure 34 shows the configuration of

biphilic samples where  $D$  is the diameter of superhydrophobic island and  $S$  is the edge to edge distance between spots. Samples with different ratios of the superhydrophobic to total areas were fabricated by increasing the diameter of the superhydrophobic spots (table 1). Figure 35 shows the process flow of sample fabrication. Samples were fabricated on 10 mm  $\times$  10 mm diced silicon wafers. The fabrication procedure includes three main processes: 1) reactive ion etching (DRIE), 2) silicon oxide thin film thermal growth, and 3) nanoglass fabrication.

Firstly, the silicon substrate was etched according to the hydrophilic network. photoresist AZ-ECI was used as a mask to protect the areas that were allocated to hydrophobic spots. Through wet thermal oxidation, a layer of  $\text{SiO}_2$  with the thickness of 1  $\mu\text{m}$  was grown on the Si substrate. Consecutively,  $\text{SiO}_2$  hydrophilic network was protected during dry etching by a patterned layer of photoresist. subjecting the sample to etching and removing the photoresist, step 2 consisted on the application of another layer of patterned photoresist with the desired geometric configurations included in Table 1. to protect the  $\text{SiO}_2$  domains and expose the areas at which the superhydrophobic islands were fabricated via deep reactive ion etching and black silicon method (Motezakker et al., 2019). A  $\text{SiO}_2$  coated sample and a superhydrophobic multiscale zeolitic imidazolate framework based coated sample (SHMC) fabricated in the previous chapter were used as totally hydrophilic and totally superhydrophobic reference samples.

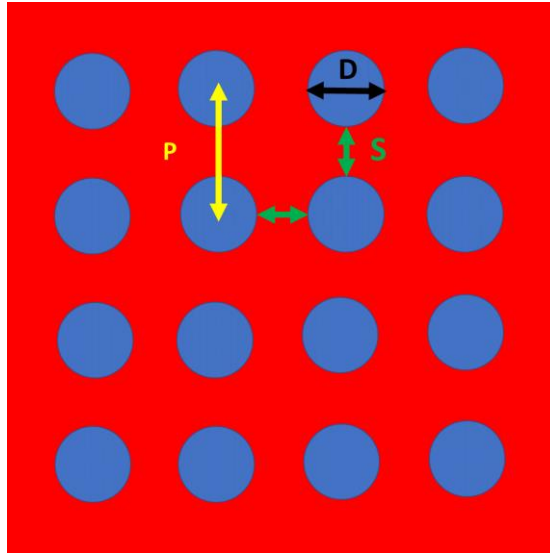


Figure 34. Configuration of biphilic samples consisting of superhydrophobic areas (blue spots), a hydrophilic substrate, as P, D, and S represent the pitch size, diameter, and edge-to-edge spacing with  $P = D + S$ .

Table 1. Geometric properties of the fabricated samples.

Sample code	Diameter ( $\mu\text{m}$ )	Edge to edge spacing ( $\mu\text{m}$ )	Superhydrophobicity ratio	Diameter to edge-to-edge spacing ratio
D1	150	850	1.76%	3:17
D5	500	500	19.62%	1:1
D7	700	300	38.46%	7:3
D10	1000	-	78.50%	-
SiO <sub>2</sub> coated silicon substrate reference surface	-	-	0.00%	-

SHMC (chapter 3) reference surface 2	-	-	100.00%	-
---	---	---	---------	---

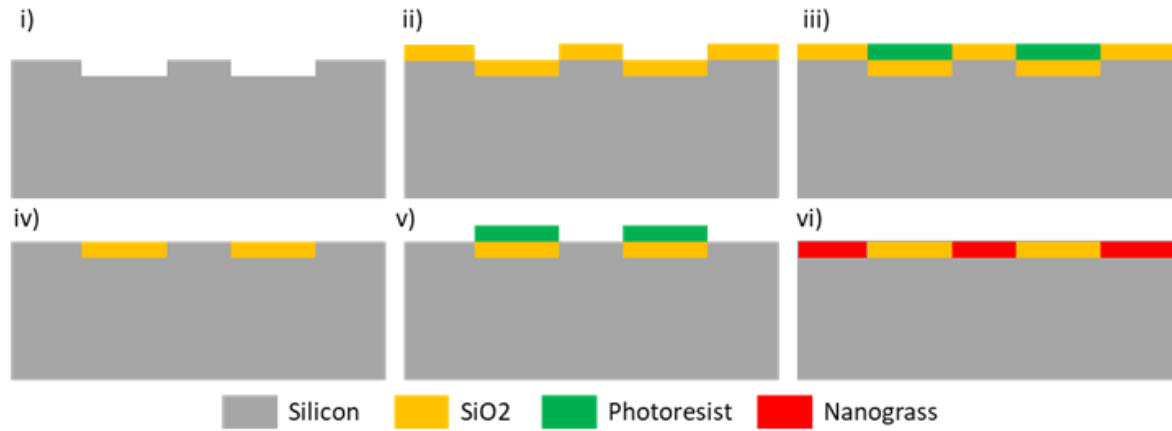


Figure 35. Schematic of the microfabrication process of the sample.

Figure 36 shows the Scanning Electron Microscopy (SEM) image of a fabricated biphilic surface. The nanograss structure developed via DRIE and black silicon methods has water contact angle (WCA) of 165° and the silicon oxide substrate shows a hydrophilic behavior with a WCA of 20°.

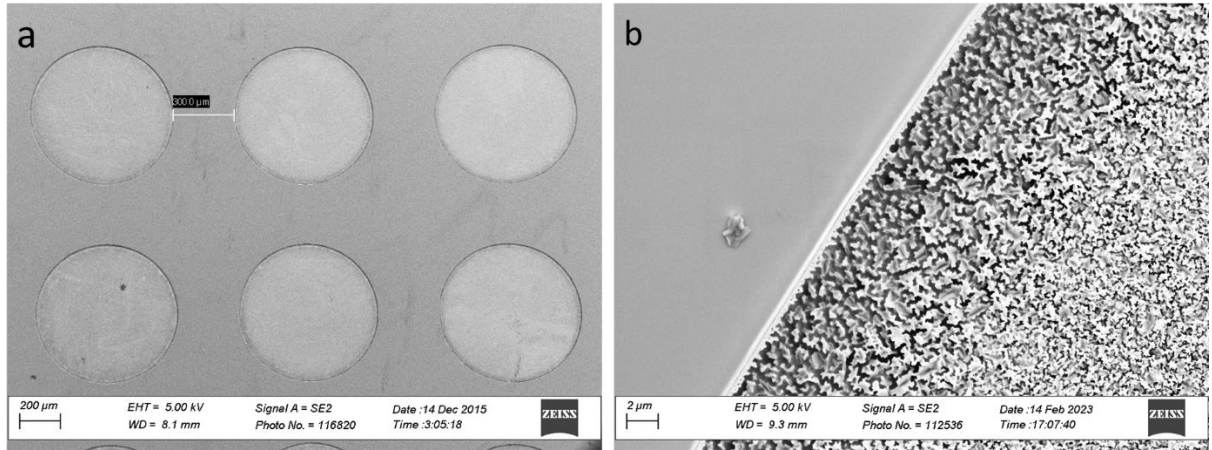


Figure 36. SEM images of a biphilic sample consisting of superhydrophobic islands with  $D=700 \mu\text{m}$ .

### 5.2.2. Icing/de-icing experiments

Interfacial phenomena during vapor to liquid and liquid to solid phase change were observed using a customized temperature- and humidity-controlled experimental setup described in chapter 4, which provides both normal-view and edge-view observations.

Figure 37 shows the photograph of the experimental setup. The samples were placed on the cold plate of Peltier (Peltier Module TEG High Temperature). A thermally conductive adhesive tape (McMaster Carr, 6838A11) was used to provide a good thermal conductivity between the sample and the Peltier cooler. The subcooling of the sample surface was maintained by setting the Peltier cooler at different temperatures. A cooling loop including a chiller and a water circulation system was designed to reduce the temperature of the hot plate of the thermoelectric device for thermal stability in long icing experiments. The chiller was set at the temperature of  $0 \text{ }^\circ\text{C}$ . The sample surface temperatures were monitored and measured simultaneously using an IR thermal camera (FLIR T1020). A standard Digital Single-Lens Reflex (DSLR) camera was used to provide observation and measurements from the side. The real-time experiments were recorded from the top using a Phantom VEO 710 high-speed camera.

Firstly, in order to be able to visualize the effect of wettability on condensation icing and de-icing more clearly, sample D5 was placed at the temperature of  $-15^{\circ}\text{C}$  and relative humidity (RH) of 75%. Later on, the icing/de-icing experiments for all the samples continued at the cold plate temperature of  $-8^{\circ}\text{C}$  and relative humidity of 55%. The cooling cycle was operated until a frost of thickness  $h = 2\text{ mm}$  was formed on the biphilic sample. The frost thickness was monitored actively using edge-view imaging. The measurement method and the choice of 2-mm thickness were chosen according to the sample size, literature and repeatability (Boreyko et al., 2013; Gurumukhi et al., 2020). Measuring frost thickness accurately is difficult owing to the presence of dendrite formation and highly porous frost films on the surface. De-icing was performed at the temperature of  $0^{\circ}\text{C}$  by turning off the de-electric device while the chiller and associated water circulation were still working at  $0^{\circ}\text{C}$ . The frosting time  $T_f$  was measured as the sample reached to  $-8^{\circ}\text{C}$  until 2mm of frost formed. The cleaning time  $T_c$  was measured starting from the second that sample surface temperature reached  $0^{\circ}\text{C}$  until no further water mobility was observed and water became stable on the surface.

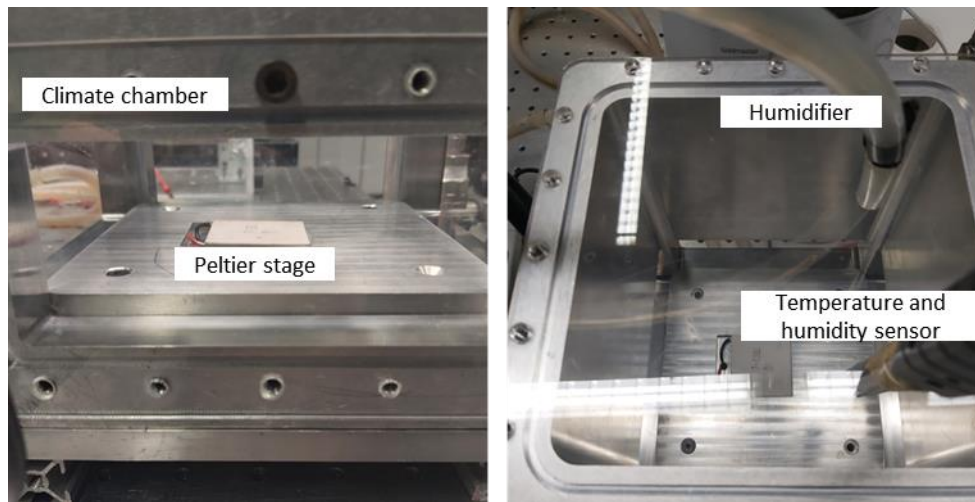


Figure 37. Photographs of the customized experimental icing setup.

### 5.3. Results and discussion

### 5.3.1. Effect of wettability on icing/de-icing

Condensation frosting occurs in main 5 consecutive stages: 1) condensation, 2) droplet coalescence, 3) ice nucleation and frost propagation, 4) dendrite growth, and 5) frost densification. Condensation and icing occur when nucleation energy barrier is overcome. Vapor condensate on a substrate colder than the surrounding atmosphere to form nanoscale droplets. The on-going vapor condensation leads to the growth and coalescence of the as-formed droplets. Given enough time to the supercooled droplet on substrate, heterogeneous ice nucleation occurs at the interface between the droplet and the surface (Yang et al., 2021).

Figure 38 shows the sequential images of condensation, icing and de-icing at the temperature of  $-15^{\circ}\text{C}$  and relative humidity (RH) of 75% on sample D5 in a horizontal configuration (without the presence of any external force acting on the droplets/slush). The  $t=0$  represent the moment the sample is placed on the cold plate. As the sample reached the temperature of  $-15^{\circ}\text{C}$  at  $t=20\text{s}$ , the condensation started at the hydrophilic/superhydrophobic boundaries, specified in the green circles indicating the boundaries as preferable locations for nucleation. This may be due to the distinct surface topography formed at the boundaries of the nanograss structure and smooth silicon oxide surface. As the surface temperature decreases, the formation of water droplets will be first observed on hydrophilic and then superhydrophobic regions. The number of the droplets changes (increases) with a faster rate on the hydrophilic regions. The number of nucleated droplets on the hydrophilic background is noticeably more than in the superhydrophobic islands ( $t=60\text{s}$ ). This suggests that the hydrophilic regions not only facilitate but also accelerate condensation on the biphilic substrate.

As the vapor condenses on a substrate, nucleation, growth and droplet mobility (three stages of dropwise condensation) depend on the heat transfer behavior of the surface which is mainly governed by the surface wettability. The critical radius of stable nuclei for nucleation,  $r^*(r_{\min})$ , can be obtained by the following formula (Maa, 1978; Wen & Ma, 2020b):

$$r^*(r_{\min}) = \frac{2\sigma_{lv}T}{\rho_l h \Delta T} \quad (1)$$

where  $\sigma_{lv}$ ,  $\rho_l$  and  $h$  represent the liquid – vapor interfacial energy, liquid density and the phase transition latent heat, respectively. Furthermore, an energy barrier,  $\Delta G^*$ , is required to be overcome so that stable nuclei ( $r = r^*$ ) form and grow into the droplets. This energy barrier  $\Delta G^*$  depends on the properties of both the liquid and substrate (Varanasi, Hsu, Bhate, Yang, & Deng, 2009):

$$\Delta G^* = \frac{\pi\sigma_{lv}r_{\min}^2(2-3\cos\theta+\cos\theta^3)}{3} \quad (2)$$

where  $\theta$  is defined as the contact angle of the substrate. According to equation (2), hydrophilic surfaces are more susceptible to the nucleation due to their lower energy barrier (affected by their higher wettability). This is the reason for why the condensation is first observed on hydrophilic areas compared to the superhydrophobic islands. On the other hand, the nucleation rate  $J$  is also affected by the surfaces wettability (Varanasi et al., 2009):

$$J = J_0 \exp\left(-\frac{\Delta G^*}{kT}\right) = J_0 \exp\left(-\frac{\pi\sigma_{lv}r_{\min}^2(2-3\cos\theta+\cos\theta^3)}{3kT}\right) \quad (3)$$

where  $J_0$  is defined as a kinetic constant. According to this equation, heterogeneous nucleation on a surface with lower contact angle (lower energy barrier) occurs faster compared to a surface with lower wettability (He et al., 2022). Due to the uniform  $G$  and  $J$  on silicon oxide, heterogeneous nucleation initiates on hydrophilic regions and droplets form randomly without any specific preference. However, a delay and a slower process is observed in condensation of droplets with Cassie Baxter state on nanogras islands. It is noticeable that condensation on superhydrophobic islands enhanced by decreasing the temperature which is due to the fact that  $\Delta G^*$  and  $J$  are directly affected by the subcooling  $\Delta T$ . A larger subcooling  $\Delta T$  can compensate the high nucleation energy barrier on superhydrophobic islands.

Another reason for observing a smaller number of droplets on the islands during condensation is droplet coalescence-induced jumping, a common phenomenon for superhydrophobic surfaces (Boreyko & Collier, 2013). Droplets can be removed from the surface prior to freezing due to the droplet mobility. Due to this phenomenon, only one third of the condensed droplets freeze while two third of them are removed because of evaporation.

Thus, as a result of droplet mobility and low nucleation rate, the superhydrophobic islands are only covered by small number of droplets.

As the surface temperature decreases, the droplets start to freeze ( $t=80s$ ). This can be observed by comparing the light intensity in the frozen droplets and liquid ones (the ice phase is darker compared to the glowing liquid phase). Icing initiated on the hydrophilic regions and the remaining droplets froze as the surface temperature decreased further until the whole surface was covered in iced droplets ( $t=95s$ ). According to the obtained results, droplet icing occurs with a few seconds delay on superhydrophobic spots compared to the hydrophilic background. Wettability has a significant influence on icing as well. Water droplets on hydrophilic regions are able to form a proper contact area with the solid substrate which leads to a better interfacial heat transfer during the phase change. However, due to the presence of air pockets trapped on the surface structure and the resulted interfacial thermal resistance, compensating the activation energy for ice nucleation on superhydrophobic islands is more challenging. It is the reason that water droplets on the hydrophilic regions froze without any further increase in their size while the Cassie Baxter state droplets only grow larger (condensation) in the same condition and froze by a larger subcooling or given more time.

In the last stage, the cooling power was turned off while the chiller was still set at 6 °C, and the de-iced droplets from the passive de-icing are shown in Figure 39 ( $t>95s$ ). Comparing images before and after icing ( $t=60s$  vs.  $t>95s$ ) it can be concluded that the number density of droplets on the superhydrophobic spot remained almost the same, while droplet coalescence and unification occurred in the hydrophilic region, which resulted in a lower number of droplets with larger diameters (yellow squares for the hydrophilic region and red circles for the superhydrophobic spots).

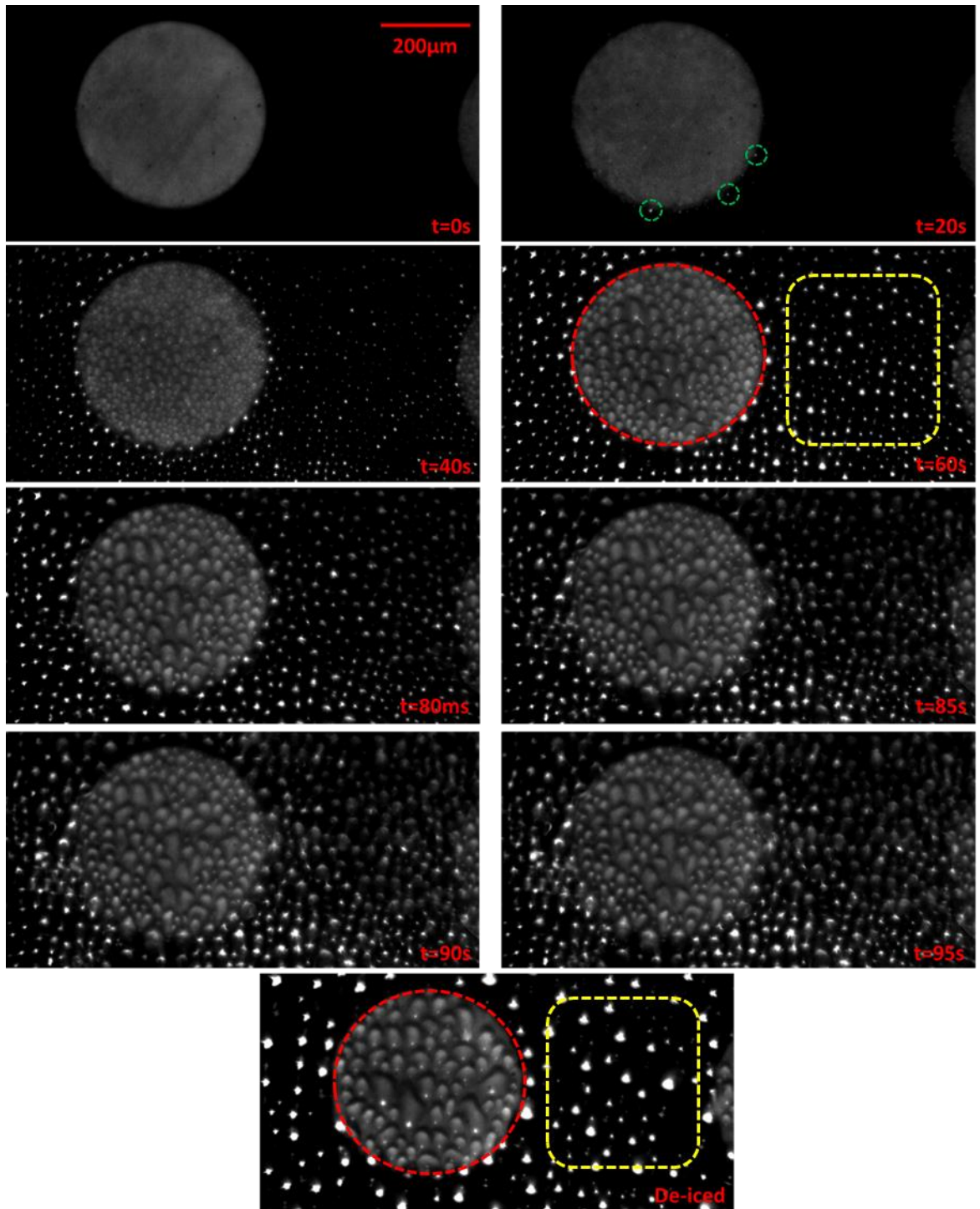


Figure 38. The sequence of images taken from biphilic surface during condensation, icing at the temperature of  $-15^{\circ}\text{C}$  and relative humidity (RH) of 75% and thermal de-icing at  $6^{\circ}\text{C}$  on sample D5.

A schematic of droplet and ice formation is shown in Figure 39a. Due to the lower surface energy of the superhydrophobic spots, the nucleated droplets tend to stay separately and form larger and distant droplets in the later stages of the drop condensation ( $t > 40s$ ). On the other hand, droplets on the hydrophilic region coalesce more easily and are spread over the surface. Therefore, not only does icing takes place much easier, the bridging and ice propagation is much faster on the hydrophilic region. A sequence of images showing the ice propagation (moving parallel to the surface and perpendicular to the images) on the biphilic surface is shown in Figure 39b, with a yellow arrow indicating the planer ice front. The ice wave movement is evident in the hydrophilic region moving towards the superhydrophobic spot. Here, the blue circles indicate the droplets or droplets during icing process and the yellow circles show the iced droplets.

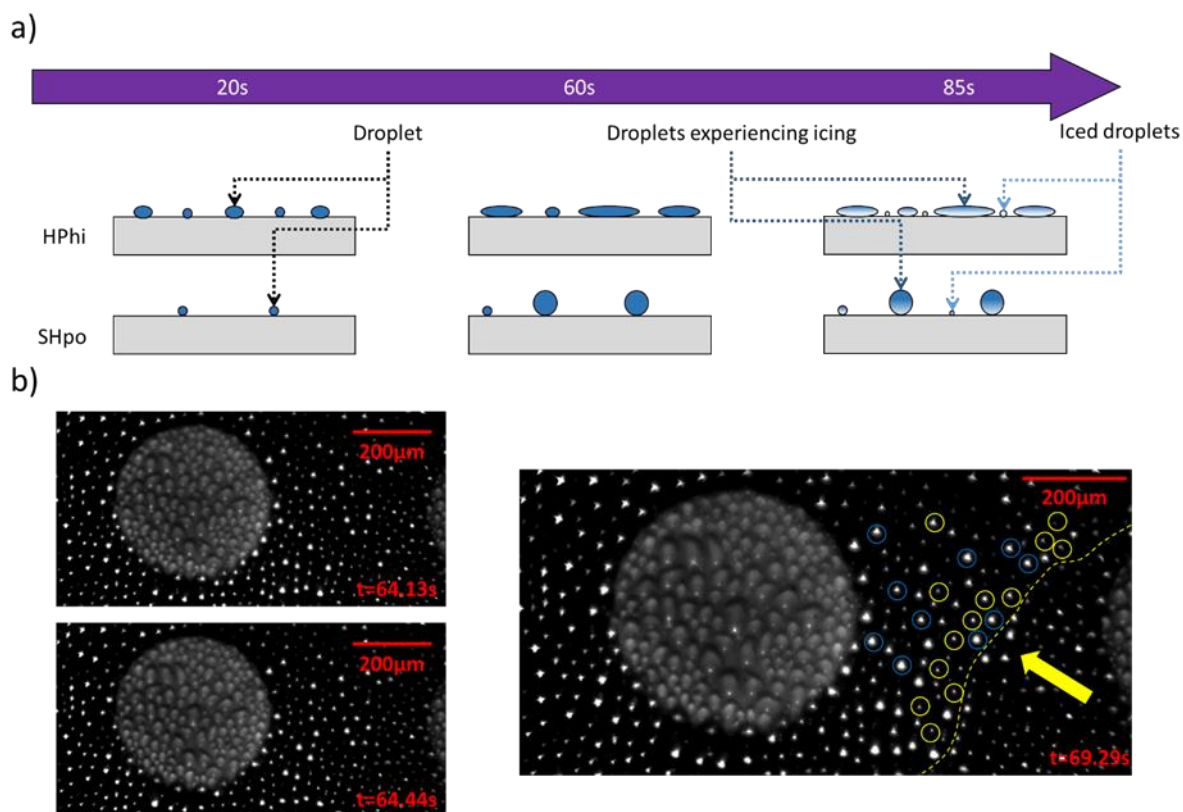


Figure 39. a) Schematic of drop condensation and icing on hydrophilic (HPhi) and superhydrophobic (SHpho) surfaces, b) Sequence of images showing icing at the temperature of  $-15^{\circ}C$  and relative humidity (RH) of 75% on sample D5.

### 5.3.2. Condensation icing

In order to investigate the effect of superhydrophobicity ratio on frosting, condensation icing was observed on each sample at the RH=55% and  $T_s = -8$  °C. Enough time was given and measured until the thickness of the frost layer reached 2 mm. The results indicate that as larger portions are designated to the superhydrophobic areas, frost formation and densification are prolonged.

Figure 40 indicates the required time for formation and densification of ice layer as a function of superhydrophobicity ratio. Time was measured starting from  $t=0$  representing the moment sample reaches  $T_s = -8$  °C until the Formation of a uniform ice layer with the thickness of 2mm. Formation of a uniform ice layer with the thickness of 2mm on the totally hydrophilic reference sample occurs within 6.2 mins while it takes 6.3 mins to observed a similar ice layer on sample D1 with the superhydrophobicity ratio of 1.76%. This is indicative of the fact that the presence of superhydrophobic islands with the diameter of 100  $\mu\text{m}$  on biphilic samples does not affect ice formation and densification significantly. However, an outstanding delay in icing (5.1 mins) is observed as the superhydrophobicity ratio increases from 78.50% (icing time = 23.3 mins) to 100% (icing time = 28.4 mins). A 2-mm thickness ice layer forms on D5 and D7 (superhydrophobicity ratio of 19.63% and 38.50%) after 11.0 mins and 12.0 mins, respectively.

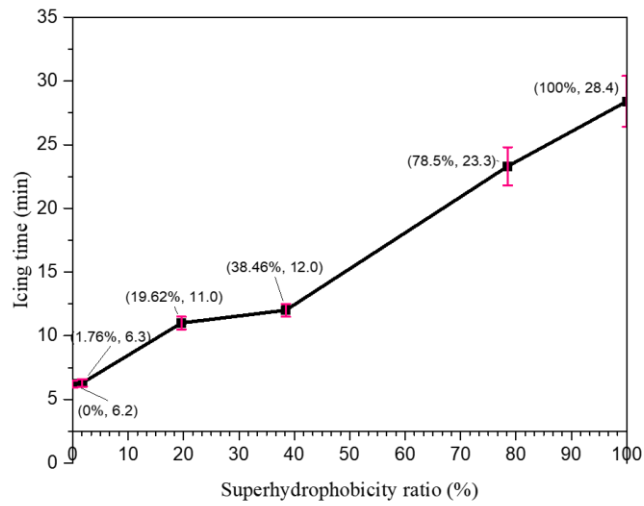


Figure 40. Superhydrophobicity ratio versus ice accumulation time on samples at RH=55% and  $T_s = -8^\circ\text{C}$ .

In order to show the effect of superhydrophobicity on icing an intermediate icing stage on the samples, at  $t=3.5$  mins after the substrates reached  $T_s = -8^\circ\text{C}$  is considered (Figure 41).

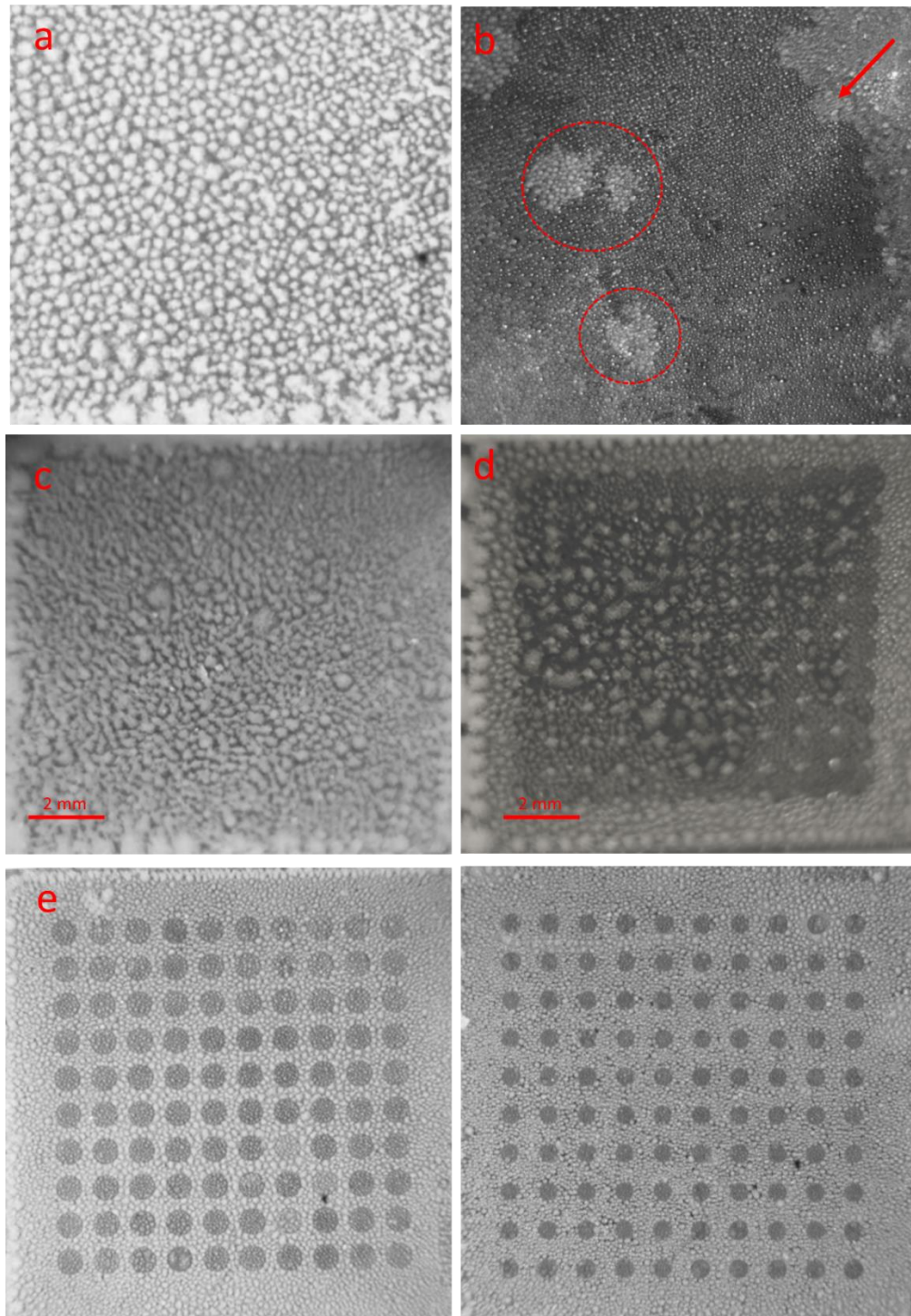


Figure 41. Intermediate icing stage on a) fully hydrophilic reference sample, b) fully superhydrophobic reference sample, c) sample D1000, d) sample D150, e) sample D700 and f) sample D500 at  $t=3.5$  mins after the substrates reach  $T_s = -8$  °C.

As can be seen in Figure 41a, the entire surface of the totally hydrophilic reference sample is covered uniformly by frozen droplets while minimal icing is observed on the totally superhydrophobic reference sample (shown with red regions in Figure 41b). Sample D1 (Figure 41c) having superhydrophobic islands with the diameter of 100 $\mu$ m indicates the similar behavior to totally hydrophilic reference sample. The bush shape of the droplets is indicative of dendrite formation on frozen droplets. Bridging between frozen droplets is observed at several points on the surface. Bridging is more obvious towards the edges as elongated ice clusters are detected (Figure 41c). While sample D1 is at an elevated freezing stage for 3.5mins after reaching  $T_s = -8$  °C, nonuniform freezing can be observed on sample D10 (Figure 41d). The presence of water droplets, frozen droplets with no or minimal dendrites formation and isolated ice clusters distant from each other are indicative of icing mitigation on sample D10. On the other hand, frozen droplets on samples D5 and D7 are visible (Figure 41e and 41f). On both samples, larger droplets form on the hydrophilic region while smaller and more distant ones are on the superhydrophobic spots. This suggests more condensation, ice formation and accumulations on the regions with higher wettability. Figure 42 displays the intermediate icing stage on all four samples at  $t=3.5$  mins after the substrates reach  $T_s = -8$  °C at higher magnifications. The red region in Figure 42a indicates advanced bridging between the frozen droplets on sample D1 while Uncomplete freezing on one side of the sample D10 is shown by the red region in Figure 42b. The lower intensity of ice crystallization and slower ice growth on superhydrophobic islands is more obvious on sample D5 and D7 in Figure 42c and d as less number of frozen droplets are observed on the silicon nanogras spots. Furthermore, the smaller size of frozen droplets on superhydrophobic regions represent lower interfacial heat transfer on these islands.

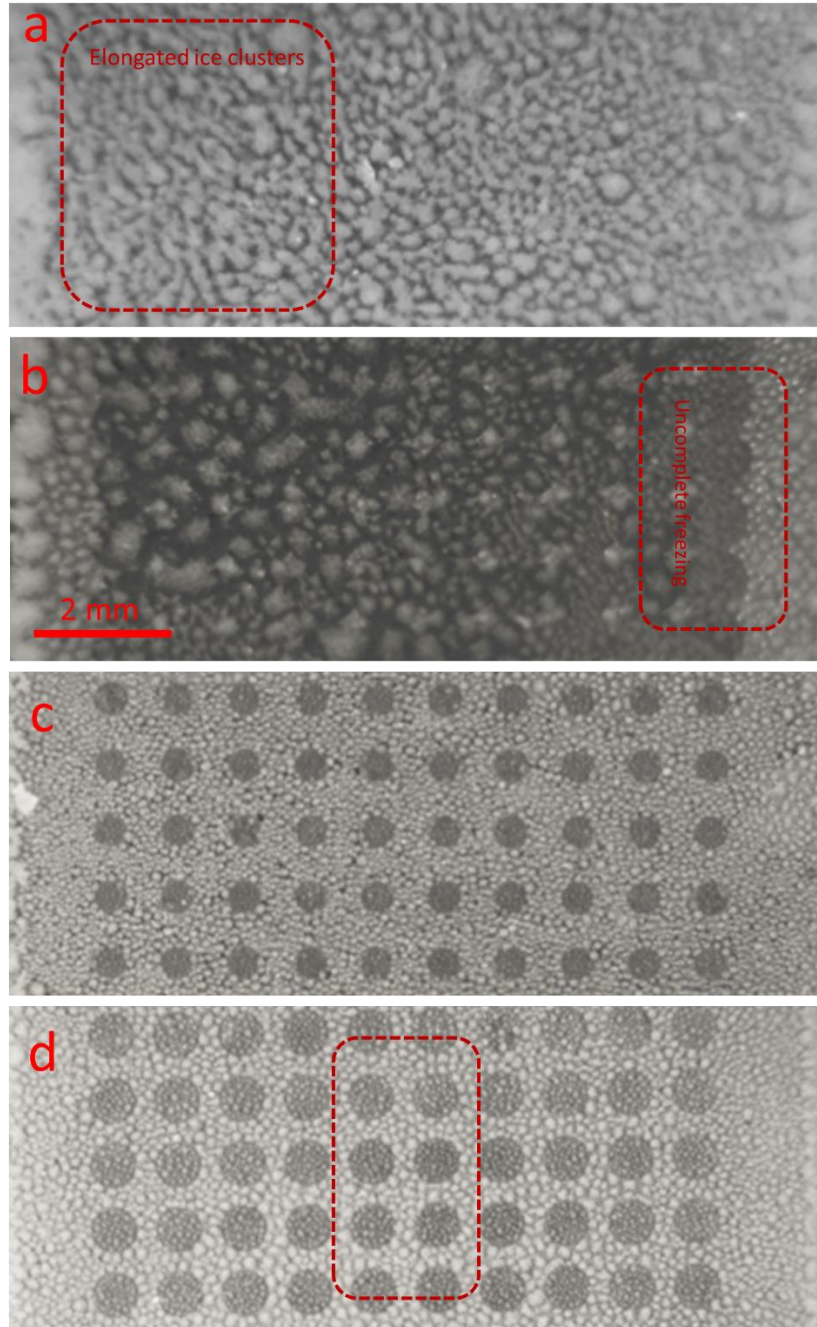


Figure 42. Intermediate icing stage on a) sample D1, b) sample D10, c) sample D5, and d) sample D7 at  $t=3.5$  mins after the substrates reach  $T_s = -8$  °C.

The presence of superhydrophobic islands on biphilic surfaces can be advantageous for anti-icing applications in terms of different aspects. As discussed earlier, superhydrophobic surfaces cause delay in condensation and icing due to the lower surface energy and interfacial heat transfer. Furthermore, due to the lower nucleation intensity and droplet coalescence jumping, a smaller number of droplets form on superhydrophobic surfaces, as clearly observed in all the experiments. This feature promotes the anti-icing performance of biphilic surfaces in two ways. Under condensation frosting condition, frost can propagate through a cluster of condensed droplets in a dominolike manner as one droplet freezes (Y. Jin, He, Guo, & Wang, 2017). An on-going evaporation-absorption phenomenon occurs between one frozen droplet and its nearby water droplets. While evaporation occurs in the neighboring water droplets (because of the latent heat release by freezing), water molecules get absorbed by the frozen one (because of vapor pressure gradient). This phenomenon leads to the ice bridging from the frozen droplet towards the water droplets, which results in frost propagation through the surface (Chavan et al., 2018). The possibility of the ice bridging only depends on geometrical parameters of the adjacent droplets such as the distance and droplet size. Other parameters such the temperature, ambient humidity, and surface wettability can only affect the kinetics of this phenomenon (Graeber, Dolder, Schutzius, & Poulikakos, 2018). Since the droplets are more distant on the superhydrophobic regions, ice front growth cannot propagate uniformly and effectively. Therefore, a discrete layer of ice is observed on biphilic surfaces during phase change. The discrete nature of the ice layer is clearer as the superhydrophobicity ratio increases. Figure 43 shows the schematic of ice propagation on hydrophilic and superhydrophobic surfaces in order to indicate the difference in ice propagation behavior of the domains on a biphilic surface.

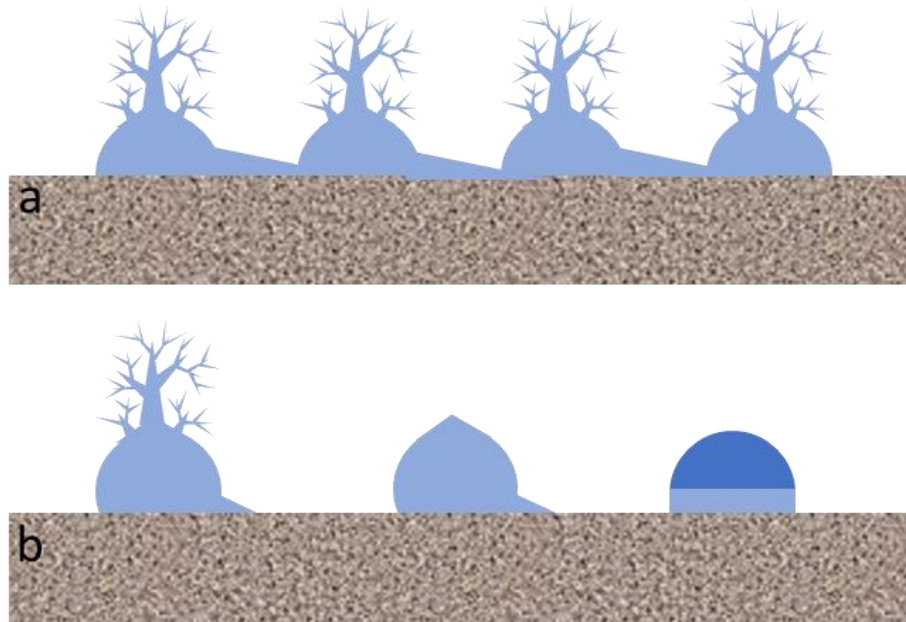


Figure 43. Ice propagation through bridging on a) hydrophilic surface and b) superhydrophobic surface.

### 5.3.2. De-frosting

In order to investigate the effect of superhydrophobicity ratio and biphilic designs on dynamic de-frosting, de-frosting of an ice layer with the thickness of 2mm was observed on each sample. De-icing was performed at the temperature of 0°C by turning off the de-electric device while the chiller and associated water circulation were still working at 0°C. Normal-view time-lapse images of dynamic de-icing on sample D5 with the diameter to the edge-to-edge spacing ratio (D: S) of 1: 1 is shown in Figure 44. The initiation of de-icing is represented by the time  $t = 0$  s. As shown in Figure 44, the first signs of de-icing are observed on superhydrophobic regions. Superhydrophobic spots are the first regions that become ice free ( $t = 12$  s). At  $t = 13$  s, defrosting initiates on hydrophilic regions starting from one edge of the sample and ice layer rupture can be observed immediately ( $t = 14$  s). Slush/water travels through the hydrophilic networks while superhydrophobic spots are kept clean from  $t=14$  s to  $t=19$  s. The whole amount of melted water is dragged to one side of the sample as

leave the surface clean ( $t=20$  s). As the melting is completed the melt water is accumulated at the corners at  $t = 23$ s and no more slush/water mobility is observed on the surface.

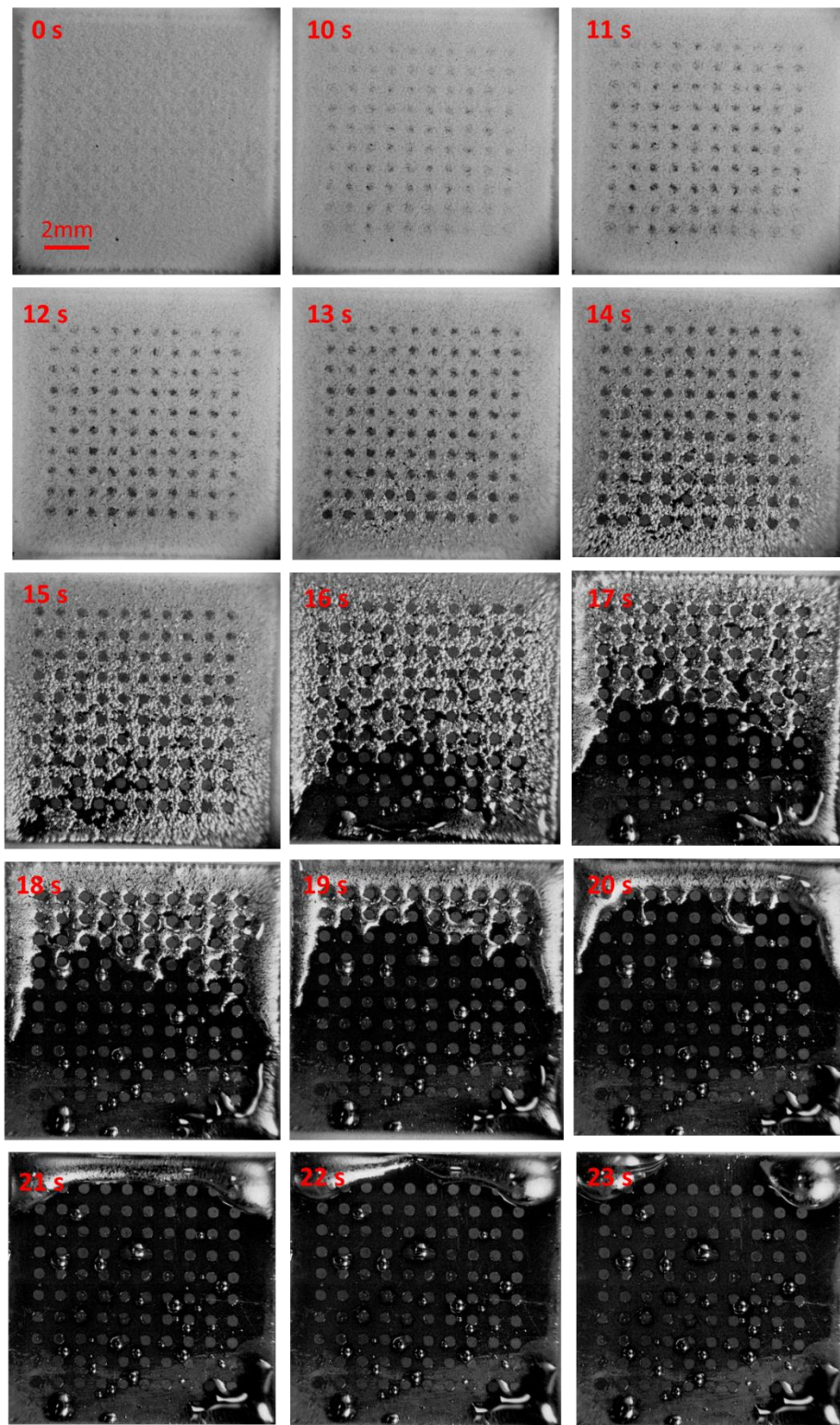


Figure 44. Normal-view time-lapse images of dynamic de-icing at 0 °C on sample D5.

The presence of preferable areas for de-icing leads to the formation of a nonuniform ice layer on the sample which occurs as a result of heterogenous wettability. A more porous layer of ice forms on the superhydrophobic spots which makes them more prone to melting. As melting continues, slush/water is dragged to the hydrophilic regions and superhydrophobic spots were the first areas that become free of slush/water. The hydrophilic regions act as a drainage network through the surface and direct slush/water to the corners of the sample. The presence of dual wettability on the surface results in a Laplace pressure gradient (due to the change in surface forces) which can create a dynamic defrosting through the sample (Gurumukhi et al., 2020). As can be observed slush/melt water mostly travels in between the superhydrophobic spots and is drained to the hydrophilic strip around the sample. An almost complete passive cleaning occurs for sample D5. The melt water is almost completely wiped off the surface and accumulated as puddles at the corners. A small amount of water is retained at few spots on the sample as droplets which easily evaporate.

Although the presence of regions with two different wettability values is the main reason for dynamic defrosting, it should be noted that the surface pattern design plays an important role in slush/water mobility. Liquid travel on a hydrophilic wedge shape track occurs due to the unbalanced capillary forces along the length direction which drags the liquid from a narrow region of a wettable surface to the wider section (Ghosh, Ganguly, Schutzius, & Megaridis, 2014). The liquid transport is strongly driven by the Laplace pressure gradient, which is caused by the surface pattern. The net axial Laplace pressure gradient governing the liquid transport can be expressed as (Ghosh et al., 2014):

$$\frac{dP}{dx} \sim - \frac{d}{dx} \left[ \frac{\gamma_{LG}}{r(x)} \right] \sim - \gamma_{LG} \frac{d}{d\delta(x)} \left[ \frac{2\sin\theta(x)}{\delta(x)} \right] \frac{d\delta(x)}{dx} \sim 2\gamma_{LG} 2\sin\theta \frac{1}{\delta(x)^2} \alpha \quad (4)$$

where  $\gamma_{LG}$ ,  $r(x)$ ,  $\delta(x)$ , and  $\theta(x)$  represents the surface energy per unit interface area between the liquid and the gas, local curvature of the liquid, local track width, and apparent contact angle, respectively. According to the equation 4, the capillary pressure gradient is directly proportional to the wedge angle  $\alpha$  and inversely proportional to the square of the local track width  $\delta(x)$ .

The circular shape of the superhydrophobic islands can create a pumping capillary force acting on slush/water on the surface during melting creating an effect similar to wedge

shape tracks. In this case, the curved edge of the islands constructs hydrophilic tracks with  $\alpha$  and  $\delta$  changing locally. The repeating converging – diverging wettability gradients through the surface generate a pumping effect through the surface which stimulates the dynamic defrosting.

The apparent contact angle  $\theta(x)$  of the liquid travelling along the two edges of the track in Equation (4) cannot be defined by the Young's equations and it is affected by the local track width and local liquid volume contained per unit length. Therefore, the calculation of the capillary force from the above equation requires complementary numerical analysis for the variation of angle  $\theta(x)$  with respect to  $x$  (Ghosh et al., 2014).

Figure 45 shows Normal-view time-lapse images of passive de-icing on sample D7 with the D: S = 7: 3. Sample D7 has a superhydrophobicity ratio twice higher than sample D5 because of the larger superhydrophobic spots (200  $\mu\text{m}$  larger in diameter). As seen, although passive cleaning occurs to some extent, the biphilic design in sample D7 is not as successful as in sample D5.

The first signs of de-frosting are observed on superhydrophobic spots. Superhydrophobic islands are visible at  $t=15\text{s}$  indicating the slush travel toward hydrophobic regions. At  $t=20\text{s}$  while there is still slush on superhydrophobic spots, disruption of ice layer on hydrophobic regions is observed. However, superhydrophobic islands on sample D5 become completely clean ( $t=15\text{s}$ ) as de-frosting initiates on hydrophilic substrate. The delay in slush//water removal off superhydrophobic islands can be contributed to drowsy slush/water flow on sample D7. Up to  $t=29\text{s}$ , most of the melt water is directed toward the edges through the hydrophilic network, however, a small amount of water cannot be transferred and retained as a puddle at the upper side of the sample ( $t=30\text{s}$  and  $t=31\text{s}$ ). Given enough time ( $t=36\text{s}$ ), the accumulated water at the edges and the retained water on the surface shrink due to de-wetting and form droplet puddles through the surface.

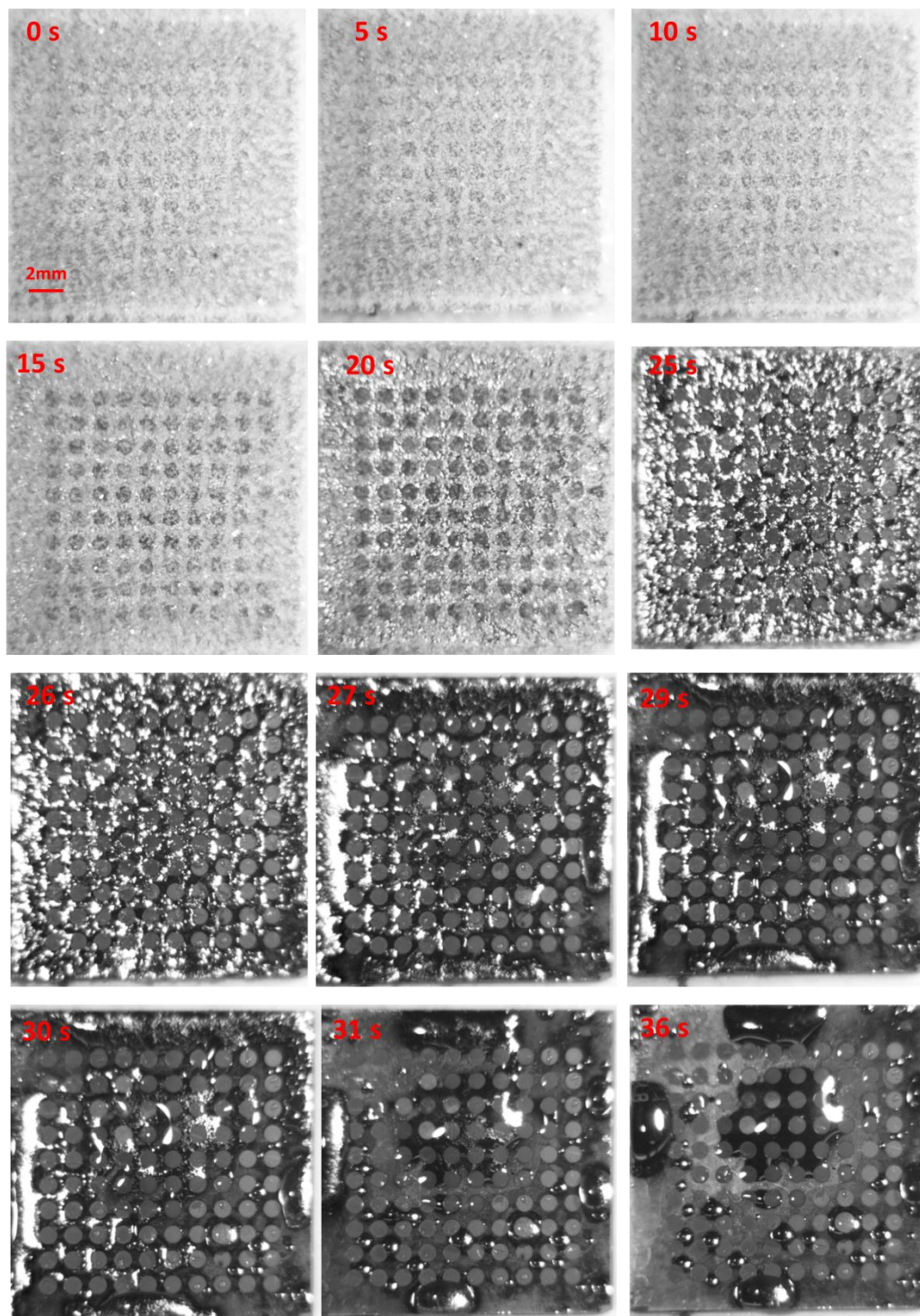


Figure 45. Normal-view time-lapse images of dynamic de-icing at 0°C on sample D7.

Although slush/water was dragged to the hydrophilic areas on sample D7, consistent flow of slush/water does not happen at some locations and some shortcomings exist. Frost melting generally initiates at the frost-solid interface, and the melt water at the interface (beneath the frost) is dragged to the surrounding hydrophilic regions. Due to the porous structure of ice on superhydrophobic regions, frost breakup occurs and leads to the formation of satellite droplets on these water repellent islands (Boreyko et al., 2013). Satellite droplets are also observed on hydrophilic regions. By taking a closer look at the images, the droplets mainly form as a result of the disruption of the slush/water flow at the narrowing hydrophilic passages. Due to the larger diameter of superhydrophobic islands, smaller portion is designated to the hydrophilic regions. Therefore, ice and resulting slush/water cannot form a solid structure through the so-called drainage network. Narrower hydrophilic passages, nonuniform structure of ice and unbalanced forces (viscous forces, interfacial forces, etc.) acting on the liquid are the main reasons for satellite droplets on hydrophilic regions. Satellite droplets have been previously detected on both superhydrophobic and hydrophilic regions during defrosting as well (Hai Wang et al., 2023a).

Furthermore, as dynamic de-frosting is seen on sample D7, it can be noticed that narrower passages compared to sample D5 (D: S = 7: 3) do not have the capacity to hold and channel slush/water through the surface. However, water buildup happens as only one droplet puddle which is actually less problematic since the remnant water is accumulated. Brinkmann et. al. (Brinkmann & Lipowsky, 2002) indicated that the shape of liquid accumulation on rectangular tracks is governed by the ratio  $\frac{V}{L^3}$  (where V and L are defined as the liquid volume and superhydrophilic track width, respectively). If  $\frac{V}{L^3}$  exceeds a critical value, the liquid accumulates as localized droplet with a contact area overlapping with the superhydrophobic region (Brinkmann & Lipowsky, 2002). Although the study discusses a static state, similar phenomena can be observed in our case. It can be concluded that the capacity or incapacity of the hydrophilic network to channel the slush/water flow highly depends on the geometry of the surface pattern and amount of melt water.

Considering same amount of ice formed on all of the samples, V is 200 mm<sup>3</sup>. Consequently,  $\frac{V}{L^3}$  for sample D5 and D7 is obtained as  $1.6 \times 10^3$  and  $7.4 \times 10^3$

respectively. Higher value of  $\frac{V}{L^3}$  for sample D7 result into the small amount of water retained on the sample and not being able to be channeled to the edges.  $1.6 \times 10^3$  can be considered as the threshold for the dynamic slush/water flow leading to passive cleaning as for the surface patterns with higher  $\frac{V}{L^3}$  water retention is considerable.

In order to conduct further investigation on the effect of superhydrophobicity ratio on de-icing behavior, samples with relatively high and low superhydrophobicity ratios were tested. Figure 46 shows normal-view time-lapse images of defrosting on sample D10 with a superhydrophobicity ratio of 78.5%. Due to the higher superhydrophobicity ratio of the sample and minor wettability gradient, slush mobility during melting and water transportation after the phase change is neglectable. After de-frosting, water retention is observed as satellite droplets and water puddles on one side the surface.

As the coolant is turned off at  $t=0s$ , the ice layer on sample D10 starts to melt. Defrosting can be realized as the biphilic surface pattern becomes more visible ( $t=40s$ ) however, due to low Laplace pressure gradient because of to the considerably small hydrophilic regions, only a slight dynamic activity is seen until  $t=48s$ . The slush water on the regions close to the hydrophilic strip around the sample are dragged to the edges. Therefore, superhydrophobic islands close to the edges are the first spots that become clean ( $t=52s$ ). As melting continues, droplet accumulation occurs at different locations on the sample ( $t=54s$ ). Eventually, water retention is observed as three puddles on the surface while keeping the central region of the sample dry ( $t=60s$ ). Given enough time the puddles shrink due to de-wetting and no further activity is observed after 90s.

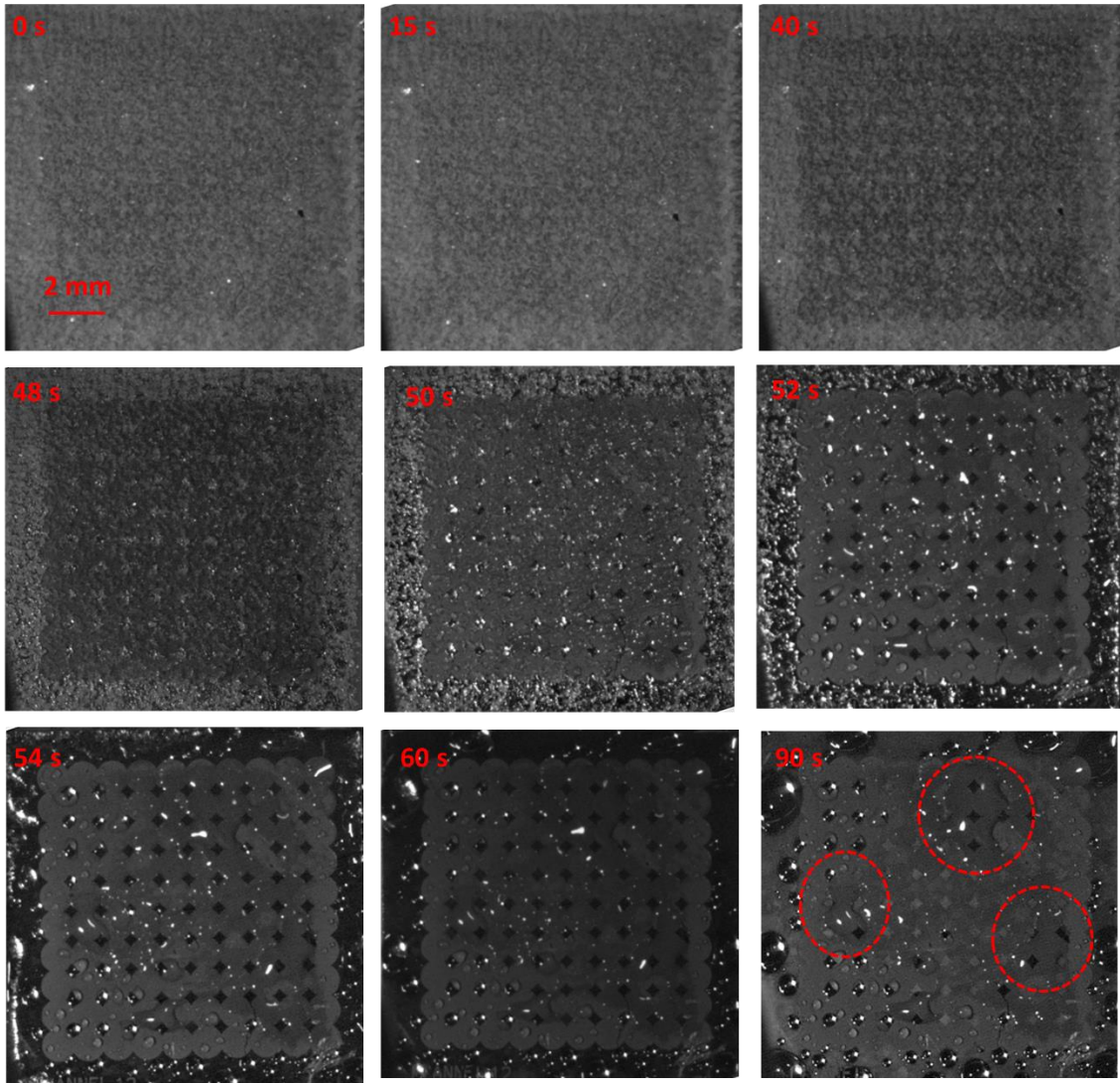


Figure 46. Normal-view time-lapse images of dynamic de-icing at at 0°C on sample D10.

De-frosting on a superhydrophobic surface leads to the formation of satellite droplets and droplet/puddle depending on the initial thickness of the frost (Boreyko et al., 2013). Satellite droplets are most likely form when the melting frost layer is thin. However, as the frost layer thickness increases, the retained water tend to shrink and form a continuous droplet/puddle due to the de-wetting phenomenon. Although sample D10 has relatively high

superhydrophobicity ratio, the water retention after de-frosting is slightly spread compared to a fully superhydrophobic surface. This is attributed to the small hydrophilic regions located through the surface not being able to create a slush/water mobility but interfering with low surface energy along the surface. Similar behavior was observed by Wang et. al (Hai Wang et al., 2023a). It is worthy to mention that the central region of the sample is completely cleaned off water which isn't observed for the two previous samples. However, water remnant wasn't as accumulated as much as it is in previously test samples, which can be problematic in later icing cycles by accelerating icing or leading to material degradation over time.

In order to investigate further the interfacial phenomena on sample D10, de-frosting a thin layer of ice (just enough to cover the surface) was studied on this sample (Figure 47). Due to the low amount of ice on the surface, defrosting occurs in a couple of seconds ( $t=3s$ ). Droplet coalescence and formation of larger droplets are more visible on hydrophilic regions showed with red circles at  $t=3s$  and  $t=5s$ . Meanwhile coalescence induced jumping leads to the droplet removal from superhydrophobic islands and the removed droplets travel to the adjacent hydrophilic regions ( $t=7s$  and  $t=9s$ ). Although a significant slush/water dynamic does not occur on sample D10 during de-frosting, individual water droplets mobility is visible which contributes to the surface cleaning.

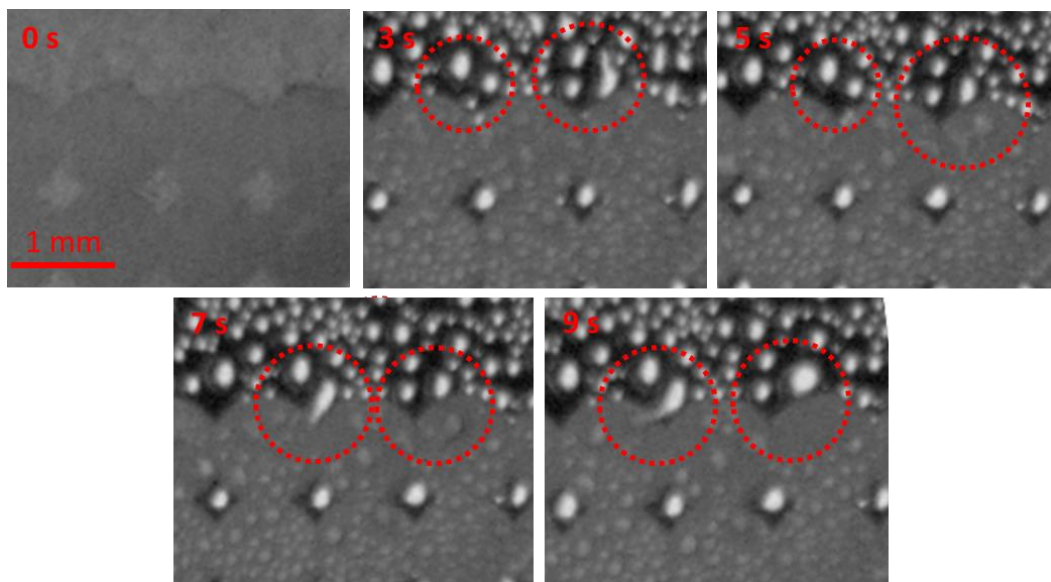


Figure 47. Normal-view time-lapse images of dynamic de-icing of a thin layer of ice at 0°C on sample D10.

Figure 48 shows normal-view time-lapse images of defrosting on sample D1 having a superhydrophobicity ratio of 1.76%. De-frosting behavior of sample D1 is similar to the behavior of a hydrophilic surface. De-frosting is first detected at one corner of the sample ( $t=3.6\text{s}$ ). Defrosting continues as more droplets form on the surface until  $t=4.5\text{s}$ . At  $t=4.5\text{s}$  the whole layer of ice is melted and water droplets are covered the entire surface. Given enough time, droplet coalescence is observed after defrosting is completed. However, after  $t=5\text{s}$  no more interfacial activity is visible on the surface.

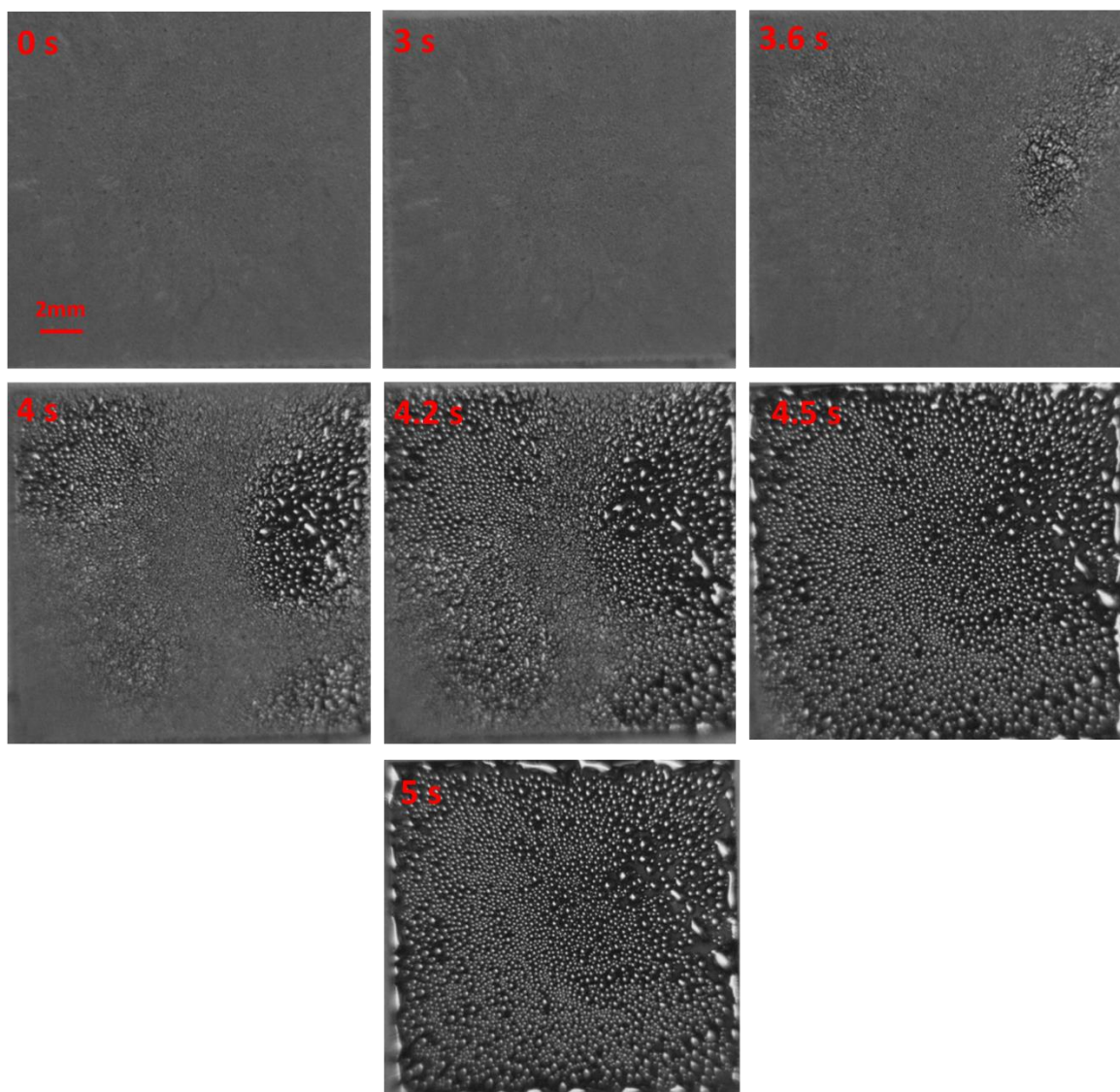


Figure 48. Normal-view time-lapse images of dynamic de-icing at 0°C on sample D1.

As frost is melting on sample D1, droplets form uniformly on the entire sample due to the high wettability of the surface. Water retention in form of droplets is visible through the sample. Due to the low surface energy of superhydrophobic surfaces, water molecules tend to bond with each other instead of interacting with the surface. Therefore, water accumulation as large droplets or bulged puddles are observed on the sample with a higher superhydrophobicity ratio. However, on a hydrophilic surface, in order to minimize the system's energy, the melted water covers the entire surface as small droplets with high

wettability. The results indicate that although the superhydrophobicity ratio of 1.76% has positive effects on properties such as heat transfer coefficient and critical heat flux in condensation and boiling, it does not have any significant effect on de-frosting behavior.

Figure 49 shows the final stage of the de-icing on the totally hydrophilic and superhydrophobic reference samples. As it can be seen in Figure 49a, after defrosting, the water retention is in the form of relatively large droplet puddles and a few small satellite droplets as it was reported by (Boreyko et al., 2013). This is clearly indicative of the fact that water molecules on the superhydrophobic surface tend to bond with each other rather than interacting with the substrate. However, the totally hydrophilic reference sample is covered uniformly with smaller water droplets similar to what was observed on sample D1 due to the higher surface energy and wettability of the hydrophilic surface.

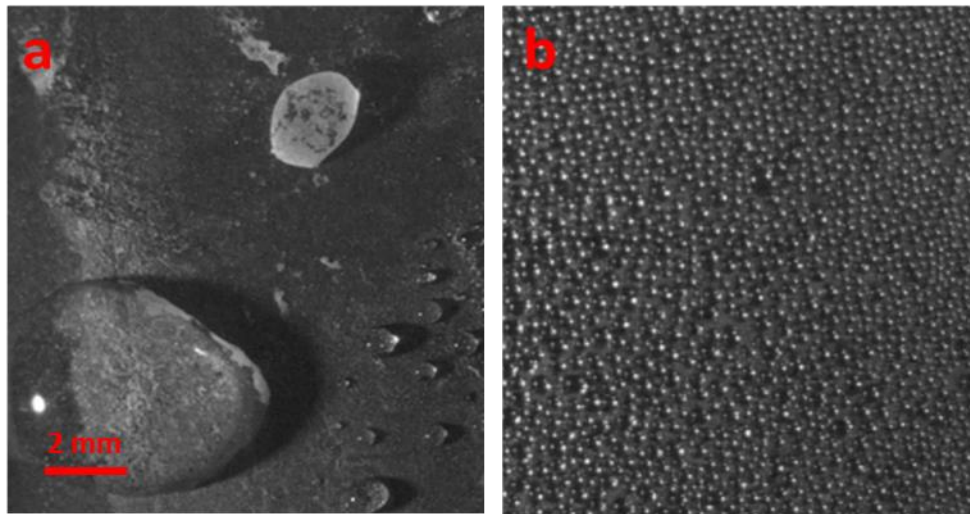


Figure 49 Normal-view time-lapse images of dynamic de-icing at 0°C on a) totally superhydrophobic and b) totally hydrophilic reference samples.

Figure 50 shows the cleaning time as a function of superhydrophobicity ratio of the biphilic samples. With an increase in superhydrophobicity ratio, the system requires more time to stabilize. Due to the low superhydrophobicity ratio in sample D1, Laplace pressure gradient is created which does not generate any dynamic flow. Therefore, defrosting occurs within only 5 s and the droplets cover the entire surface with no further activity.

As the diameter of superhydrophobic spots increases, the duration of dynamic flow increases. It is worth mentioning that biphilic design of sample D5 can create an almost complete surface within only 23 seconds. On the other hand, although sample D7 and D10 showed some short coming in creating a consistent flow of slush/water, it takes longer until no further activity is observed on them. This suggest that the Laplace pressure gradient is generated on these samples, however it is not sufficient to provide the complete cleaning. The dynamic flow of slush/water on sample D10 is active for about 90 s until no further interfacial event is observed. As a result of high superhydrophobicity ratio, the retained water tends to shrink due to the de-wetting phenomenon, however small hydrophilic regions through the sample create an unbalanced force distribution and prolong the interfacial activities. Although the melt water on the totally superhydrophobic surface was accumulated as two large droplets and a large area of the surface was cleaned, the longest activity (135 s) was observed on this sample. Furthermore, by comparison of the dynamic flow on sample D1 and the totally hydrophilic reference sample, it can be concluded that introducing superhydrophobic islands to hydrophilic substrate with the diameter of 100  $\mu\text{m}$  does not lead to a noticeable difference in de-frosting behavior.

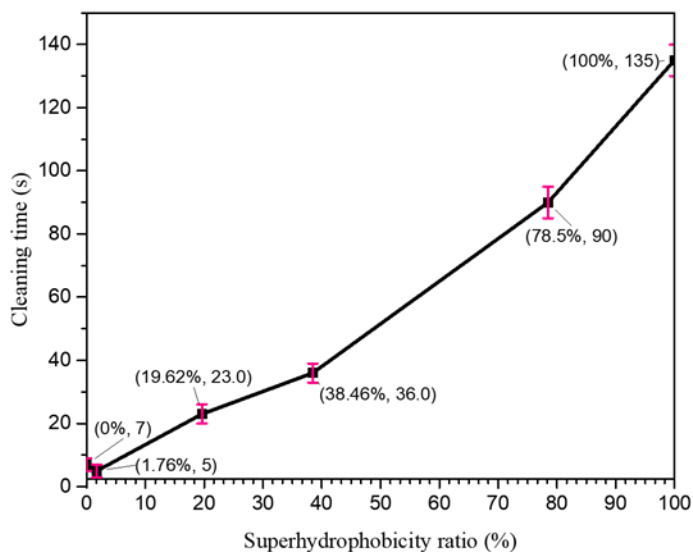


Figure 50. Cleaning time at 0°C - superhydrophobicity ratio.

According to the results, sample D5 has the best performance in terms of passive cleaning. The water is completely wiped off the sample and delivered to the corners. This is due to the Laplace pressure gradient and the capillary forces which are generated due to the proper biphilic design. Slush/water flow is also visible on sample D7; however, only partial cleaning occurs. Motezaker et. al (Motezakker et al., 2019) reported heat transfer coefficient and critical heat flux enhancements for biphilic surfaces having superhydrophobic islands with  $D \leq 700 \mu\text{m}$ . Superhydrophobic islands with  $D=700$  resulted in the maximum critical heat flux enhancement (38.46%). This implies that in case of water retention on samples with  $D \leq 700 \mu\text{m}$ , the molten water can be removed from the surfaces efficiently. Therefore, samples with  $D \leq 700$  can provide a more effective and economical active defrosting in terms of ice and water removal as a result of both Laplace pressure gradient and high heat flux enhancement.

Compared to the literature (Gurumukhi et al., 2020; Hai Wang et al., 2023b), similar results were obtained for de-frosting behavior of biphilic surfaces. Gurumukhi et. al (Gurumukhi et al., 2020) investigated striped biphilic designs for passive cleaning. They reported successful passive cleaning for the sample having superhydrophobic width to hydrophilic width ratio ( $L_{\text{SHPO}}: L_{\text{SHPI}}$ ) of 1: 1 (superhydrophobicity ratio of 50%). Wang et. al. (Hai Wang et al., 2023a) observed complete cleaning on a biphilic design with superhydrophobic squares having the width to the edge-to-edge spacing ratio ( $L_{\text{SHPO}}: S$ ) of 1:1. According to the results, superhydrophobicity ratio may not be an accurate criterion to describe the passive cleaning behavior of biphilic surfaces. Passive cleaning can only happen due to the proper dynamic slush/water flow through the surface generated from the Laplace pressure gradient which mostly depends on the surface pattern and geometry of the domains with different wettability values. Therefore, a complete passive cleaning can be achieved on biphilic designs with the domain width ratio of 1: 1 independent of the size of the samples and domain shape.

#### 5.4. Conclusion

In this study, biphilic surfaces consisting of superhydrophobic circular domains on a hydrophilic substrate were investigated in terms of icing/de-icing behavior. Samples with different superhydrophobicity ratios ( $A^* = A_{\text{superhydrophobic}}/A_{\text{total}}$ ) were designed and fabricated. In order to investigate the biphilic design for a complete passive cleaning with no additional external energy, the de-frosting was performed at 0°C. The biphilic sample having superhydrophobic islands with the diameter of  $D=500 \mu\text{m}$ , the superhydrophobicity ratio ( $A^*$ ) of 19.62%, and the diameter to edge-to-edge ratio ( $D: S$ ) of 1: 1 leads to a complete passive cleaning within 23s. The Laplace pressure gradient generated due to the presence of the domains with different wettability results in a dynamic slush/water flow. The geometry properties of the biphilic design is of great importance as well. The circular shape of the superhydrophobic islands generate a capillary force on the slush/water flow moving on the hydrophilic network and consecutively creates a pumping force through the network. The portion of superhydrophobic region to hydrophilic area in each cross section is one of the main parameters to achieve the complete clean surface through dynamic de-frosting. Although the samples with a higher superhydrophobicity ratio exhibits slush/water mobility, complete cleaning is not achieved. However, due to the interfacial phenomena occurring due the biphilic design, the retained water has different behavior on each surface. The presence of superhydrophobic areas leads to the formation of porous and not interconnected layer of ice which is more prone to melting.

## Chapter VI: Conclusions and future works

### 6.1. Conclusions

In this thesis, fundamentals of ice formation and accumulation as well as de-icing through both thermodynamic and interfacial phenomena were discussed. Frosting/de-frosting was observed on different engineered surfaces through an attempt to simulate the real life conditions during experiments. Furthermore, anti-icing coatings and surfaces were designed and developed in order to address the shortcomings of the current approaches. The coatings and surfaces were selected according to the needs.

In this thesis, a MOF-based functionalized superhydrophobic multiscale coating (SHMC) with an apparent CA value larger than  $171^\circ$ , rolling angle of  $<5^\circ$ , and contact angle hysteresis of  $<3^\circ$  was developed. Complex and multistep fabrication processes were among the major limitations of the current approaches in the development of superhydrophobic coatings for industrial applications. However, the coating proposed in this thesis was prepared using the practical spray coating method on aluminum and copper surfaces, which are the mostly used materials in the relevant industries. The multiscale surface texture of the coating was achieved due superposition of nanoparticles and highly porous structure of ZIF-8. Multiscale, randomness, and self-similarity features of SHMC texture suggested the fractal nature of the coating, and a fractal theory-based model of water contact angle was adapted

to reveal the non-wetting mechanism on SHMC. Different modes of icing were observed on plain (on-surface) and coated surfaces (off-surface), resulting in different ice morphology due to the presence of the coating on the substrate. The multiscale texture of the SHMC extended the icing time by at least 300% and maintained its superhydrophobicity for more than 30 icing/deicing cycles. Furthermore, reduction in heat transfer rate during the total droplet contact time on the SuperHydrophobic Multiscale Coating was realized. Taking of these into account, this coating could be considered as a strong candidate for industrial applications, especially wind turbine blades.

Although superhydrophobic surfaces delay ice formation and accumulation, active-frosting is an inseparable part of industrial de-icing techniques. Furthermore, superhydrophobic surfaces are not suitable for all the industrial conditions which are prone to icing such as ventilation. This thesis provides information on a surface design having hybrid wettability for such applications. For this the superhydrophobicity ratio ( $A^* = A_{\text{superhydrophobic}}/A_{\text{total}}$ ) of biphilic surfaces were designed as the major parameter. The biphilic surface consisting of superhydrophobic islands with the diameter of  $D=500 \mu\text{m}$  on hydrophilic substrates having superhydrophobicity ratio ( $A^*$ ) of 19.62%, and the diameter to edge-to-edge ratio (D: S) of 1: 1 was capable of complete passive cleaning. Furthermore, as the superhydrophobicity ratio increases, more delay in ice formation and accumulation occurs. High superhydrophobicity ratio also leads to a more porous and a not interconnected ice structure. Therefore, it can be concluded that the choice of a surface design is actually a trade off between its icing and de-icing behavior.

## 6.2. Future prospective

- In addition to the hydrophobic nature, ZIF-8 is intrinsically oleophilic. Highly porous structure and oleophilic nature of ZIF-8 makes it a good candidate for lubricant infused coatings in anti-icing applications in terms of durability.

- Different synthesis methods, reactant ratios, and synthesis parameters such as temperature can directly affect the particle size, particle morphology and porous structure of ZIF-8. Since the outstanding anti-icing properties of the superhydrophobic multiscale ZIF-8 based coating (SHMC) developed in this thesis was highly associated with the nanoparticle properties, the effect of synthesis process on the anti-icing behavior of a ZIF-8 based coating can be studied.
- De-icing experiments were carried out on small scale samples which also leads to limited ice formation. In order to provide a better understanding about the applicability of proposed biphilic design in industrial applications larger samples will be useful.
- The wettability gradient between the superhydrophobic and hydrophilic domains create the Laplace pressure gradients. Therefore, further studies can be performed in order to find the optimum configuration the wettability gradient for biphilic designs fabrications.
- Biphilic designs having superhydrophobic islands with diameters decreasing as they reach to the edge of the samples can have a more efficient performance in terms of channeling the melt water off the surface. However, again an optimum for diameter gradient should be obtained.

### 6.3. Contribution to the scientific community

This dissertation suggests a novel multiscale superhydrophobic zeolitic imidazole framework-based coating with outstanding anti-icing performance. The coating is developed through practical spray coating method which is aimed to be used for energy systems such as wind turbine blades. Dense and uniform distribution of highly porous ZIF-8 nanoparticles proposes a multiscale (subnano-nano-micro) structure to the surface that leads to an extraordinary water repellency. The interfacial phenomena and physics of condensation and icing including three phase contact line, interfacial heat transfer, ice growth modes are

thoroughly and fundamentally investigated on this coating by employing hybrid methods. The capillary pressure generated within the remarkable multiscale surface structure prevents the droplets from penetrating into it and reduce the risk of condensation-induced freezing under different variant supercooling and relative humidity conditions and within continuous icing/deicing cycles. Furthermore, excellent chemical and thermal durability of ZIF-8 makes the coating a strong candidate for industrial systems such as solar panels along with wind turbine blades. A detailed investigation and discussion on static and dynamic icing as well as condensation frosting can be found in this thesis. All the involved phenomena during the course of icing were visualized and discussed fundamentally.

This dissertation also proposes a functionalized biphilic design consisting of superhydrophobic islands surrounded by hydrophilic regions for optimum icing/de-icing behavior. The biphilic design is aimed at complete passive cleaning during defrosting with minimal energy consumption for the water/ice removal off the engineering surfaces. The biphilic surface is proposed as it can create an efficient Laplace pressure gradient through the surface in order to channel the slush water through the surface and clean the surface. Furthermore, the biphilic design leads to the formation of uninterconnected and nonuniform ice structures which leads to acceleration in melting and easier ice removals. The optimum biphilic design is realized as fundamental studies on interfacial phenomena during frosting/de-frosting were performed. The proposed surface is a strong candidate for ventilation and refrigeration systems as can create a balance in condensation, frosting, and defrosting.

## References

- Abbasiasl, T., Chehrghani, M. M., Sadaghiani, A. K., & Koşar, A. (2021). Gradient mixed wettability surfaces for enhancing heat transfer in dropwise flow condensation. *International Journal of Heat and Mass Transfer*, *179*, 121664.
- Aboubakri, A., Ahmadi, V. E., Celik, S., Sadaghiani, A. K., Sefiane, K., & Kosar, A. (2021). Effect of surface biphilicity on FC-72 flow boiling in a rectangular minichannel. *Frontiers in Mechanical Engineering*, *7*, 755580.
- Adachi, K., Saiki, K., & Sato, H. (1998). *Suppression of frosting on a metal surface using ultrasonic vibrations*. Paper presented at the 1998 IEEE Ultrasonics Symposium. Proceedings (Cat. No. 98CH36102).
- Adachi, K., Saiki, K., Sato, H., & Ito, T. (2003). Ultrasonic frost suppression. *Japanese journal of applied physics*, *42*(2R), 682.
- Ahmadi, S. F., Nath, S., Iliff, G. J., Srijanto, B. R., Collier, C. P., Yue, P., & Boreyko, J. B. (2018). Passive antifrosting surfaces using microscopic ice patterns. *ACS Applied Materials & Interfaces*, *10*(38), 32874-32884.
- Awadallah-F, A., Hillman, F., Al-Muhtaseb, S. A., & Jeong, H.-K. (2019). On the nanogate-opening pressures of copper-doped zeolitic imidazolate framework ZIF-8 for the adsorption of propane, propylene, isobutane, and n-butane. *Journal of Materials Science*, *54*(7), 5513-5527. doi:10.1007/s10853-018-03249-y

- Barthlott, W., & Neinhuis, C. (1997). Purity of the sacred lotus, or escape from contamination in biological surfaces. *Planta*, 202(1), 1-8. doi:10.1007/s004250050096
- Bayer, I. S., & Megaridis, C. M. (2006). Contact angle dynamics in droplets impacting on flat surfaces with different wetting characteristics. *Journal of Fluid Mechanics*, 558, 415-449. doi:10.1017/S0022112006000231
- Benam, B. P., Ahmadi, V. E., Motezakker, A. R., Saeidiharzand, S., Villanueva, L. G., Park, H. S., . . . Koşar, A. (2023). A parametric study on pool boiling heat transfer and critical heat flux on structured surfaces with artificial cavities. *Applied Thermal Engineering*, 221, 119841.
- Bhushan, B., Jung, Y. C., & Koch, K. (2009). Micro-, nano- and hierarchical structures for superhydrophobicity, self-cleaning and low adhesion. *Philos Trans A Math Phys Eng Sci*, 367(1894), 1631-1672. doi:10.1098/rsta.2009.0014
- Bhushan, B., Jung, Y. C., & Koch, K. (2009). Micro-, nano-and hierarchical structures for superhydrophobicity, self-cleaning and low adhesion. *Philosophical Transactions of the Royal Society A: Mathematical, Physical and Engineering Sciences*, 367(1894), 1631-1672.
- Boreyko, J. B., & Collier, C. P. (2013). Delayed frost growth on jumping-drop superhydrophobic surfaces. *ACS nano*, 7(2), 1618-1627.
- Boreyko, J. B., Srijanto, B. R., Nguyen, T. D., Vega, C., Fuentes-Cabrera, M., & Collier, C. P. (2013). Dynamic defrosting on nanostructured superhydrophobic surfaces. *Langmuir*, 29(30), 9516-9524.
- Borigo, C. J. (2014). *A novel actuator phasing method for ultrasonic de-icing of aircraft structures*: The Pennsylvania State University.
- Brinkmann, M., & Lipowsky, R. (2002). Wetting morphologies on substrates with striped surface domains. *Journal of applied physics*, 92(8), 4296-4306.
- Bu, X., Lin, G., Yu, J., Yang, S., & Song, X. (2013). Numerical simulation of an airfoil electrothermal anti-icing system. *Proceedings of the Institution of Mechanical Engineers, Part G: Journal of Aerospace Engineering*, 227(10), 1608-1622.
- Cao, Y., Tan, W., & Wu, Z. (2018). Aircraft icing: An ongoing threat to aviation safety. *Aerospace science and technology*, 75, 353-385.
- Cassie, A. B. D., & Baxter, S. (1944). Wettability of porous surfaces. *Transactions of the Faraday society*, 40, 546-551.
- Chavan, S., Park, D., Singla, N., Sokalski, P., Boyina, K., & Miljkovic, N. (2018). Effect of latent heat released by freezing droplets during frost wave propagation. *Langmuir*, 34(22), 6636-6644.

- Chehrghani, M. M., Abbasiasl, T., Sadaghiani, A. K., & Koşar, A. (2021). Biphilic surfaces with optimum hydrophobic islands on a superhydrophobic background for dropwise flow condensation. *Langmuir*, 37(46), 13567-13575.
- Chen, C., Tian, Z., Luo, X., Jiang, G., Hu, X., Wang, L., . . . Zhong, M. (2022). Micro–Nano–Nanowire Triple Structure-Held PDMS Superhydrophobic Surfaces for Robust Ultra-Long-Term Icephobic Performance. *ACS Applied Materials & Interfaces*, 14(20), 23973-23982. doi:10.1021/acsami.2c02992
- Chen, H., Wang, F., Fan, H., Hong, R., & Li, W. (2021). Construction of MOF-based superhydrophobic composite coating with excellent abrasion resistance and durability for self-cleaning, corrosion resistance, anti-icing, and loading-increasing research. *Chemical Engineering Journal*, 408, 127343. doi:<https://doi.org/10.1016/j.cej.2020.127343>
- Chen, H., Zhang, X., Zhang, P., & Zhang, Z. (2012). Facile approach in fabricating superhydrophobic SiO<sub>2</sub>/polymer nanocomposite coating. *Applied Surface Science*, 261, 628-632. doi:<https://doi.org/10.1016/j.apsusc.2012.08.071>
- Chen, S., Li, X., Dong, E., Lv, H., Yang, X., Liu, R., & Liu, B. (2019). Intrinsic and extrinsic responses of ZIF-8 under high pressure: a combined Raman and X-ray diffraction investigation. *The Journal of Physical Chemistry C*, 123(49), 29693-29707.
- Chen, X., Patel, R. S., Weibel, J. A., & Garimella, S. V. (2016). Coalescence-induced jumping of multiple condensate droplets on hierarchical superhydrophobic surfaces. *Scientific Reports*, 6(1), 18649.
- Choi, H., & Liang, H. (2016). Wettability and spontaneous penetration of a water drop into hydrophobic pores. *Journal of Colloid and Interface Science*, 477, 176-180. doi:<https://doi.org/10.1016/j.jcis.2016.05.029>
- Dalili, N., Edrisy, A., & Carriveau, R. (2009). A review of surface engineering issues critical to wind turbine performance. *Renewable and Sustainable energy reviews*, 13(2), 428-438.
- Deng, A. P., & Wu, J. F. (2012). Analysis of Team Purchase Online Profit Model based on the Asymmetric Information Theory. *Statistics and Decision*, 351(3), 67-69.
- Deng, X., Mammen, L., Zhao, Y., Lellig, P., Müllen, K., Li, C., . . . Vollmer, D. (2011). Transparent, thermally stable and mechanically robust superhydrophobic surfaces made from porous silica capsules. *Adv Mater*, 23(26), 2962-2965. doi:10.1002/adma.201100410
- Ding, Y., Ma, G., Chai, Q., & Jiang, Y. (2004). Experiment investigation of reverse cycle defrosting methods on air source heat pump with TXV as the throttle regulator. *International Journal of Refrigeration*, 27(6), 671-678.

- Eberle, P., Tiwari, M. K., Maitra, T., & Poulidakos, D. (2014). Rational nanostructuring of surfaces for extraordinary icephobicity. *Nanoscale*, 6(9), 4874-4881.
- Erbil, H. Y., & Cansoy, C. E. (2009). Range of applicability of the Wenzel and Cassie–Baxter equations for superhydrophobic surfaces. *Langmuir*, 25(24), 14135-14145.
- Fan, Z., & Men, H. (2022). Heterogeneous nucleation and grain initiation on a single substrate. *Metals*, 12(9), 1454.
- Farhadi, S., Farzaneh, M., & Kulinich, S. A. (2011). Anti-icing performance of superhydrophobic surfaces. *Applied Surface Science*, 257(14), 6264-6269. doi:<https://doi.org/10.1016/j.apsusc.2011.02.057>
- Feng, S., Zhang, X., Shi, D., & Wang, Z. (2021). Zeolitic imidazolate framework-8 (ZIF-8) for drug delivery: A critical review. *Frontiers of Chemical Science and Engineering*, 15, 221-237.
- Fürstner, R., Barthlott, W., Neinhuis, C., & Walzel, P. (2005). Wetting and Self-Cleaning Properties of Artificial Superhydrophobic Surfaces. *Langmuir*, 21(3), 956-961. doi:10.1021/la0401011
- Gantasala, S., Luneno, J.-C., & Aidanpaa, J.-O. (2016). Detection of ice mass based on the natural frequencies of wind turbine blade. *Wind Energy Science Discussions*, 1-17.
- Gao, T., Luo, Z. B., Zhou, Y., & Yang, S. K. (2021). A novel de-icing strategy combining electric-heating with plasma synthetic jet actuator. *Proceedings of the Institution of Mechanical Engineers, Part G: Journal of Aerospace Engineering*, 235(4), 513-522.
- Gao, Y., Sun, Y., & Guo, D. (2014). Facile fabrication of superhydrophobic surfaces with low roughness on Ti–6Al–4V substrates via anodization. *Applied Surface Science*, 314, 754-759. doi:<https://doi.org/10.1016/j.apsusc.2014.07.059>
- Gharib, G., Saeidiharzand, S., Sadaghiani, A. K., & Koşar, A. (2021). Antifreeze Proteins: A Tale of Evolution From Origin to Energy Applications. *Front Bioeng Biotechnol*, 9, 770588. doi:10.3389/fbioe.2021.770588
- Ghosh, A., Ganguly, R., Schutzius, T. M., & Megaridis, C. M. (2014). Wettability patterning for high-rate, pumpless fluid transport on open, non-planar microfluidic platforms. *Lab on a Chip*, 14(9), 1538-1550.
- Graeber, G., Dolder, V., Schutzius, T. M., & Poulidakos, D. (2018). Cascade freezing of supercooled water droplet collectives. *ACS nano*, 12(11), 11274-11281.
- Gultekin, A., Erkan, N., Ozdemir, E., Colak, U., & Suzuki, S. (2021). Simultaneous multiple droplet impact and their interactions on a heated surface. *Experimental Thermal and Fluid Science*, 120, 110255. doi:<https://doi.org/10.1016/j.expthermflusci.2020.110255>
- Gurumukhi, Y., Chavan, S., Sett, S., Boyina, K., Ramesh, S., Sokalski, P., . . . Chen, J.-Y. (2020). Dynamic defrosting on superhydrophobic and biphilic surfaces. *Matter*, 3(4), 1178-1195.

- Hansman Jr, R. J. (1982). Microwave ice prevention system. In: Google Patents.
- He, Z., Yang, X., Mu, L., Wang, N., & Lan, X. (2022). A versatile “3M” methodology to obtain superhydrophobic PDMS-based materials for antifouling applications. *Frontiers in Bioengineering and Biotechnology*, *10*, 998852.
- Heydarian, S., Jafari, R., & Momen, G. (2021). Recent progress in the anti-icing performance of slippery liquid-infused surfaces. *Progress in Organic Coatings*, *151*, 106096. doi:<https://doi.org/10.1016/j.porgcoat.2020.106096>
- Hooda, A., Goyat, M. S., Pandey, J. K., Kumar, A., & Gupta, R. (2020). A review on fundamentals, constraints and fabrication techniques of superhydrophobic coatings. *Progress in Organic Coatings*, *142*, 105557. doi:<https://doi.org/10.1016/j.porgcoat.2020.105557>
- Hou, Y., Yu, M., Shang, Y., Zhou, P., Song, R., Xu, X., . . . Yao, S. (2018). Suppressing ice nucleation of supercooled condensate with biphilic topography. *Physical review letters*, *120*(7), 075902.
- Huang, C., & Guo, Z. (2019). Fabrications and applications of slippery liquid-infused porous surfaces inspired from nature: A review. *Journal of Bionic Engineering*, *16*, 769-793.
- Huang, C., Zhao, Y., & Gu, T. (2022). Ice Dendrite Growth Atop a Frozen Drop under Natural Convection Conditions. *Crystals*, *12*(3), 323.
- Huang, W., Huang, J., Guo, Z., & Liu, W. (2022). Icephobic/anti-icing properties of superhydrophobic surfaces. *Advances in Colloid and Interface Science*, 102658.
- Hung, C.-C., Dillehay, M. E., & Stahl, M. (1987). A heater made from graphite composite material for potential deicing application. *Journal of Aircraft*, *24*(10), 725-730.
- Ilinca, A. (2011). Analysis and mitigation of icing effects on wind turbines. *Wind turbines*, *4*(4), 183-214.
- Janjua, Z. A., Turnbull, B., Choy, K.-L., Pandis, C., Liu, J., Hou, X., & Choi, K.-S. (2017). Performance and durability tests of smart icephobic coatings to reduce ice adhesion. *Applied Surface Science*, *407*, 555-564. doi:<https://doi.org/10.1016/j.apsusc.2017.02.206>
- Jiang, G., Chen, L., Zhang, S., & Huang, H. (2018). Superhydrophobic SiC/CNTs Coatings with Photothermal Deicing and Passive Anti-Icing Properties. *ACS Applied Materials & Interfaces*, *10*(42), 36505-36511. doi:10.1021/acsami.8b11201
- Jiang, G., Hu, J., & Chen, L. (2020). Preparation of a Flexible Superhydrophobic Surface and Its Wetting Mechanism Based on Fractal Theory. *Langmuir*, *36*(29), 8435-8443. doi:10.1021/acs.langmuir.0c00823
- Jin, P., Yan, X., Hoque, M. J., Rabbi, K. F., Sett, S., Ma, J., . . . Miljkovic, N. (2022). Ultra-low ice-substrate adhesion and self-deicing during droplet impact freezing. *Cell Reports Physical Science*, *3*(5), 100894. doi:<https://doi.org/10.1016/j.xcrp.2022.100894>

- Jin, Y., He, Z., Guo, Q., & Wang, J. (2017). Control of ice propagation by using polyelectrolyte multilayer coatings. *Angewandte Chemie International Edition*, 56(38), 11436-11439.
- Kamegawa, T., Shimizu, Y., & Yamashita, H. (2012). Superhydrophobic surfaces with photocatalytic self-cleaning properties by nanocomposite coating of TiO<sub>2</sub> and polytetrafluoroethylene. *Advanced Materials*, 24(27), 3697-3700.
- Khadka, A., Subeshan, B., & Asmatulu, R. (2021). Correction to: Studies on de-icing and anti-icing of carbon fiber-reinforced composites for aircraft surfaces using commercial multifunctional permanent superhydrophobic coatings. *Journal of Materials Science*, 56(5), 4051-4051.
- Kida, K., Okita, M., Fujita, K., Tanaka, S., & Miyake, Y. (2013). Formation of high crystalline ZIF-8 in an aqueous solution. *CrystEngComm*, 15(9), 1794-1801.
- Kim, A., Lee, C., Kim, H., & Kim, J. (2015). Simple Approach to Superhydrophobic Nanostructured Al for Practical Antifrosting Application Based on Enhanced Self-propelled Jumping Droplets. *ACS Applied Materials & Interfaces*, 7(13), 7206-7213. doi:10.1021/acsami.5b00292
- Kobina Sam, E., Kobina Sam, D., Lv, X., Liu, B., Xiao, X., Gong, S., . . . Liu, J. (2019). Recent development in the fabrication of self-healing superhydrophobic surfaces. *Chemical Engineering Journal*, 373, 531-546. doi:<https://doi.org/10.1016/j.cej.2019.05.077>
- Kreder, M. J., Alvarenga, J., Kim, P., & Aizenberg, J. (2016). Design of anti-icing surfaces: smooth, textured or slippery? *Nature Reviews Materials*, 1(1), 15003. doi:10.1038/natrevmats.2015.3
- Kwak, G., Seol, M., Tak, Y., & Yong, K. (2009). Superhydrophobic ZnO Nanowire Surface: Chemical Modification and Effects of UV Irradiation. *The Journal of Physical Chemistry C*, 113(28), 12085-12089. doi:10.1021/jp900072s
- Lamb, D., & Verlinde, J. (2011). *Physics and chemistry of clouds*: Cambridge University Press.
- Landry, M., Beauchemin, R., & Venne, A. (2000). *De-icing EHV overhead transmission lines using electromagnetic forces generated by moderate short-circuit currents*. Paper presented at the 2000 IEEE ESMO-2000 IEEE 9th International Conference on Transmission and Distribution Construction, Operation and Live-Line Maintenance Proceedings. ESMO 2000 Proceedings. Global ESMO 2000. The Pow.
- Latthe, S. S., & Rao, A. V. (2012). Superhydrophobic SiO<sub>2</sub> micro-particle coatings by spray method. *Surface and Coatings Technology*, 207, 489-492. doi:<https://doi.org/10.1016/j.surfcoat.2012.07.055>
- Lee, J.-P., Choi, S., & Park, S. (2011). Extremely Superhydrophobic Surfaces with Micro- and Nanostructures Fabricated by Copper Catalytic Etching. *Langmuir*, 27(2), 809-814. doi:10.1021/la1045354

- Lee, Y.-R., Jang, M.-S., Cho, H.-Y., Kwon, H.-J., Kim, S., & Ahn, W.-S. (2015). ZIF-8: A comparison of synthesis methods. *Chemical Engineering Journal*, 271, 276-280. doi:<https://doi.org/10.1016/j.cej.2015.02.094>
- Li, B., He, L., Liu, Y., Luo, J., & Zhang, G. (2019). Influences of key factors in hot-air deicing for live substation equipment. *Cold regions science and technology*, 160, 89-96.
- Li, J., Wan, H., Ye, Y., Zhou, H., & Chen, J. (2012). One-step process for the fabrication of superhydrophobic surfaces with easy repairability. *Applied Surface Science*, 258(7), 3115-3118. doi:<https://doi.org/10.1016/j.apsusc.2011.11.047>
- Li, Q., & Guo, Z. (2018). Fundamentals of icing and common strategies for designing biomimetic anti-icing surfaces. *Journal of Materials Chemistry A*, 6(28), 13549-13581. doi:10.1039/C8TA03259A
- Li, W., Zhan, Y., & Yu, S. (2021). Applications of superhydrophobic coatings in anti-icing: Theory, mechanisms, impact factors, challenges and perspectives. *Progress in Organic Coatings*, 152, 106117. doi:<https://doi.org/10.1016/j.porgcoat.2020.106117>
- Li, Y., Li, B., Zhao, X., Tian, N., & Zhang, J. (2018). Totally Waterborne, Nonfluorinated, Mechanically Robust, and Self-Healing Superhydrophobic Coatings for Actual Anti-Icing. *ACS Applied Materials & Interfaces*, 10(45), 39391-39399. doi:10.1021/acsami.8b15061
- Libbrecht, K. G. (2017). Physical dynamics of ice crystal growth. *Annual Review of Materials Research*, 47, 271-295.
- Liu, J., Zhu, C., Liu, K., Jiang, Y., Song, Y., Francisco, J. S., . . . Wang, J. (2017). Distinct ice patterns on solid surfaces with various wettabilities. *Proceedings of the National Academy of Sciences*, 114(43), 11285-11290.
- Long, Y., Yin, X., Mu, P., Wang, Q., Hu, J., & Li, J. (2020). Slippery liquid-infused porous surface (SLIPS) with superior liquid repellency, anti-corrosion, anti-icing and intensified durability for protecting substrates. *Chemical Engineering Journal*, 401, 126137. doi:<https://doi.org/10.1016/j.cej.2020.126137>
- Lu, Y., Sathasivam, S., Song, J., Crick, C. R., Carmalt, C. J., & Parkin, I. P. (2015). Robust self-cleaning surfaces that function when exposed to either air or oil. *Science*, 347(6226), 1132-1135. doi:10.1126/science.aaa0946
- Lu, Y., Song, J., Liu, X., Xu, W., Sun, J., & Xing, Y. (2012). Loading capacity of a self-assembled superhydrophobic boat array fabricated via electrochemical method. *Micro & Nano Letters*, 7(8), 786-789. Retrieved from <https://digital-library.theiet.org/content/journals/10.1049/mnl.2012.0435>

- Lv, J., Song, Y., Jiang, L., & Wang, J. (2014). Bio-inspired strategies for anti-icing. *ACS nano*, 8(4), 3152-3169.
- Maa, J. R. (1978). Drop size distribution and heat flux of dropwise condensation. *The Chemical Engineering Journal*, 16(3), 171-176.
- Madi, E., Pope, K., Huang, W., & Iqbal, T. (2019). A review of integrating ice detection and mitigation for wind turbine blades. *Renewable and Sustainable energy reviews*, 103, 269-281.
- Mayer, C., Ilinca, A., Fortin, G., & Perron, J. (2007). Wind tunnel study of electro-thermal de-icing of wind turbine blades. *International Journal of Offshore and Polar Engineering*, 17(03).
- Moser, M. J., George, B., Zangl, H., & Brasseur, G. (2009, 5-7 May 2009). *Icing detector for overhead power transmission lines*. Paper presented at the 2009 IEEE Instrumentation and Measurement Technology Conference.
- Motezakker, A. R., Sadaghiani, A. K., Celik, S., Larsen, T., Villanueva, L. G., & Koşar, A. (2019). Optimum ratio of hydrophobic to hydrophilic areas of biphilic surfaces in thermal fluid systems involving boiling. *International Journal of Heat and Mass Transfer*, 135, 164-174.
- Muthumani, A., Fay, L., Akin, M., Wang, S., Gong, J., & Shi, X. (2014). Correlating lab and field tests for evaluation of deicing and anti-icing chemicals: A review of potential approaches. *Cold Regions Science and Technology*, 97, 21-32.
- Nath, S., Ahmadi, S. F., & Boreyko, J. B. (2017). A review of condensation frosting. *Nanoscale and Microscale Thermophysical Engineering*, 21(2), 81-101.
- Nine, M. J., Tung, T. T., Alotaibi, F., Tran, D. N. H., & Losic, D. (2017). Facile Adhesion-Tuning of Superhydrophobic Surfaces between “Lotus” and “Petal” Effect and Their Influence on Icing and Deicing Properties. *ACS Applied Materials & Interfaces*, 9(9), 8393-8402. doi:10.1021/acsami.6b16444
- Nordin, N., Ismail, A., Mustafa, A., Goh, P., Rana, D., & Matsuura, T. (2014). Aqueous room temperature synthesis of zeolitic imidazole framework 8 (ZIF-8) with various concentrations of triethylamine. *RSC advances*, 4(63), 33292-33300.
- Nordin, N. A. H. M., Ismail, A. F., Misdan, N., & Nazri, N. A. M. (2017). *Modified ZIF-8 mixed matrix membrane for CO<sub>2</sub>/CH<sub>4</sub> separation*. Paper presented at the AIP Conference Proceedings.
- Onda, T., Shibuichi, S., Satoh, N., & Tsujii, K. (1996). Super-Water-Repellent Fractal Surfaces. *Langmuir*, 12(9), 2125-2127. doi:10.1021/la950418o

- Pan, R., Zhang, H., & Zhong, M. (2021). Triple-Scale Superhydrophobic Surface with Excellent Anti-Icing and Icephobic Performance via Ultrafast Laser Hybrid Fabrication. *ACS Applied Materials & Interfaces*, 13(1), 1743-1753. doi:10.1021/acsami.0c16259
- Pan, Y., Liu, Y., Zeng, G., Zhao, L., & Lai, Z. (2011). Rapid synthesis of zeolitic imidazolate framework-8 (ZIF-8) nanocrystals in an aqueous system. *Chemical Communications*, 47(7), 2071-2073.
- Parent, O., & Ilinca, A. (2011). Anti-icing and de-icing techniques for wind turbines: Critical review. *Cold regions science and technology*, 65(1), 88-96.
- Parvate, S., Dixit, P., & Chattopadhyay, S. (2020). Superhydrophobic Surfaces: Insights from Theory and Experiment. *The Journal of Physical Chemistry B*, 124(8), 1323-1360. doi:10.1021/acs.jpcc.9b08567
- Pérez-Lombard, L., Ortiz, J., Coronel, J. F., & Maestre, I. R. (2011). A review of HVAC systems requirements in building energy regulations. *Energy and buildings*, 43(2-3), 255-268.
- Pourbagian, M., & Habashi, W. (2013). *CFD-based optimization of electro-thermal wing ice protection systems in de-icing mode*. Paper presented at the 51st Aiaa Aerospace Sciences Meeting Including the New Horizons Forum and Aerospace Exposition.
- Qian, B., & Shen, Z. (2005). Fabrication of Superhydrophobic Surfaces by Dislocation-Selective Chemical Etching on Aluminum, Copper, and Zinc Substrates. *Langmuir*, 21(20), 9007-9009. doi:10.1021/la051308c
- Qing, Y., Yang, C., Yu, N., Shang, Y., Sun, Y., Wang, L., & Liu, C. (2016). Superhydrophobic TiO<sub>2</sub>/polyvinylidene fluoride composite surface with reversible wettability switching and corrosion resistance. *Chemical Engineering Journal*, 290, 37-44. doi:<https://doi.org/10.1016/j.cej.2016.01.013>
- Radermacher, R., & Kim, K. (1996). Domestic refrigerators: recent developments. *International Journal of Refrigeration*, 19(1), 61-69. doi:[https://doi.org/10.1016/0140-7007\(95\)00069-0](https://doi.org/10.1016/0140-7007(95)00069-0)
- Rashid, T., Khawaja, H. A., & Edvardsen, K. (2016). Review of marine icing and anti-/de-icing systems. *Journal of marine engineering & technology*, 15(2), 79-87.
- Roach, P., Shirtcliffe, N. J., & Newton, M. I. (2008). Progress in superhydrophobic surface development. *Soft Matter*, 4(2), 224-240. doi:10.1039/B712575P
- Ryerson, C. C., & Koenig, G. G. (2003). *Helicopter preflight deicing* (0148-7191). Retrieved from Saharudin, K. A., Sreekantan, S., Basiron, N., Chun, L. K., Kumaravel, V., Abdullah, T. K., & Ahmad, Z. A. (2018). Improved super-hydrophobicity of eco-friendly coating from palm oil fuel ash (POFA) waste. *Surface and Coatings Technology*, 337, 126-135. doi:<https://doi.org/10.1016/j.surfcoat.2017.11.070>

- Sann, E. E., Pan, Y., Gao, Z., Zhan, S., & Xia, F. (2018). Highly hydrophobic ZIF-8 particles and application for oil-water separation. *Separation and Purification Technology*, 206, 186-191. doi:<https://doi.org/10.1016/j.seppur.2018.04.027>
- Schaefer, V. J., & Langmuir, I. (1953). *Project cirrus*.
- Schremb, M., Roisman, I. V., & Tropea, C. (2018). Normal impact of supercooled water drops onto a smooth ice surface: experiments and modelling. *Journal of Fluid Mechanics*, 835, 1087-1107. doi:10.1017/jfm.2017.797
- Schutzius, T. M., Jung, S., Maitra, T., Eberle, P., Antonini, C., Stamatopoulos, C., & Poulikakos, D. (2015). Physics of icing and rational design of surfaces with extraordinary icephobicity. *Langmuir*, 31(17), 4807-4821.
- Sharifi, N., Pugh, M., Moreau, C., & Dolatabadi, A. (2016). Developing hydrophobic and superhydrophobic TiO<sub>2</sub> coatings by plasma spraying. *Surface and Coatings Technology*, 289, 29-36. doi:<https://doi.org/10.1016/j.surfcoat.2016.01.029>
- Sharp, D. H. (1984). An overview of Rayleigh-Taylor instability. *Physica D: Nonlinear Phenomena*, 12(1-3), 3-18.
- Shen, X., Wang, H., Lin, G., Bu, X., & Wen, D. (2020). Unsteady simulation of aircraft electro-thermal deicing process with temperature-based method. *Proceedings of the Institution of Mechanical Engineers, Part G: Journal of Aerospace Engineering*, 234(2), 388-400.
- Shirtcliffe, N. J., McHale, G., Newton, M. I., & Zhang, Y. (2009). Superhydrophobic Copper Tubes with Possible Flow Enhancement and Drag Reduction. *ACS Applied Materials & Interfaces*, 1(6), 1316-1323. doi:10.1021/am9001937
- Sing, K. S. (1985). Reporting physisorption data for gas/solid systems with special reference to the determination of surface area and porosity (Recommendations 1984). *Pure and applied chemistry*, 57(4), 603-619.
- Song, D., Jiang, Y., Chou, T., Asawa, K., & Choi, C.-H. (2020). Spontaneous Deicing on Cold Surfaces. *Langmuir*, 36(38), 11245-11254. doi:10.1021/acs.langmuir.0c01523
- Song, J., Xu, W., & Lu, Y. (2012). One-step electrochemical machining of superhydrophobic surfaces on aluminum substrates. *Journal of Materials Science*, 47(1), 162-168. doi:10.1007/s10853-011-5783-2
- Song, Y.-Y., Schmidt-Stein, F., Bauer, S., & Schmuki, P. (2009). Amphiphilic TiO<sub>2</sub> Nanotube Arrays: An Actively Controllable Drug Delivery System. *Journal of the American Chemical Society*, 131(12), 4230-4232. doi:10.1021/ja810130h
- Sørensen, J. N. (2011). Aerodynamic aspects of wind energy conversion. *Annual Review of Fluid Mechanics*, 43, 427-448.

- Sreekantan, S., Yong, A. X., Basiron, N., Ahmad, F., & De'nan, F. (2022). Effect of Solvent on Superhydrophobicity Behavior of Tiles Coated with Epoxy/PDMS/SS. *Polymers (Basel)*, *14*(12). doi:10.3390/polym14122406
- STOECKER, W. F., Lux Jr, J., & Kooy, R. (1983). Energy considerations in hot-gas defrosting of industrial refrigeration coils. *ASHRAE transactions*, *89*, 549-573.
- Tenjimbayashi, M., Park, J.-Y., Muto, J., Kobayashi, Y., Yoshikawa, R., Monnai, Y., & Shiratori, S. (2018). In situ formation of slippery-liquid-infused nanofibrous surface for a transparent antifouling endoscope lens. *ACS Biomaterials Science & Engineering*, *4*(5), 1871-1879.
- Tong, W., Xiong, D., Wang, N., Wu, Z., & Zhou, H. (2019). Mechanically robust superhydrophobic coating for aeronautical composite against ice accretion and ice adhesion. *Composites Part B: Engineering*, *176*, 107267. doi:<https://doi.org/10.1016/j.compositesb.2019.107267>
- Tourkine, P., Le Merrer, M., & Quéré, D. (2009). Delayed Freezing on Water Repellent Materials. *Langmuir*, *25*(13), 7214-7216. doi:10.1021/la900929u
- Varanasi, K. K., Hsu, M., Bhate, N., Yang, W., & Deng, T. (2009). Spatial control in the heterogeneous nucleation of water. *Applied Physics Letters*, *95*(9), 094101.
- Vocale, P., Morini, G. L., & Spiga, M. (2014). Influence of outdoor air conditions on the air source heat pumps performance. *Energy Procedia*, *45*, 653-662.
- Wang, C., & Guo, Z. (2020). A comparison between superhydrophobic surfaces (SHS) and slippery liquid-infused porous surfaces (SLIPS) in application. *Nanoscale*, *12*(44), 22398-22424.
- Wang, F., Ding, W., He, J., & Zhang, Z. (2019). Phase transition enabled durable anti-icing surfaces and its DIY design. *Chemical Engineering Journal*, *360*, 243-249.
- Wang, H., He, M., Liu, H., & Guan, Y. (2019). One-Step Fabrication of Robust Superhydrophobic Steel Surfaces with Mechanical Durability, Thermal Stability, and Anti-icing Function. *ACS Applied Materials & Interfaces*, *11*(28), 25586-25594. doi:10.1021/acsami.9b06865
- Wang, H., Zhang, F., Wang, J., Wang, Z., Xu, H., & Zhang, W. (2023a). Efficient defrosting on hybrid surfaces with heterogeneous wettability. *Case Studies in Thermal Engineering*, *102999*.
- Wang, H., Zhang, F., Wang, J., Wang, Z., Xu, H., & Zhang, W. (2023b). Efficient defrosting on hybrid surfaces with heterogeneous wettability. *Case Studies in Thermal Engineering*, *45*, 102999.
- Wang, N., Xiong, D., Deng, Y., Shi, Y., & Wang, K. (2015). Mechanically Robust Superhydrophobic Steel Surface with Anti-Icing, UV-Durability, and Corrosion Resistance Properties. *ACS Applied Materials & Interfaces*, *7*(11), 6260-6272. doi:10.1021/acsami.5b00558

- Wang, Y., Xu, Y., & Huang, Q. (2017). Progress on ultrasonic guided waves de-icing techniques in improving aviation energy efficiency. *Renewable and Sustainable energy reviews*, 79, 638-645.
- Wang, Y., Xue, J., Wang, Q., Chen, Q., & Ding, J. (2013). Verification of Icephobic/Anti-icing Properties of a Superhydrophobic Surface. *ACS Applied Materials & Interfaces*, 5(8), 3370-3381. doi:10.1021/am400429q
- Wang, Z. (2017). Recent progress on ultrasonic de-icing technique used for wind power generation, high-voltage transmission line and aircraft. *Energy and buildings*, 140, 42-49.
- Watson, G. S., Green, D. W., Cribb, B. W., Brown, C. L., Meritt, C. R., Tobin, M. J., . . . Watson, J. A. (2017). Insect Analogue to the Lotus Leaf: A Planthopper Wing Membrane Incorporating a Low-Adhesion, Nonwetting, Superhydrophobic, Bactericidal, and Biocompatible Surface. *ACS Applied Materials & Interfaces*, 9(28), 24381-24392. doi:10.1021/acsami.7b08368
- Wei, K., Yang, Y., Zuo, H., & Zhong, D. (2020). A review on ice detection technology and ice elimination technology for wind turbine. *Wind Energy*, 23(3), 433-457.
- Wen, R., & Ma, X. (2020a). Advances in Dropwise Condensation: Dancing Droplets. In
- Wen, R., & Ma, X. (2020b). Advances in dropwise condensation: Dancing droplets. In *21st century surface science-a handbook* (pp. 1-26): IntechOpen.
- Wenzel, R. N. (1936). RESISTANCE OF SOLID SURFACES TO WETTING BY WATER. *Industrial & Engineering Chemistry*, 28(8), 988-994. doi:10.1021/ie50320a024
- Wu, C., Liu, Q., Chen, R., Liu, J., Zhang, H., Li, R., . . . Wang, J. (2017). Fabrication of ZIF-8@SiO<sub>2</sub> Micro/Nano Hierarchical Superhydrophobic Surface on AZ31 Magnesium Alloy with Impressive Corrosion Resistance and Abrasion Resistance. *ACS Applied Materials & Interfaces*, 9(12), 11106-11115. doi:10.1021/acsami.6b16848
- Wu, T., Xu, W.-h., Guo, K., Xie, H., & Qu, J.-p. (2021). Efficient fabrication of lightweight polyethylene foam with robust and durable superhydrophobicity for self-cleaning and anti-icing applications. *Chemical Engineering Journal*, 407, 127100. doi:<https://doi.org/10.1016/j.cej.2020.127100>
- Wyderski, M., Lozada-Ruiz, A., Ryerson, C., Davila, J., & Tarazano, D. (2003). *Evaluation of environmentally friendly, glycol-free mobile aircraft deicing system* (0148-7191). Retrieved from
- Xia, Y., Hrnjak, P. S., & Jacobi, A. M. (2005). Air-Side Thermal-Hydraulic Performance of Louvered-Fin, Flat-Tube Heat Exchangers with Sequential Frost-Growth Cycles. *ASHRAE transactions*, 111(1).

- Xu, Q. F., & Wang, J. N. (2009). A superhydrophobic coating on aluminium foil with an anti-corrosive property. *New Journal of Chemistry*, 33(4), 734-738.
- Xue, C.-H., Guo, X.-J., Ma, J.-Z., & Jia, S.-T. (2015). Fabrication of robust and antifouling superhydrophobic surfaces via surface-initiated atom transfer radical polymerization. *ACS Applied Materials & Interfaces*, 7(15), 8251-8259.
- Yan, Y.-l., Cai, Y.-x., Liu, X.-c., Ma, G.-w., Lv, W., & Wang, M.-x. (2020). Hydrophobic Modification on the Surface of SiO<sub>2</sub> Nanoparticle: Wettability Control. *Langmuir*, 36(49), 14924-14932. doi:10.1021/acs.langmuir.0c02118
- Yang, S., Wu, C., Zhao, G., Sun, J., Yao, X., Ma, X., & Wang, Z. (2021). Condensation frosting and passive anti-frosting. *Cell Reports Physical Science*, 2(7), 100474.
- Yao, X., Wu, S., Chen, L., Ju, J., Gu, Z., Liu, M., . . . Jiang, L. (2015). Self-Replenishable Anti-Waxing Organogel Materials. *Angewandte Chemie International Edition*, 54(31), 8975-8979.
- Yeom, C., & Kim, Y. (2016). Purification of oily seawater/wastewater using superhydrophobic nano-silica coated mesh and sponge. *Journal of Industrial and Engineering Chemistry*, 40, 47-53. doi:<https://doi.org/10.1016/j.jiec.2016.06.005>
- Yin, Y., Liu, T., Chen, S., Liu, T., & Cheng, S. (2008). Structure stability and corrosion inhibition of super-hydrophobic film on aluminum in seawater. *Applied Surface Science*, 255(5), 2978-2984.
- Yousuf, A., Khawaja, H. A., & Virk, M. S. Conceptual Design of Cost-Effective Ice Detection System Based on Infrared Thermography. *Available at SSRN 4411767*.
- Yu, J., Zhang, H., & You, S. (2012). Heat transfer analysis and experimental verification of casted heat exchanger in non-icing and icing conditions in winter. *Renewable Energy*, 41, 39-43. doi:<https://doi.org/10.1016/j.renene.2011.10.003>
- Yu, X., Zhang, Y., Hu, R., & Luo, X. (2021). Water droplet bouncing dynamics. *Nano Energy*, 81, 105647.
- Yuan, Y., Xu, X., Xia, J., Zhang, F., Wang, Z., & Liu, Q. (2019). A hybrid material composed of reduced graphene oxide and porous carbon prepared by carbonization of a zeolitic imidazolate framework (type ZIF-8) for voltammetric determination of chloramphenicol. *Microchimica Acta*, 186, 1-8.
- Zeng, Q., & Xu, S. (2015). Thermodynamics and Characteristics of Heterogeneous Nucleation on Fractal Surfaces. *The Journal of Physical Chemistry C*, 119(49), 27426-27433. doi:10.1021/acs.jpcc.5b07709

- Zhang, J., Wang, A., & Seeger, S. (2014). Nepenthes pitcher inspired anti-wetting silicone nanofilaments coatings: preparation, unique anti-wetting and self-cleaning behaviors. *Advanced Functional Materials*, 24(8), 1074-1080.
- Zhang, X., Geng, T., Guo, Y., Zhang, Z., & Zhang, P. (2013). Facile fabrication of stable superhydrophobic SiO<sub>2</sub>/polystyrene coating and separation of liquids with different surface tension. *Chemical Engineering Journal*, 231, 414-419. doi:<https://doi.org/10.1016/j.cej.2013.07.046>
- Zhang, Z., Ge, B., Men, X., & Li, Y. (2016). Mechanically durable, superhydrophobic coatings prepared by dual-layer method for anti-corrosion and self-cleaning. *Colloids and Surfaces A: Physicochemical and Engineering Aspects*, 490, 182-188. doi:<https://doi.org/10.1016/j.colsurfa.2015.11.049>
- Zhang, Z., & Liu, X.-Y. (2018). Control of ice nucleation: freezing and antifreeze strategies. *Chemical Society Reviews*, 47(18), 7116-7139. doi:10.1039/C8CS00626A
- Zhang, Z., Lusi, A., Hu, H., Bai, X., & Hu, H. (2021). An experimental study on the detrimental effects of deicing fluids on the performance of icephobic coatings for aircraft icing mitigation. *Aerospace science and technology*, 119, 107090.
- Zhao, L., Liu, Q., Gao, R., Wang, J., Yang, W., & Liu, L. (2014). One-step method for the fabrication of superhydrophobic surface on magnesium alloy and its corrosion protection, antifouling performance. *Corrosion Science*, 80, 177-183. doi:<https://doi.org/10.1016/j.corsci.2013.11.026>
- Zhao, X., & Rose, J. L. (2016). Ultrasonic guided wave tomography for ice detection. *Ultrasonics*, 67, 212-219.
- Zhao, Y., Guo, Q., Lin, T., & Cheng, P. (2020). A review of recent literature on icing phenomena: Transport mechanisms, their modulations and controls. *International Journal of Heat and Mass Transfer*, 159, 120074. doi:<https://doi.org/10.1016/j.ijheatmasstransfer.2020.120074>
- Zhao, Y., Yan, C., Hou, T., Dou, H., & Shen, H. (2022). Multifunctional Ti<sub>3</sub>C<sub>2</sub>T<sub>x</sub> MXene-Based Composite Coatings with Superhydrophobic Anti-icing and Photothermal Deicing Properties. *ACS Applied Materials & Interfaces*, 14(22), 26077-26087. doi:10.1021/acsami.2c07087
- Zheng, S., Bellido-Aguilar, D. A., Huang, Y., Zeng, X., Zhang, Q., & Chen, Z. (2019). Mechanically robust hydrophobic bio-based epoxy coatings for anti-corrosion application. *Surface and Coatings Technology*, 363, 43-50. doi:<https://doi.org/10.1016/j.surfcoat.2019.02.020>
- Zheng, S., Bellido-Aguilar, D. A., Wu, X., Zhan, X., Huang, Y., Zeng, X., . . . Chen, Z. (2019). Durable Waterborne Hydrophobic Bio-Epoxy Coating with Improved Anti-Icing and Self-

Cleaning Performance. *ACS Sustainable Chemistry & Engineering*, 7(1), 641-649.  
doi:10.1021/acssuschemeng.8b04203

Zhuo, Y., Wang, F., Xiao, S., He, J., & Zhang, Z. (2018). One-step fabrication of bioinspired lubricant-regenerable icephobic slippery liquid-infused porous surfaces. *ACS omega*, 3(8), 10139-10144.